Characterization and Optimization of NV-Ensemble in Bulk Diamond for Sensing Application

Dissertation zur Erlangung des Doktorgrades der
Technischen Fakultät der
Albert-Ludwigs-Universität Freiburg im Breisgau

Tingpeng LUO

August. 2022

Institut für Nachhaltige Technische Systeme - INATECH

Fraunhofer-Institut für Angewandte Festkörperphysik IAF

Dekan:

Prof. Dr. Roland Zengerle

Erstgutachter und Betreuer der Arbeit:

Prof. Dr. Dr. Oliver Ambacher
Gips-Schüle Professur für Leistungselektronik
Institut für Nachhaltige Technische Systeme - INATEC

Zweitgutachter:

Prof. Dr. Michael Fiederle
Materialcharakterisierung und Detektortechnologie
Freiburger Materialforschungszentrum - FMF

Disputation

06-February-2023

I declare that the work is that of the me alone except where due acknowledgement has been made. The work has not been submitted previously, in whole or in part, to qualify for any other academic award. The content of the thesis is the result of work which has been carried out since the official commencement date of the approved research program. Any editorial work, paid or unpaid, carried out by a third party is acknowledged. Ethics procedures and guidelines have been followed.

Freiburg, 06-February-2023

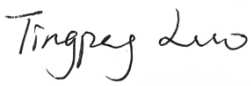

(**Tingpeng Luo**)

Acknowledgements

I would like to express my deep appreciation to Professor Oliver Ambacher for his guidance and support throughout my PhD study. This appreciation extends to Professor Michael Fiederle for being the second reviewer of this thesis.

I am also deeply indebted to Dr. Jan Jeske for his supervision on daily basis, and for leading me into the world of NV centers.

Thanks should also go to Dr. Xavier Vidal, who always supports me with valuable ideas and advice in my research. Many thanks to Lukas Lindner, who supports in every way, the hardware, software, scientific ideas (and even the local culture). I am also very grateful to Julia Langer and Dr. Volker Cimalla, who have grown the large number of diamond samples, which lays the foundation of this thesis.

I would like to extend my sincere thanks to all colleagues and collaborators who have helped with their expertise, scientific thoughts and technical support during these years. Many thanks to:

- our group members Felix Hahl and Niklas Mathes, for extensive scientific exchanges on daily basis.
- the many colleagues Dr. Christoph Schreyvogel, Dr. Christian Giese, Dr. Peter Knittel, Arne Götze, Dr. Jan Engels, Philipp Reinke, Dr. Michael Kunzer, Ralf Schmidt, Thomas Eckermann, Dr. Nicola Lang and Dr. Lutz Kirste for valuable discussions and experimental supports at times.
- the diamond processing team members Michael Ardner, Carmen Schomas, Michaela Fritz, Christine Lell, David Herrling, Sascha Klingelmeier and Tanja Kummerer for all the sample preparation including laser cutting, polishing, cleaning, and basic pre-characterizations.
- Shangjing Liu for the technical support of PL and birefringence measurements.
- Dorothee Luick, Dr. Marko Härtelt and Klaus Schwarz for the technical support of UV-Vis and FTIR measurements.

- Dr. Ralf Ostendorf, Dr. Marcel Rattunde and Dr. Daniel Hähnel for scientific and administrative support.
- Mareike Bausch, Lisa Hees, Birgit Berker, Sabine Rau, Sandra Spang and Beatrice Scherer for administrative supports.
- Professor Takeshi Ohshima, Dr. Shinobu Onoda and Dr. Shuya Ishii from QST, Japan, for the support of e-beam irradiation, annealing and EPR measurements.
- Dr. Marco Capelli, Professor Brant Gibson and Professor Andrew Greentree from RMIT University, Australia, for valuable scientific exchanges.
- Dr. Brett C. Johnson and his team members from RMIT University, Australia, for the EPR support.
- Di Wang and Dr. David A. Simpson from University of Melbourne, Australia, for the Hahn-echo measurements.
- Dr. Rémi Blinder and Professor Fedor Jelezko from Universität Ulm, Germany, for the EPR support.
- Professor Alexandre Zaitsev for the support of LPHT annealing.
- Dr. Serhiy Danylyuk, Dr. Klaus Bergmann and their team members for the EUV support.

All their help makes this complex characterization work possible.

Furthermore, I would like to thank all my family members, in particular my dad who is always proud of me and encourages my decisions in life, and my mom who lives in and supports me from my heart. I also thank the many of my friends (and their cats) who care about me so much and always try to help even though we are far apart.

Finally my special thanks to my partner Qianli, who influences me through his positive attitude, his self-discipline, and his kind nature. Only with the help, encouragement and love from him I can finish my PhD study. Thanks for always being by my side, and thanks for making me a better person.

It was a nice journey with diamonds, an interesting chapter in my life. I hope this thesis draws a satisfactory comma for the story, and I have started looking forward to its next chapter.

Contents

List of Figures

List of Tables

Abbreviations

AC	**A**lternating **C**urrent
CVD	**C**hemical **V**apor **D**eposition
CW	**C**ontinuous-**W**ave
DC	**D**irect **C**urrent
EPR	**E**lectron **P**aramagnetic **R**esonance
FTIR	**F**ourier-**T**ransform **I**nfra**R**ed (spectroscopy)
FWHM	**F**ull **W**idth at **H**alf **M**aximum
HPHT	**H**igh-**P**ressure **H**igh-**T**emperature
HT	**H**igh-**T**emperature
LPHT	**L**ow-**P**ressure **H**igh-**T**emperature
LTM	**L**aser **T**hreshold **M**agnetometer
MWs	**M**icrowaves
NMR	**N**uclear **M**agnetic **R**esonance
NV	**N**itrogen-**V**acancy (center)
ODMR	**O**ptically **D**etected **M**agnetic **R**esonance
PL	**P**hoto**L**uminescence
ppb	**p**arts **p**er **b**illion
ppm	**p**arts **p**er **m**illion
PSB	**P**honon **S**ide **B**and
SCD	**S**ingle **C**rystalline **D**iamond
SIMS	**S**econdary **I**on **M**ass **S**pectrometry
SPAD	**S**ingle-**P**hoton **A**valanche **D**iode
SQUID	**S**uperconducting **Qu**antum **I**nterference **D**evice
UV-VIS	**U**ltra**V**iolet-**Vis**ible (spectroscopy)
WLI	**W**hite **L**ight **I**nterferometry
ZPL	**Z**ero-**P**honon **L**ine

Abstract

The nitrogen-vacancy (NV) center in diamond is a promising quantum platform for magnetometry applications exhibiting optical readout of minute energy shifts in its spin sub-levels even at room temperature. In particular, NV-ensembles in bulk diamonds are favored for a considerably improved signal-to-noise ratio and sensitivity. Key material requirements for general NV-ensemble-based applications are a high NV^- concentration, a long spin coherence time, and a stable charge state. Additionally, for specific applications that require large detection volumes, for example, the multi-pass readout or cavity coupling, a low optical loss in the material is also an essential need, calling for a low diamond absorption and a low birefringence. These requirements, however, are interdependent and can be difficult to optimize during diamond growth and subsequent NV creation. Therefore, better understanding the correlation between these material properties and finding their balances are crucial for improved sensitivity from the material side.

Chemical vapor deposition (CVD) diamonds typically exhibit NV concentrations below 10 parts per million (ppm), but often show a high homogeneity in the NV distribution. Moreover, the nitrogen incorporation during the CVD synthesis can be precisely controlled. With these advantages, the CVD diamond attracts more and more interest in NV research. In contrast, high-pressure high-temperature (HPHT) synthesis with higher NV concentrations (up to dozens of ppm) is also of great interest. However, its inhomogeneity in the nitrogen distribution and less controllability of the nitrogen concentration raise challenges when applying it to the sensing systems.

In this thesis, the author investigates optical, NV and spin properties of diamonds, specifically for CVD diamonds with a wide variety of nitrogen densities but also in comparison with HPHT diamonds. This thesis studies the optimal process in the creation of NV centers and the link to optical properties. The author develops novel optical methods in this thesis to determine the defect concentrations, which are more widely accessible and easier to implement than the conventional methods. Addition-

ally, the author establishes various characterization protocols to systematically study NV and diamond properties. Based on these methods, CVD diamond series with varied nitrogen flow over 4 orders of magnitude are investigated, to understand the incorporation of single substitutional nitrogen atoms (P1 centers) and NV creation during the growth. For a fixed nitrogen concentration, varied electron-irradiation fluences are investigated and optimized for two different accelerated electron energies. Defect transformations during the irradiation and annealing treatments are studied via optical characterizations. The author points out that with increasing fluences a turning point exists, above which mainly the undesirable NV charge state (NV^0) is being created, indicating an optimum that balances the high conversion efficiency and charge stability. A general approach is suggested by the author to determine the optimal irradiation conditions, for which an enhanced NV concentration and an optimum of NV charge states can both be satisfied. Optimizing the treatment, this thesis achieves spin-spin coherence times T_2 ranging from 45.5 to 549 μs for CVD diamonds containing 168 to 1 parts per billion (ppb) NV^- centers, respectively. This enables better combinations of high NV concentrations and long coherence times in bulk diamonds compared to previous works.

Diamond is an excellent host for advanced optical/photonic applications, however, doping can compromise the optical properties significantly. Therefore, the author further investigates relationships and ways of combining high NV concentrations with improved optical properties, specifically absorption and birefringence. Based on this, high temperature (HT) treatments are introduced as a promising candidate to reduce optical loss, while not conflicting with the requirement for high NV^- concentrations. This thesis shows a pathway to engineering properties of NV-doped CVD diamonds for improved sensitivity.

Chapter 1

1 Introduction

The nitrogen-vacancy (NV) center is a point defect in diamond with C_{3v} symmetry, which consists of a substitutional nitrogen atom adjacent to a lattice vacancy [1] (Figure 1.1). It is known to exist in three charge states, i.e. negatively charged NV^-, neutral NV^0 states and positively charged NV^+. While NV^- and NV^0 are mainly observed in natural and synthetic diamonds, NV^- exhibits a spin triplet S = 1 ground state with long spin lifetimes at room temperature, which can be initialized and read-out optically and coherently controlled using microwaves (MWs) [2, 3, 4, 5]. This makes it a promising spin system for quantum sensing [6, 7, 8] and quantum information processing [9, 10, 11]. NV-ensembles with high NV^- concentrations, specifically, are favored for a considerably improved signal-to-noise ratio and sensitivity [12, 13].

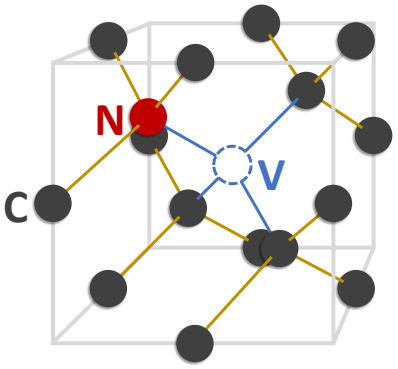

Figure 1.1: Simplified atomic structure of the nitrogen-vacancy (NV) center in diamond.

This chapter firstly gives an overview of NV^- centers for sensing applications, secondly introduces optical and spin properties of NV^- centers, thirdly discusses differ-

ent approaches to create NV-ensembles in diamonds, in the end introduces the main interest and focus of this work: characterization and optimization of NV-ensembles in bulk diamonds.

1.1 Overview: NV centers for sensing

The first detection of electron paramagnetic resonance (EPR) from a single NV defect was reported in 1997 by Gruber *et al.* [14]. Although ensembles of NV centers have been observed prior to 1997, this initial detection of single centers triggered an intense research effort in the context of diamond-based quantum technologies, and the NV center became a popular platform to develop various quantum manipulation protocols [15, 16, 17, 18].

The NV^- center provides long-term photo-stable fluorescence with high luminescence efficiency [19, 20]. Moreover, it exhibits highly-coherent, optically-readable electronic spins. The nature of the diamond lattice with a low magnetic noise protects the NV superposition states from decoherence, enabling its long coherence time. Isotopically pure diamond synthesis can further reduce the decoherence by nuclear spin from paramagnetic ^{13}C isotopes [21]. By engineering the material and spin control techniques, longitudinal relaxation times $T_1 \approx$ 6 ms [22, 23] and coherence times T_2 up to a few ms [21, 24] of NV^- centers are achievable even at room temperature. This is in the electron spin, in the nuclear spin (nitrogen or surrounding ^{13}C) even longer times (up to seconds) can be achieved. The high luminescence efficiency and long spin coherence make NV^- a novel, promising sensing scheme with potentially enhanced sensitivity compared to classical techniques. Key parameters of the NV-diamonds in related works are listed in Table 1.1 for an overview.

In around 2008, the NV^- center has been firstly proposed and demonstrated as magnetic-field sensors [2, 3, 25, 26, 27]. Over the past decade, the sensing of magnetic [3, 28, 29, 30] and electric [31, 32] field, strain [33, 34], temperature [35, 36, 37, 38] and pressure [39] have all been demonstrated with the NV^- center. Its applications cover a wide range including condensed matter physics [40, 41], biology [42, 43], nuclear magnetic resonance (NMR) [44, 45] and scanning probe microscopy [46, 47].

Single NV^- centers enable sensing with high resolution [41, 48, 49, 50]. In comparison, NV-ensembles with high NV^- concentrations and/or large detection volumes

Table 1.1: Key parameters of NV-diamonds in related works.

Reference	$[NV^-]$	T_2[(1)]	NV^-/NV	Type
This work	1-168 ppb	Up to 549 μs	85.5%	bulk
Edmonds *et al.* [59]	~2 ppm	unspecified	62%	bulk
Schloss *et al.* [60]	3.8 ppm	7 μs	65.5%	bulk
Stanwix *et al.* [4]	<0.18 ppb	600 μs	unspecified	bulk
Herbschleb *et al.* [24]	low[(2)]	2.4 ms	~100%	bulk
Lühmann *et al.* [61]	5 ppm	100 μs	unspecified	near-surface[(3)]
Barry *et al.* [51]	1.7 ppm	5.1 μs	unspecified	shallow layer[(4)]

(1) T_2 measured by Hahn-echo sequence.
(2) NV concentration unspecified. Since no nitrogen doping or implantation has been conducted in this work, a low NV concentration is expected.
(3) Spot with a diameter~20 μm, penetration depth<0.1 μm limited by the implantation technique.
(4) Shallow NV-layer of 13 μm thickness in bulk diamond.

are favored for precision magnetometry [26, 27, 51, 52], for a considerably improved signal-to-noise ratio and sensitivity, which both ideally improve with the square root of the number of sensing spins [12, 13]. Therefore, bulk diamonds with NV-ensembles throughout the entire diamond volume are required for many applications such as detecting magnetic nanoparticles [53], battery characterization [54], vector imaging [55, 56], and lasing [57, 58].

State-of-the-art sensitivities at the $\mathrm{pT}/\sqrt{\mathrm{Hz}}$ level can be achieved by NV-ensemble-based magnetometers. Competing technologies with lower sensitivities are often realized as bulkier devices. For instance, superconducting quantum interference devices (SQUIDs) and optically pumped magnetometers (OPM) can both achieve sensitivities at the $\mathrm{fT}/\sqrt{\mathrm{Hz}}$ level and below [62, 63, 64], while their detection volumes are much larger than NV-based magnetometers, which have typical detection volumes in the 100 μm to 1 mm scale Moreover, NV-based sensors can be performed on single spins that are localized within a few Angstroms, which marks their unique advantages to be integrated as compact, portable devices [65, 66, 67, 68, 69]. Additionally, NV sensors can measure on background fields, while OPMs require a zero-field operation environment. NV sensors also have a large dynamic range and linearity when compared to other techniques. All these advantages make NV centers a promising platform for sensing applications.

The main interest and key challenge for the NV-based magnetometry is to improve sensitivity. This should be approached via both developing novel spin control tech-

niques and optimizing the NV-diamond material: this thesis investigates the optimization approach from the material side.

In particular, improved sensitivities and strong signals of NV-ensemble-based sensors call for high NV concentrations, long coherence times, and stable charge states. This requirement is challenging for material optimization since a high NV concentration originates from a high nitrogen content in diamond, but the high nitrogen content plays a role as the main decoherence source of NV centers, leading to a short coherence time. In this sense, a rational strategy to optimize the NV-diamond is to remain a relatively low nitrogen concentration (to obtain a long coherence time), while enhancing the nitrogen to NV conversion ratio (to obtain a high NV concentration). This strategy, however, raises another challenge, that a high conversion ratio often leads to an increase in the undesirable NV charge state (i.e. NV^0), resulting in a worse NV charge state stability. Moreover, high NV concentrations can also lead to unstable optical properties of diamonds, such as diamond absorption and birefringence. The two diamond properties are both crucial for applications requiring large sensing volumes. Consequently, the very essential question for the NV-diamond optimization is to understand the inter-dependencies between these NV and diamond properties. It is systematically studied in this thesis, thus a practical pathway to balance these properties and optimize the NV-diamond is suggested.

1.2 Optical and spin properties of NV centers

Basic optical and spin properties of the NV^- center are described in Figure 1.2. The NV^- electronic structure, Figure 1.2(a), includes two spin triplet states: a ground state of symmetry $^3A_2$ and an excited state of symmetry ^3E; as well as a spin singlet state that involves two levels with symmetries $^1A_1$ and ^1E [5, 42, 70]. Electric dipole transitions between the excited (^3E) and ground ($^3A_2$) states are strongly radiative, creating photo-luminescence that covers the red and near-infrared spectral region, Figure 1.2(c). The main transition between the ground and excited state can be excited by most of the visible wavelengths below 640 nm, and it has a resonant wavelength of 638 nm, which is well known as the zero-phonon-line (ZPL) of the NV^- center. Most of the luminescence, however, is not created by the main transition (which does not appear at the ZPL), but by transitions of vibrational states. This creates broad NV^- phonon side bands (PSB) between 630 nm and 800 nm. The NV^- ZPL with PSB is a crucial optical feature of the NV^- center, thus a useful

tool to identify it in diamonds. NV^0 has a ZPL at 575 nm and PSB from around 560 nm to 700 nm. The NV charge state identification and analysis are based on these features in this work, which will be mainly discussed in Section 2.2.2. Only NV^- centers are of interest for quantum applications, NV^0 centers contribute to the fluorescence background that is undesirable for sensing.

Back to the energy-level diagram of NV^-, Figure 1.2(a), the two triplet states further split into three spin sub-levels, i.e. two degenerate levels $m_s = \pm 1$ and an energetically lower level $m_s = 0$. Optical transitions are strongly spin preserving, meaning that the spin state stays consistent while cycling between the ground and excited state. Nevertheless, the electron in the excited $m_s = \pm 1$ states has a significant chance to undergo a non-radiative inter-system crossing via the singlet state to the ground $m_s = 0$ state due to the spin-orbit coupling. In contrast, electrons in the excited $m_s = 0$ state mostly decay via the fast radiative transition. Given that the lifetime of the metastable singlet state (250 ns [5, 71]) is over one order of magnitude longer than the radiative lifetime of the excited state (12-13 nm [70, 72, 73]), the $m_s = 0$ is slightly brighter than the $m_s = \pm 1$.

Although optical transitions are spin-preserving, a transition within the ground state from the $m_s = 0$ to $m_s = \pm 1$ states can be realized by applying microwaves at the resonant frequency, which has been firstly established by Gruber *et al.* [14]. The resonant frequency is defined by the energy difference between $m_s = 0$ and $m_s = \pm 1$, which is intrinsically $D = 2.87$ GHz for the ground state, Figure 1.2(b). D here is called zero-field splitting. Magnetic fields can split $m_s = \pm 1$ states (Zeeman effect) by a factor of $2\gamma B$, where γ is the electron gyromagnetic ratio, and B dedicates to the magnetic field projected onto the high symmetry axis of NV^- (connecting line between vacancy and nitrogen, (111) crystal direction) [20, 40]. In this case, the $m_s = 1$ and $m_s = -1$ state are no longer degenerate but shift in opposite directions. They show varied energy gaps to the $m_s = 0$ and exhibit different resonant frequencies.

This magnetic field dependence lays the foundation for all NV-based magnetic sensing applications. When slowly sweeping the microwave frequency, the transition from the 'bright' ($m_s = 0$) state to the 'dark' ($m_s = \pm 1$) state occurs at the resonant frequency, resulting in less fluorescence intensity, i.e showing a 'dip', Figure 1.2(d). Without the magnetic field, only one dip appears at 2.87 GHz corresponding to the zero-field splitting D. With magnetic fields, the signal shows two dips corresponding to the two resonant frequencies of $m_s = 0 \leftrightarrow m_s = -1$ and $m_s = 0 \leftrightarrow m_s = 1$.

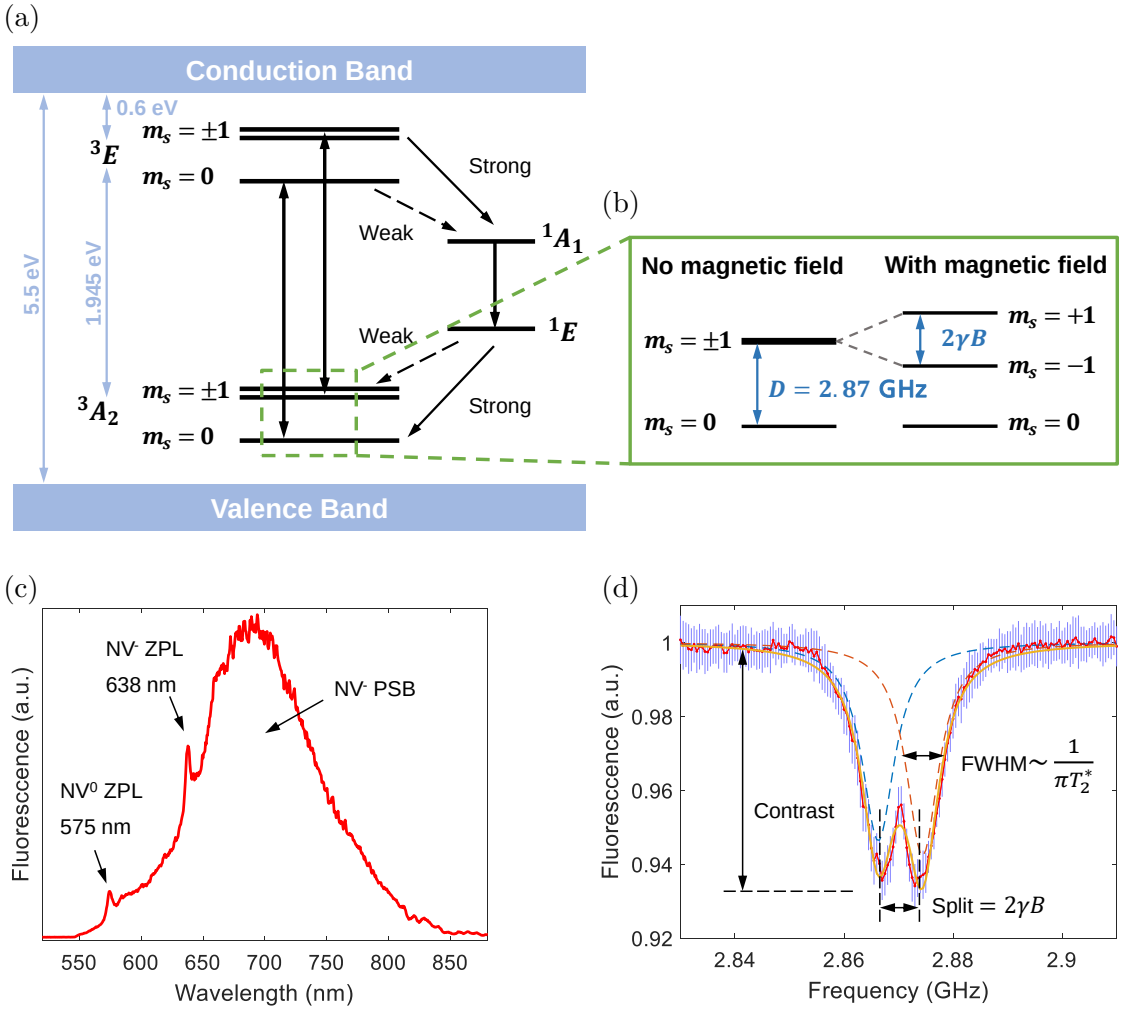

Figure 1.2: Illustration of the basic optical and spin properties of NV centers. (a) Energy level diagram for the NV^- center including two spin triplet states ($^3A_2$ ground state and ^3E excited state) and a metastable singlet state (with symmetries $^1A_1$ and ^1E). (b) Zero-field splitting $D = 2.87$ GHz (no magnetic field) and Zeeman splitting $2\gamma B$ (with magnetic field) between ground state sub-levels $m_s = 0$ and $m_s = \pm 1$. (c) Emission spectrum of the NV center, showing the NV^- zero-phonon-line (ZPL) at 638 nm and phonon side bands (PSB) at 630-800 nm, and NV^0 ZPL at 575 nm. (d) Optically detected magnetic resonance (ODMR) spectrum showing the Zeeman splitting.

By measuring the splitting between the two dips, one can detect the strength of the magnetic field. This is so-called optically detected magnetic resonance (ODMR), which is a characteristic effect of NV^- centers and has been rarely observed for other molecules or defects [74].

ODMR experiments can be approached either with continuous-wave (CW) or pulsed.

Pulsed experiments have higher sensitivity, where a laser pulse is used to initialize the spin state and read it out at the end, and an MW pulse is used to flip the spin state precisely from 0 to 1 on resonance. The sensitivity is proportional to the coherence time τ. The coherence time τ represents the period that the coherent superposition states of the ground state $m_s = 0$ and $m_s = \pm 1$ levels last. There is a distinction between the shorter time T_2^*, which is relevant to DC measurements, and the longer T_2 time, which is achieved by dynamical decoupling pulse sequences that remove slowly varying environmental noise (magnetic field variations). This leads to different considerations for sensitivity when driven by different techniques [13, 75]. For the material side, comparing NV coherence times using the same protocol is essential to evaluate the material quality. Material considerations for sensitivity will be discussed in detail in Section 3.1.

1.3 NV creation procedures

As discussed above, the NV^- center possesses plenty of characteristics favored by quantum technologies, such as its special optical and spin properties, operability at room temperature, biocompatibility, and initialization simplicity. The fact that it can be easily produced also benefits its investigation and application. Different techniques are applied to create NV centers, all with the same prerequisite of high-quality diamonds. Another prerequisite is the isolated-substitutional-nitrogen atoms (called P1, N_s^0, or C centers), from which forms the NV center by trapping a nearest-neighbor lattice vacancy [76, 77]. This section introduces mainstream diamond synthesis methods and techniques for nitrogen incorporation and NV creation.

1.3.1 Diamond synthesis

High-pressure high-temperature (HPHT) growth and chemical vapor deposition (CVD) growth are the two mainstream diamond synthesis methods nowadays. Here their procedures and main differences are discussed respectively.

HPHT synthesis

HPHT growth proceeds at high temperatures and pressures that imitate the conditions to form natural diamonds. It is often created at a temperature of 1300-1600 °C and a pressure of 5-6 GPa [78]. A diamond seed is placed in the reactor, under a carbon source such as graphite or diamond powder. During the growth, a molten metal catalyst dissolves the carbon source, which is then transported to the diamond seeds and precipitates. HPHT growth can come with a large nitrogen content (up to several hundreds of ppm) due to the contamination of the metal solvent-catalysts. It often shows strong variations in nitrogen densities between crystals grown under the same conditions, and shows sectors with vastly different P1 concentrations and other properties in a single crystal, due to the different nitrogen incorporation efficiencies along different growth directions during synthesis [79].

CVD synthesis

CVD growth, as its name implies, involves a chemical reaction inside a gas phase as well as deposition onto a substrate surface [80]. A diamond substrate in the reactor is exposed to a hydrogen-methane (H_2-CH_4) gas mixture. By heating this gas mixture (using a microwave beam or a hot filament), a plasma is created and carbon atoms then deposit onto the substrate and form the diamond layer. CVD growth allows for well-controlled nitrogen-doping by setting the gas flow to the reaction chamber, typically at a lower end of nitrogen doping levels compared to HPHT growth. Nevertheless, it can realize a high homogeneity of nitrogen incorporation due to growth in a single crystalline direction and more precise control over the desired nitrogen density and thus NV coherence time. In particular, during CVD growth a small fraction of P1 centers trap vacancies and form NV centers directly. Thus CVD diamonds unlike HPHT diamonds contain higher NV densities directly after growth and without irradiation and annealing steps. This makes the as-grown, NV-doped CVD diamond favored for some applications, for technological simplicity.

To significantly enhance the NV creation in both HPHT and CVD diamond, after-growth treatments play a crucial role, which is discussed in the following section.

1.3.2 After-growth treatments for NV creation

According to different application focuses, the growth of nitrogen-doped or intrinsic ('pure') diamonds can be of interest. Nitrogen-doped growth results in a nitrogen distribution throughout the entire diamond crystal, which is normally followed by an irradiation and annealing step to further create NV centers. This is normally favored for applications that require NV-ensembles in bulk diamonds. In contrast, to create NV centers in intrinsic diamonds, an ion-implantation treatment is often applied, to implant nitrogen atoms (and/or other n-type impurities). This can create shallow NV-ensemble layers or small groups of NV centers at predetermined positions.

Irradiation and subsequent annealing

For nitrogen-doped diamonds, P1 centers are enriched in the entire diamond plate. Irradiating them with electrons, ions, high-energy photons or neutrons [1, 81, 82, 83] creates vacancies. When annealing the irradiated diamonds above 800 °C, vacancies are highly mobilized [1, 84] and trapped by P1 centers to form NV centers [27, 85, 86]. Among all these irradiation particles, the electron is mostly applied, as it can create vacancies homogeneously and deeply into the diamond (with a penetration depth up to millimeters [83]). Furthermore, it mainly creates isolated vacancies but not multi-vacancies or vacancy clusters [13], while preventing further crystal damages. These make the electron-beam irradiation a favorable tool to create NV-ensemble in the bulk diamond plate, which normally has a thickness from hundreds of microns to more than one millimeter.

It is worth mentioning that when using lower energy, focused electron-beam, the precision creation of NV centers can be also achieved [87], but at the cost of losing the penetration depth.

Ion-implantation

Intrinsic diamonds do not contain sufficient nitrogen content to form detectable NV centers. For these diamonds, ion-implantation, in particular with nitrogen ions introduces substitutional nitrogen atoms and vacancies in diamond [88]. It is a powerful tool to spatially control the creation of NV centers, while its penetration depth can be limited in the nm level [89, 90]. Surface damages caused by high energy ion-implantation are another concern when applying this kind of technique.

Subsequent annealing is also needed to combine nitrogen atoms with vacancies to form NV centers, which is similar to the treatment process with e-beam irradiation. Additionally, it has been suggested that the annealing process turns other defects mobile and potentially migrates to the surface, which repairs damage to the crystal caused by implantation [89].

Different approaches are adapted to create NV centers in desired platforms. As some examples, to create NV-ensembles throughout a large volume of the bulk diamond, the most efficient procedure is to irradiate (with high-energy electrons) and anneal the nitrogen-doped diamond. While to create shallow NV layers, one can either ion-implant and anneal the intrinsic diamond, or grow a thin diamond film with nitrogen doping, then followed by an irradiation and annealing step. Engineering the combination of the synthesis method and after-growth treatments is a crucial part of the creation of NV-diamond.

1.4 Focus and outlook of this thesis

The creation of NV centers is highly relevant to all NV research. This thesis studies the formation of NV centers in the repeatable homogeneous CVD process and subsequent treatments, specifically the e-beam irradiation and annealing steps. The NV concentration, charge state distributions, and coherence times are investigated as a function of the creation parameters and over a large range of nitrogen concentrations. These NV properties are investigated in the context of NV ensembles for a wide interest in sensing and improved sensitivities. In sensors with large volumes, optical properties of the diamond are also highly relevant, especially for schemes such as multi-pass readout, cavity coupling, etc. Therefore, this thesis also studies the absorption and birefringence of nitrogen-doped diamonds throughout the creation process, in relation to nitrogen and NV densities, and investigates ways to improve these parameters.

For NV-ensemble-based sensing applications, sensitivity benefits from high NV^- concentrations. The requirement of high NV^- concentrations raises several concerns:

1. High NV^- concentrations originate from an enhanced nitrogen content in diamonds, which is also the main decoherence source of the NV spin that limits the coherence time T_2 [91, 92, 93] for quantum manipulation and sensing.

2. Pursuing high NV concentration by converting P1 centers into NV centers is often accompanied by the increase of NV^0 concentration, which deteriorates the charge state stability.

3. Impurities in diamonds introduce more uncertainties in terms of both the structural and spectral quality. Specifically, the impact of high nitrogen content on diamond absorption and birefringence needs to be carefully considered for applications that require large sensing volume, since all optical readout suffers from the absorption and sometimes also from the birefringence in the material.

The competing parameters create challenges when combining high NV^- concentrations with long coherence times, which are both key factors for improved sensitivity in magnetic field sensing [40, 94]. They also raise a question mark about how to obtain high NV^- concentrations with low absorption and low birefringence, which are the essential requirements of laser applications–higher gain, lower loss.

This thesis focuses on material optimization including three main parts: The first part introduces characterization methods that are highly relevant for the defect investigation; the second part investigates how to achieve improved combinations of NV^- concentration and coherence time in bulk diamonds; then the final part discusses how nitrogen content and each treatment step influence the diamond absorption and birefringence. The chapters are arranged as follows:

Chapter 2 introduces characterization methods to determine nitrogen-related defect densities, with a focus on P1 and NV centers. The author establishes two novel methods to determine respectively P1 and NV concentrations, based on the defect emission and absorption spectroscopy. Additionally, this chapter discusses other established methods for the determination of these two defects, as well as other relevant nitrogen-related defects such as NVH centers, multi-nitrogen or nitrogen aggregations (e.g. A and B centers), NVN centers, and the total nitrogen concentration. The methods introduced in this chapter lay a foundation for the characterization and analysis in later chapters.

Chapter 3 shows the characterization of as-grown CVD diamonds to investigate the incorporation of P1 and NV centers, as well as NV charge state distributions. The chapter firstly discusses the material consideration for sensitivity, in order to better understand the goal for material optimization. Starting from that point, several CVD diamond series have been grown in a single reactor, with a varying nitrogen flow over 4 orders of magnitude, leading to a broad range of P1 densities from 0.2 to

20 ppm. Moreover, coherence time T_2 of the NV center after growth is investigated, and the connection between P1 density and T_2 after growth is shown. This chapter shows the capability of as-grown NV-doped CVD diamonds as a sufficient material for some sensing applications.

Chapter 4 explores the e-beam irradiation and subsequent annealing, finds the mechanisms of the NV creation and charge state behavior through these treatments then defines an optimum. Continuing the systematic investigation in Chapter 3 (which discusses a large range of nitrogen-doped growth), this chapter investigates the same nitrogen concentration but varied e-beam irradiation and annealing conditions. Two diamond series of the same nitrogen concentration are discussed in this chapter, with a wide range of irradiation fluence and with two separate energies. While in many other investigations one or very few samples are studied and hardly a single parameter is varied. Conventional procedures for NV creation pursue mainly a high P1 to NV centers conversion and a high concentration of total NV centers. The simultaneous reduction of the favorable NV^- charge state often has been ignored. Here through the irradiation, this chapter studies the increase in NV centers as well as the change in charge state distribution. The aim is to balance the increase of NV density with maintaining a high NV^-/NV ratio. From this, general approaches are suggested to determine the optimal irradiation fluence for different nitrogen densities. Furthermore, coherence time changes are investigated after irradiation and annealing. Through irradiation and annealing treatments, the change in T_2 is monitored with the aim to increase the NV density without compromising T_2. This chapter discusses combinations from high NV^- with short T_2, to low NV^- with long T_2, which help to identify the appropriate combination to achieve the optimal sensitivity for different applications.

Chapter 5 and Chapter 6 then study the diamond absorption and birefringence respectively. All optical readout suffers from absorption, advanced techniques such as multi-pass readout, optical cavity coupling, or laser cavity sensing require specifically low absorption, and optical modes also suffer from birefringence in the material. Therefore, this chapter discusses the absorption coefficient at 700 nm, where most of the NV^- fluorescence is present; and the average birefringence Δn in the center region of the samples. Possible causes of them and their behavior for different nitrogen doping levels are discussed. This chapter further shows a series of results to study their changes via e-beam irradiation and annealing, in order to find the direction to improve them thus reducing the optical loss in the material. Additionally, two promising high-temperature (HT) treatments are investigated, i.e. low-pressure

high-temperature (LPHT) and high-pressure high-temperature (HPHT) annealing. Via spectral study, the results show their positive impact on reducing diamond absorption. A well-performed HT treatment also shows the potential to maintain a stable (or even improved) birefringence. These make HT treatments a useful tool, which can be considered as a pre-treatment process (before irradiation) for improved diamond quality.

Material characterization always contains a wide variety and a large amount of experimental work. The systematic study can not be established without the help of experts on different specific techniques. Additionally, some of the experiments can be only conducted externally due to the equipment availability. Here the author specifies the part of experimental works that are done by the collaborators, and acknowledges the contribution from them:

CVD diamond growth in this thesis is done by Julia Langer and Volker Cimalla (Fraunhofer IAF, Germany). EPR measurements are conducted by Brett C. Johnson (RMIT University, Australia) and Rémi Blinder (Universität Ulm, Germany). E-beam irradiation (2 MeV) and a part of the annealing treatment are conducted by Takeshi Ohshima, Shinobu Onoda and Shuya Ishii (QST, Japan). All Hahn-echo measurements included in this thesis are done by Di Wang and David A. Simpson (University of Melbourne, Australia). LPHT annealing is conducted by Alexandre Zaitsev (College of Staten Island, the City University of New York, U.S.). E-beam irradiation with 1 MeV and HPHT annealing are conducted commercially. Important parts of the analysis and discussion in this thesis are based on these experimental works and the knowledge behind that contributed by the collaborators. Beyond that, many other experts also support this characterization work, who are respectfully mentioned in Acknowledgement.

The research concept, the designing of overall processing procedures, the data analysis and discussions and visualizations (plots and schemes) are the work of the author. Additionally, the author establishes new optical methods (Chapter 2) from the concept and the algorithm, to the experimental verification and calibration. The establishment of standard optical characterization method (PL, UV-Vis, Birefringence, etc.) are done by the author, as well as a large number of optical experiments, which acquires enough data as a foundation to establish characterization protocols in house, and enables the investigation of the interdependency between different diamond properties. Parts of the results in this thesis have been published as journal articles, which are listed in the Publication of the author.

Chapter 2

2 Determination of defect densities in diamond

Different NV-related applications call for different NV-doping levels and formats in bulk diamonds. For instance the NV-lasing requires high NV concentrations throughout the entire diamond volume [95, 58, 57], the NV-based wide field microscopy requires shallow NV-ensemble layers [57, 96], the scanning NV magnetometry then needs the precise creation of single NV centers [2, 97, 98, 41]. The determination of NV density in diamonds is always an essential question, especially for NV-ensemble applications. Moreover, knowing the NV concentration is also a very first step to understand NV creation in the diamond during the growth and after-growth treatments. Besides, knowledge of the density of single substitutional nitrogen atoms (called P1, N_s^0 or C-centers in different contexts) also gives significant advantages in the choice of material and performance in applications: P1 centers are the prerequisite to create NV centers (Section 1.3), they provide electrons to charge the desired NV^- state, and their doping levels remarkably influence the sensitivity. Although the determination of NV and P1 concentrations plays such an important role in the application, there are still many missing pieces and difficulties in related characterization. Reliable, precise and rapid methods to determine the density of P1 centers and NV (NV^- and NV^0) centers play a crucial role in NV research.

This chapter gives a review of established methods to determine the P1 and NV concentrations, introduces novel methods and lays the foundations for significant improvements and better materials insight. Additionally, general methods to determine other nitrogen-related defect densities are also discussed, such as the total nitrogen density, nitrogen aggregations and NVH centers.

2.1 Determining P1 concentration

Single substitutional nitrogen atoms (called P1, N_s^0 or C-centers in different contexts) are the prerequisite to create NV centers (Section 1.3), they are doped during the diamond growth or implanted on the diamond surface, followed by irradiation and annealing steps to create vacancies and allow NV centers to form. They play a role as the typical electron donor to charge the desired NV^- state [99, 100, 90, 101], and they determine the NV charge stability. Optimizing the P1 to NV^- conversion ratio is crucial for improving the NV center's performance and sensitivity (Section 3). Moreover, at ppm levels and above they can act as the main decoherence source of the NV center [102].

This section discusses the general way to determine the P1 concentration through three mainstream methods: electron paramagnetic resonance (EPR), Fourier-transform infrared (FTIR) and UV-Visible (UV-Vis) spectroscopy. Among them, EPR is well established and used as a measurement standard [103, 104, 105]. While the other two optical methods, due to their experimental simplicity and widespread availability, are also favorable in some cases. In addition to the general introduction of the established methods, a novel fitting method for the UV-Vis spectrum is developed in this section, which enables a rapid, reliable and precise determination of the P1 concentration.

2.1.1 Established methods: EPR and FTIR

EPR spectrometers measure the absorption of electromagnetic radiation. In measurement, a varied magnetic field and a fixed microwave frequency are typically applied. By sweeping the magnetic field (from small to large), the state energy difference of the electron (Zeeman splitting) widens until it matches with the microwave radiation, resulting in the absorption of the radiation (as a peak of the signal). A phase-sensitive detector is used in EPR spectrometers, which converts the normal absorption signal to its first derivative. Therefore the typical EPR signal is presented in the form of the first derivative of the absorption rather than a simple peak, and the spectrum passes through zero corresponds to the peak of absorption spectrum, Figure 2.1. To determine the P1 concentration, double integration of the EPR signal is taken to determine the EPR peak intensity [106], then by comparing it with a spin reference one can deduce the P1 concentration.

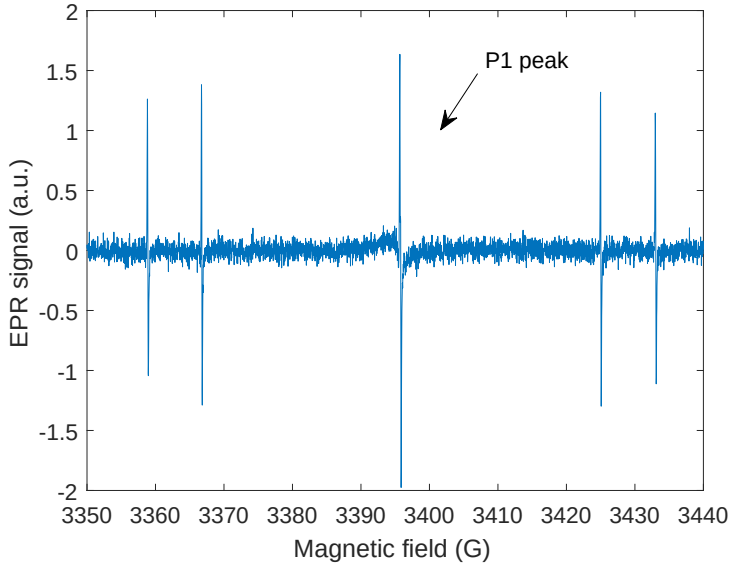

Figure 2.1: EPR spectrum for P1 centers. On the x-axis, it is the swept magnetic field, and on the y-axis the EPR signal represents the derivative of the imaginary part of the molecular magnetic susceptibility with respect to the external static magnetic field. Double integration of the P1 peak is taken to estimate the P1 concentration.

This method has been well established, it measures the absolute spin numbers in the sample, thus it does not require the same type of diamond to be the reference, any 'spin reference' or a pre-defined spin counting function is sufficient in order to calculate the P1 concentration. Therefore this method is often used as a standard to calibrate other methods. However, it is often hard to access and labor-intensive, and its high requirement in the surface quality of diamond brings technical difficulties for the measurement. Moreover, it measures the spin number in the entire sample volume and averages different areas in the sample. For diamonds with less homogeneity, e.g. high-pressure-high-temperature (HPHT) diamonds that usually show sectors containing very different P1 concentrations in a single crystal [79], the spatially resolved determination of the P1 density is highly relevant and more precise than the averaged value. For a normal diamond plate with the typical volume of 3×3×0.3 mm, the conventional EPR measurements can normally estimate P1 concentration higher than ∼1 ppm, the estimation for lower concentrations is often more challenging and brings larger fitting errors.

In a FTIR absorption spectrum, P1 center has a main feature as a sharp peak at 1344 cm^{-1} and a relatively narrow band at 1130 cm^{-1} [107], Figure 2.2. The relations to estimate the P1 concentration [P1] from these two features have been suggested

in [107] as

$$[P1] = (25 \pm 2)\mu_{1130} \tag{2.1}$$

$$[P1] = (25 \text{ to } 50)\mu_{1344} \tag{2.2}$$

where μ is the absorption coefficient in cm^{-1}, and [P1] is in ppm/cm^{-1}. The exact deduction and fitting process have not been stated in their work, and how these relations are influenced by surrounding bands has not been discussed in detail.

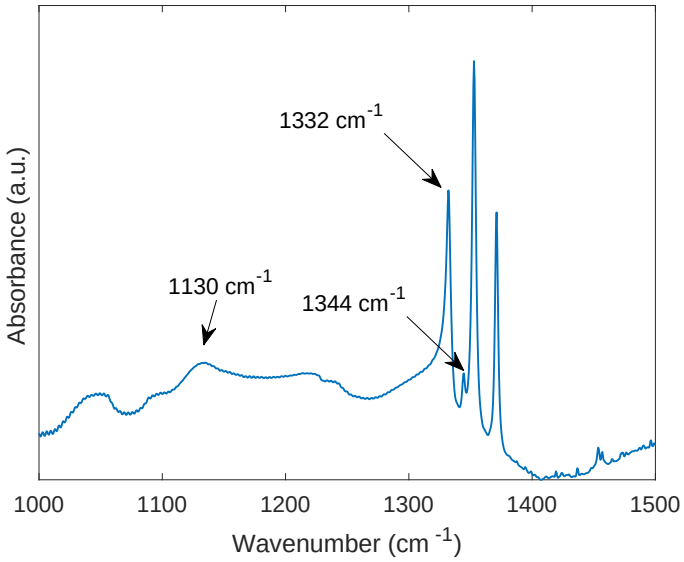

Figure 2.2: FTIR spectrum for P1 (1130 cm^{-1} and 1344 cm^{-1}) and N_s^+ (1332 cm^{-1}) centers.

Close to the two features for the P1 center, a sharp peak at 1332 cm^{-1} that relates to the N_s^+ center [76] also plays an important role. The concentration of N_s^+ centers potentially influences the P1 to NV conversion and the NV charge state [59]. Similar to Equation 2.1, the N_s^+ concentration $[N_s^+]$ in ppm can be deduced from this peak with the relation [76]:

$$[N_s^+] = (5.5 \pm 1)\mu_{1332} \tag{2.3}$$

To observe these peaks, a good enough spectral resolution is needed. It has been found in [108] that the resolution of the spectrometer has a significant effect on the calculation of the concentration. Moreover, for diamonds with low nitrogen densities less than a few tenths of ppm), the conventional FTIR spectroscopy often shows insufficient sensitivity in detecting these nitrogen-related centers [107]. In comparison, as we will see below the UV-Vis spectroscopy enables the detection

of single nitrogen as low as 0.01 ppm [109], which is much below the detection limit of the conventional FTIR method. Furthermore, UV-Vis spectroscopy with its experimental simplicity can be applied as a rapid method to characterize diamonds, especially for low nitrogen concentrations.

2.1.2 Determining P1 concentration by UV-Vis

For as-grown CVD diamonds, their UV-Vis spectra often exhibit three typical absorption bands (Figure 2.3): A band centered at 270 nm that links to P1 centers [110, 111, 112]; a band centered at 360 nm originates from vacancy clusters [113, 114]; and a 520 nm band that has been assigned to NVH^0 centers [113].

For untreated HPHT Ib diamond, normally no significant 360 nm and 520 nm bands appear, as the related defects are potentially dissociated under the high temperature during the synthetic procedure. Instead, an absorption continuum of the 270 nm band (reaching from around 300 nn to around 500 nm) is often clearly observed [107]. It has been suggested that this absorption continuum accompanies the 270 nm band, however, it locates at the same regime as the 360 nm band in CVD diamonds, they cannot be distinguished from each other (and there is no clear conclusion if the continuum even exists in CVD diamonds). In this sense, although for HPHT diamonds both the 270 nm band and its continuum have been used to determine the P1 concentration [109], while for CVD diamonds only the 270 nm band itself can be used.

Regarding the analysis of the 270 nm band in CVD diamonds, different fitting methods have been introduced. The key requirement is to separate the band from the underlying and surrounding features. The typically complex spectra with multiple features lead to difficulties to determine the band reliably. Assuming a linear slope as the underlying feature in the visible spectrum, Sumiya *et al.* [115] has suggested early on to subtract the spectrum at 270 nm with the 'tail-line', then calibrate this height with the EPR result. The 'tail-line' is a straight line fitted with the acquired spectrum at around 600-800 nm (the 'tail'), so its slope is changed by the 'tail'. This method is very limited to diamonds that have no additional spectral components at the 'tail' region, any additional components across the range (for example NV^-, NVN^- centers, or the Ni-related broad band centered at 710 nm, etc.) would invalidate it. For CVD diamonds, a perfect 'tail' without influence by other defects is unusual and difficult to achieve in nitrogen-doped growth.

A more recent protocol has been introduced by Khan *et al.* [113, 114], which relied on more complex fitting components: a 'ramp' in the form of λ^{-3} that fits well to the overall decreasing trend of the absorption spectrum (which can be related to single vacancies [116] (Section 4.4), or vacancy clusters [117, 118]); a combination of bands at 360 nm and 520 nm; and a 'reference spectrum' including the 270 nm band and its absorption continuum taken from a high-pressure-high-temperature (HPHT) type Ib diamond. The weight of the 'reference spectrum' then gives the strength of the 270 nm band and thus the P1 concentration. This protocol improved the fitting accuracy significantly, nevertheless, it largely relies on the HPHT reference spectrum, meaning one must obtain a suitable HPHT Ib diamond with a detectable, clear 270 nm band. Besides, the author points out that HPHT spectra have their own 'ramp' component and potentially other spectral features. Using these as the reference will not only isolate the 270nm peak but also fit the other components of the reference to the acquired spectrum, deteriorating the fitting accuracy and likely creating a dependency on which HPHT reference spectrum is used. Furthermore, considering the fundamental difference in material properties between different diamond syntheses, using a reference spectrum from HPHT diamond to fit for CVD diamonds can induce more uncertainties.

This section introduces an improved fitting protocol for the 270 nm band, which can be better adapted for complex spectra, especially for CVD diamonds. The results of this section lead to the publication [119] of the author. This new method avoids the requirement for an ideal HPHT reference spectrum and increases the fitting robustness. The diamond transmission T is measured in the range of 200-800 nm using an UV-Vis spectrometer (PerkinElmer Lambda950, standard detector) at room temperature, then the absorption A is deduced following the Lambert-Beer law:

$$A = -\log_{10}(T)/d \tag{2.4}$$

where d is the sample thickness.

Figure 2.3a shows a typical UV-Vis absorption spectrum of CVD diamonds, containing three absorption bands centered at respectively 270 nm, 360 nm and 520 nm. This thesis fits the spectrum with five components (Figure 2.3):

- Three Gaussian functions for the three bands:

  $g_j(\lambda) = a_j \cdot \exp\left(-(\lambda - b_j)^2/(2c_j^2)\right)$, where a_j, b_j and c_j are the fitting parameters for each band j=270, 360, 520 (nm). Here 270 nm is the band of interest to

extract the P1 concentration, 360 nm corresponds to vacancy clusters and 520 nm to NVH^0 centers [114].

- A 'ramp' function $r(\lambda) = R \cdot \lambda^{-3}$ (same as in [113]), where the factor R is the fitting parameter for this function.
- A spectrum 'El-offset', $e(\lambda)$, which is given by an electronic grade diamond (theoretically a 'pure' diamond without defect bands in the UV-Vis range). This reference spectrum is applied as an offset and baseline to the acquired spectrum, and it is also fitted with a coefficient d.

A sum of the five components was fitted to the original spectrum by a non-linear least squares fit: $Fit = g_{270}(\lambda) + g_{360}(\lambda) + g_{520}(\lambda) + r(\lambda) + d \cdot e(\lambda)$

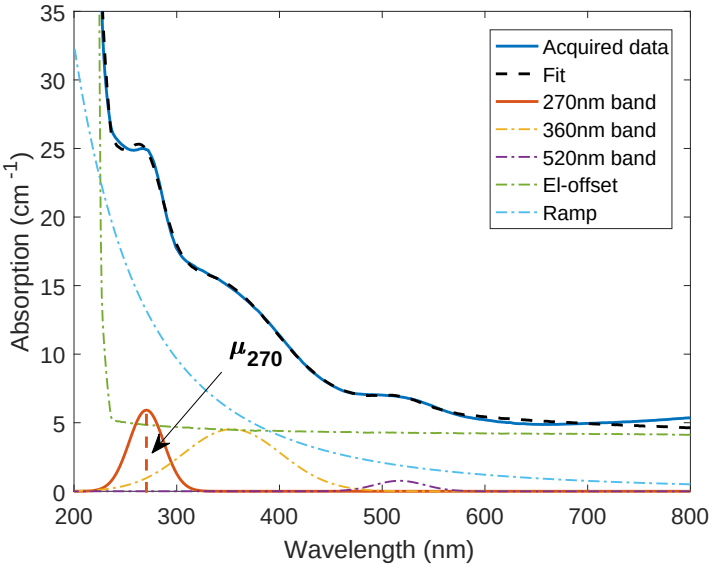

Figure 2.3: Fitting for the UV-Vis absorption spectrum including three Gaussian bands at 270 nm, 360 nm and 520nm, a 'ramp' function and an electronic-grade diamond spectrum as the offset. The 270 nm band (red solid curve) can be taken as a direct indication of the concentration of P1 centers.

The 270 nm feature is extracted as a Gaussian band in this method. For this band (i.e. $g_{270}(\lambda)$ function), a lower- and upper boundary of the fitting parameter have been introduced for the band-center b_{270} (268-272 nm) and the Gaussian RMS width c_{270} (13-27 nm), in order guide the algorithm to optimize the parameters in a small range. The boundaries were selected based on free fitting results of a large number of samples, they also help to examine whether the fitting outcome exhibits reasonable values: if a final parameter is on the boundary value, this indicates an

unreliable fitting performance, i.e. the boundary has 'forced' the algorithm to stop while no optimization has been found in the expected range. On the contrary, if the final parameter exhibits a free value in the given range, the fitting was optimized correctly.

With extracting the 270nm band, one then compares its height, μ_{270} (in cm^{-1}), as an indication of relative P1 densities. To obtain the absolute value of the P1 concentration, the results was calibrated with EPR measurements, which will be discussed in the following paragraphs in this section. In this method, no reference sample with an ideal 270 nm band is required, the only reference spectrum in this method is the 'El-offset' component measured from the electronic grade diamond. This lowers the difficulty and variation of implementing the fitting, as a 'pure' diamond with a 'transparent' spectrum feature in the UV-Vis range is easy to obtain. It greatly avoids introducing undesired spectral components that vary from diamond to diamond, while keeping the diamond intrinsic spectral feature (with an absorption edge at around 225-235 nm, then being 'flat' in the visible range up to 800 nm), instead of using a straight line as the offset. Considering that the 270 nm band is located very close to the absorption edge (∼225-235 nm), the El-offset feature is required to properly fit the sharp drop in this regime and is necessary to supplement the 'ramp' function. In this sense, inducing the 'El-offset' can considerably improve the fitting performance.

For a spectrum with a weak or undetectable 520 nm band, the fitting method can be also adapted to four components. This can help to improve the fitting accuracy for some samples, as the fitting parameters for $g_{520}(\lambda)$ should be nearly zero in this sense, subtracting this band in the fitting function reduces unnecessary fitting parameters.

To calibrate the method, six (100) oriented CVD diamonds have been grown with varying nitrogen-doping levels (Nitrogen series #2, details see Appendix A). Their P1 concentrations were measured with an EPR spectrometer (Bruker ELEXSYS E580) at room temperature (P1 results see Table 2.1). The spectrometer was fitted with a Bruker super-high-Q probe head (ER4122 SHQE), and the microwave frequencies were set to 9.84 GHz. P1 concentrations were determined using the built-in spin-counting feature (pre-calibrated by the manufacturer), from the acquisition software (xEPR). This measurement for P1 concentration carries an error of around 6%. Later on, the UV-Vis spectrum of all the six samples is measured and fitted, Figure 2.4. They all show a good match between the fitting result and the

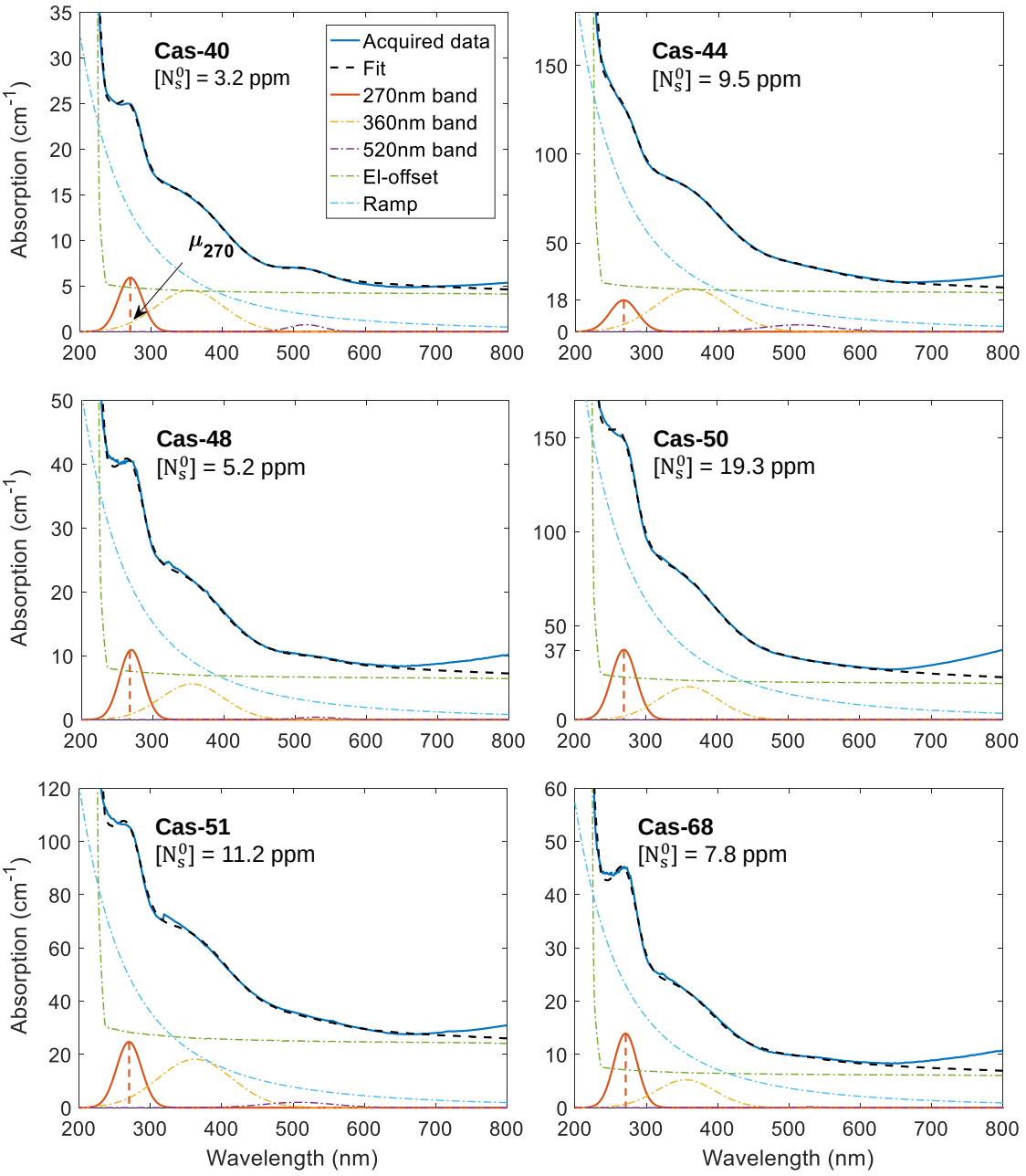

Figure 2.4: Fitting result for six samples with different P1 concentration. Details of the P1 concentration and the peak height of 270 nm see Table 2.1.

original spectrum. Mismatches appear at the high wavelength (>650 nm), which is due to higher spectral features that are not included in the fitting. A possible candidate for these CVD diamonds can be H2 centers (NVN^-) with a zero-phonon line at 986 nm and a broad phonon side band centered at around 800 nm. For samples with strong features in this higher-wavelength regime (i.e. Cas-48, Cas-50 and Cas-68), a cut-off at 650 nm for the acquired data (i.e. fit for 200-650 nm) can improve the fit-

ting performance. The good fitting result at a lower wavelength shows that the new method is independent of higher spectral features. The spectral variation around 650-800 nm illustrates the problem with defining a 'tail' as a baseline reference for the 270 nm peak [115].

Then the height of the extracted 270 nm Gaussian peak, μ_{270}, is compared to the EPR result (Fig. 2.5). The good agreement between the two methods is shown by the close-to-linear arrangement of the data points, proving the reliability of the fitting method. However, earlier research has suggested that the 270 nm band can be influenced by both N_s^0 (P1) and N_s^+, especially for diamonds with low nitrogen concentrations [77]. While multiple papers have ignored this and used the 270nm peak to determine N_s^0 only [113, 114, 59], the possibility has never been fully ruled out. Although the results can also not fully eliminate the possibility of a contribution of N_s^+, the good linear fit of the EPR and UV-Vis results indicates that N_s^+ has a minor influence if any. The discrepancies between the two methods in some previous works might have arisen from an inadequate fitting method for the spectrum. Data details see Table 2.1.

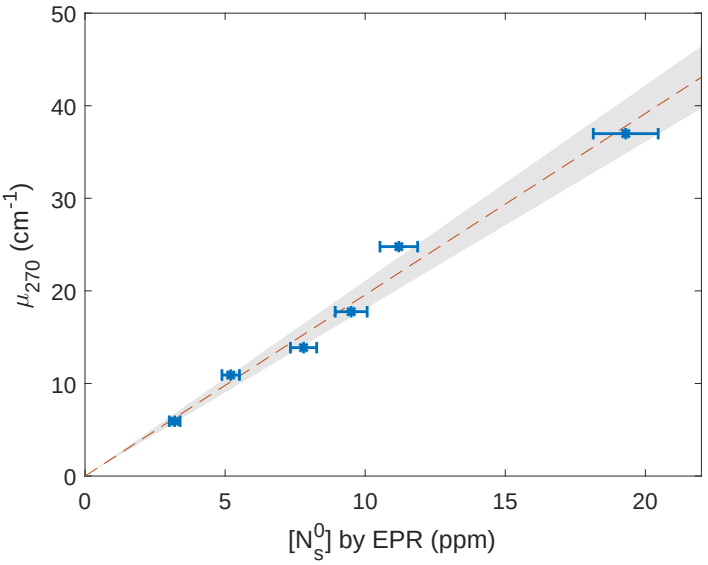

Figure 2.5: The UV-Vis result by the new fitting method is well aligned to the EPR result, showing a linear correlation. The linear fit shows a slope of 1.96±0.15 cm^{-1}·ppm^{-1}, the error is given by 95% confidence interval of the fitting parameter (gray area in the plot).

From the slope in Figure 2.5, one can deduce the absorption cross-section σ of the

P1 center at 270 nm, with the relation:

$$\mu_{270} = \sigma \cdot [P1] \tag{2.5}$$

where $[P1]$ is the P1 concentration in ppm, μ_{270} is the absorption coefficient of the extracted 270 nm band height (as described above). For common logarithm (i.e. decadic absorption coefficients), the absorption cross-section $\sigma = 1.96 \pm 0.15$ cm^{-1}·ppm^{-1}, the error is given by 95% confidence interval of the fitting parameter for the linear fit to the two methods. For the absorption coefficient calculated by natural logarithm, an absorption cross-section $\sigma_e = 4.51 \pm 0.35$ cm^{-1}·ppm^{-1} should be applied instead. In previous research, a single reference of the absorption cross-section at 270 nm is found [107], which has been stated as $1/\sigma$=0.6±0.1 ppm/cm^{-1}. However, the method of its determination, specifically how the spectrum has been separated was not stated.

Table 2.1: Details of the samples and results. The P1 concentration [P1] was measured by EPR, which brings an error of around ±6 %. The fitting error for μ_{270} is $\lesssim$1 %.

Sample	[P1] (ppm)	μ_{270} (cm^{-1})
Cas-40	3.2	5.9
Cas-44	9.5	17.7
Cas-48	5.2	10.9
Cas-50	19.3	37.2
Cas-51	11.2	24.7
Cas-68	7.8	13.9

From this new protocol, one can estimate $[P1]$ directly from their UV-Vis spectra, without calibrating by other methods. This can be achieved for any samples with both sides polished in the following way: Firstly measure the UV-Vis transmission in percentage then convert it into the absorption spectrum in cm^{-1}; secondly separate the spectrum to extract the 270 nm band and obtain μ_{270} according to the method described above; finally calculate the P1 concentration using Equation (2.5) with the absorption cross-section σ or σ_e (depending on the logarithm type when deducing the absorption from transmission). The method is setup-independent and applicable for UV-Vis spectra taken by any machine, whether by volume measurements or spatially resolved measurements. No further EPR/FTIR measurements are required, as Equation (2.5) gives the absolute value of the P1 concentration and the given value for σ can be used.

The detectable range of the P1 concentration is determined by the UV-Vis spectrometer, here the author discusses estimated values based on our spectrometer with a photometric accuracy for the absorbance of 0.0006 (the absorbance is given by $-log_{10}(I_2/I_1)$, where I_1 and I_2 are respectively the light intensity before and after the absorbing material). The range can be improved with better spectrometers.

The fitting method in this section is highly sensitive - ideally when the 270 nm band can be distinguished and extracted from the background, it can be applied to calculate the P1 concentration using the method. As a reference, the lowest and highest P1 concentration that have been measured in-house already are respectively 0.1 ppm (320 μm thick) and 30 ppm (210 μm thick). Although the two samples were not calibrated with the EPR method (and for 0.1 ppm it is difficult to be measured with EPR), satisfactory fittings were carried out, confirming the feasibility of the method in this range. Here gives the derivation of the estimated detectable range as follows:

In order to extract the 270 nm band from the spectrum, the signal (the band height) should be larger than the measurement noise of the absorbance. The absorbance here represents the quantity of light that is absorbed by the sample, which is not normalized by the sample thickness. Its noise is denoted as S_A, then the criterion can be expressed as $\mu_{270} \cdot d > S_A$, where (as a reminder) μ_{270} is the extracted band height at 270 nm and d is the sample thickness.

From Equation (2.5) we have:

$$\mu_{270} \cdot d = \sigma \cdot [N_s^0] \cdot d \tag{2.6}$$

Therefore the criterion becomes:

$$\mu_{270} \cdot d = \sigma \cdot [N_s^0] \cdot d > S_A \tag{2.7}$$

$$\Rightarrow [N_s^0] \cdot d > S_A/\sigma \tag{2.8}$$

Equation. (2.8) gives the limit of the combination of the N_s^0 concentration $[N_s^0]$ and the sample thickness d, to measure thinner samples, higher $[N_s^0]$ is required to acquire a valid signal. This is influenced by the measurement devices, which exhibit different S_A. In the case of this thesis, a measurement noise of $S_A \approx 0.0006$ is given as the photometric accuracy from the manufacturer. This value was also confirmed

with the background measurement. This leads to:

$$[N_s^0] \cdot d > 3.1 \pm 0.2 \ \mu\text{m}^{-1} \cdot \text{ppm}^{-1} \tag{2.9}$$

With that, theoretically one can detect the P1 concentration above ∼0.01 ppm for a diamond thickness of 300 μm. Be aware that the values discussed here are based on the precision of our UV-Vis spectrometer. The analysis method, with improved devices, can potentially achieve a lower detection limit of the N_s^0 concentration.

The upper limit of the P1 concentration can be considered from the lowest reliable transmission (T) that can be measured. As the absorption is deduced from the transmission (the lower the transmission T the higher the absorption A), when the transmission is too low to be measured, no reliable absorption can be deduced. In the actual measurement, the lowest reliable T as 0.1% was observed for our device. From Fig 2.4 we can see that around 270 nm, most of the absorption was contributed by the 'ramp' rather than the 270 nm band. The upper detection limit of the absorption is partially influenced by the 'ramp' and partially by the 270 nm band, and these two contributions can vary in relative strength in the spectrum in the samples. In this sense, a complication arises when estimating the upper detection limit of the P1 concentration, as the fraction between the 'ramp' and the 270 nm band differs from sample to sample, and their behavior for higher N_s^0 range is unclear.

The author points out that for many HPHT diamonds with P1 concentrations ≥100 ppm (with a thickness of 250-300 μm), our spectrometer is unable to detect sufficient transmitted light at the wavelength of 200-400 nm, therefore no spectrum is acquired in this regime to apply the fitting. Polishing down the sample thickness or using a more sensitive spectrometer potentially allows the spectrum acquisition of samples with such high nitrogen densities, so that the new method can be applied. Based on the samples that have been measured, the author estimates the upper detection limit to be 30-50 ppm for typical 300 μm thick diamond plates. This is limited by the lowest reliable transmission T of 0.1%. For more sensitive setups, an order of magnitude lower T-limit (i.e. 0.01%) can potentially enable the detection of higher P1 concentrations by an order of magnitude, meaning up to hundreds of ppm for 300 μm thick samples. In general, for higher N_s^0 concentrations, the sample thickness, the fraction of the 'ramp', and the precision of the device should be considered carefully to acquire a sufficient UV-Vis spectrum.

2.2 Determining NV concentration

Multiple methods can be used to determine the NV concentration. Photoluminescence (PL) based methods are well applied, giving relative NV concentrations between different positions and samples, while the absolute values require calibrations. Different calibration methods have been used in previous work, for example comparing the NV-PL intensity with a single NV center [4, 94], or calibrating the NV-PL with the absorption cross-section [79]. The UV-Vis absorption spectrum at cryogenic temperature has also been used to determine NV^- and NV^0 concentrations respectively [59, 120]. Specifically, the ZPL of NV^- and NV^0 can be well identified in a cryogenic UV-Vis spectrum, thus they can be used to determine the concentration. EPR methods have been also applied in a few cases [121, 114], but usually only work for high NV concentrations.

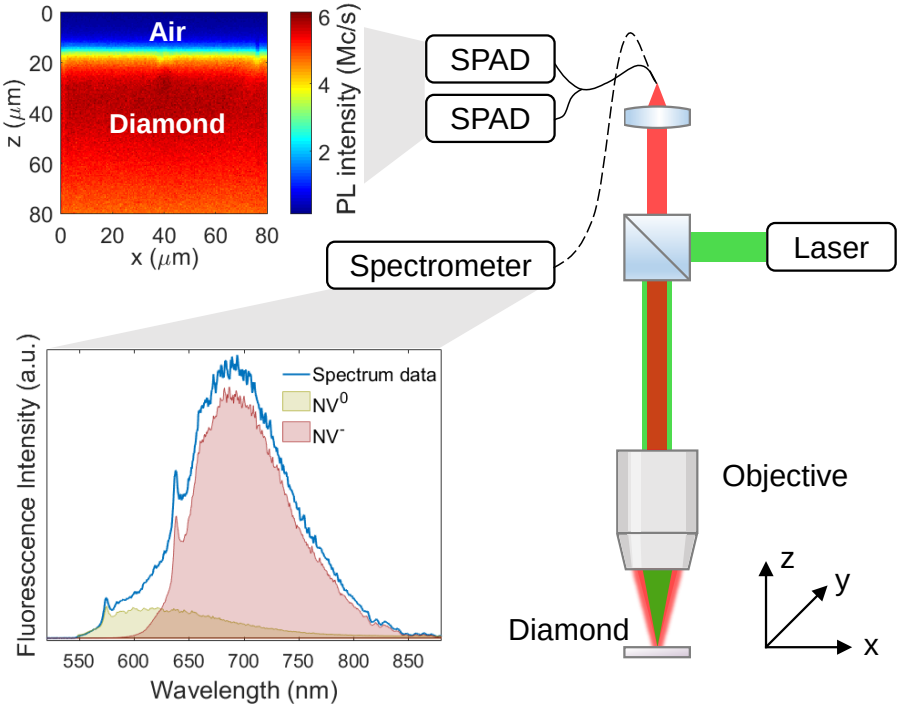

Figure 2.6: Schematic for the Photoluminescence (PL) measurement of NV-doped diamond plates. The diamond sample is excited by a 532 nm green laser, which is reflected by a dichroic mirror into the objective and then focused on/in the sample. Excited NV centers emit red fluorescence, which passes through the dichroic mirror and is focused by a lens into the fiber. The fiber is then connected to the detector (SPADs or the spectrometer).

One must be aware that comparisons between results obtained by different meth-

ods should be treated carefully. NV-PL-based methods are most commonly used, although the NV fluorescence can be suppressed in some cases (e.g. by very high nitrogen concentration [122] or graphitization [123]), it is still an excellent way to evaluate the NV concentration, as it links directly to the sensing applications, and in this sense it plays an even more important role than the 'absolute' number of NV spins. Therefore, this section will mainly discuss the NV concentration and NV charge states estimated by PL, and the calibration method.

In this thesis, the NV concentration is determined by NV-PL measured with a home-built confocal setup (Figure 2.6). NV-diamonds are excited with a 532 nm green laser (CrystaLaser), with a power of 10 μW, then the PL signal is detected by single-photon avalanche diodes (SPAD, Laser Components Count-T series) and a spectrometer (HORIBA iHR320). The setup can scan the sample in three dimensions (moved by a piezo stage, Physik Instrumente), maximum of 200 μm on each axis. Depth slice maps (XZ) and surface-parallel maps (XY) are constructed from the signal by SPAD, in order to calculate the average PL intensity for the relative NV concentration. Software Qudi [124] is used to control the scanning of the sample. The spectrometer then provides the spectrum at single positions to check that the fluorescence is produced by NV centers, and later on the spectrum is used to determine the NV charge state. The following subsections discuss details of the determination of the total NV concentration, the calibration with UV-Vis absorption cross-section, and the NV charge state analysis.

2.2.1 Determine total NV concentration by PL

As described above, depth maps and XY maps are taken for diamond samples to compare their fluorescence intensity, Figure 2.7. The average intensity is calculated, but normally not through the entire scanned depth, as the diamond absorption can largely influence the PL profile along the depth. That means, for highly absorptive diamonds, the deeper into the diamond, the more excitation green light and emission red light are absorbed by the material, thus less fluorescence can be detected. This explains the smooth decay of the PL signal along the Z-axis for some samples (left subplot in 2.7(b)). Theoretically, if the absorption is homogeneous in the diamond, one can build up a model that links the intensity decay and the absorption coefficient to correct the depth scan. However, considering the complex influence factors of the diamond absorption (Chapter 5), the absorption coefficient can be varied in different samples area (for some growth protocols significant changes were observed in the

absorption along the depth). To map the absorption changes spatially is also rather difficult. In this sense, the average intensity is taken over a near-surface region to remove any error that is caused by the diamond absorption. Normally the author takes the regime from the sample surface to 10-20 μm deep for the calculation (for hundreds of micron thick samples).

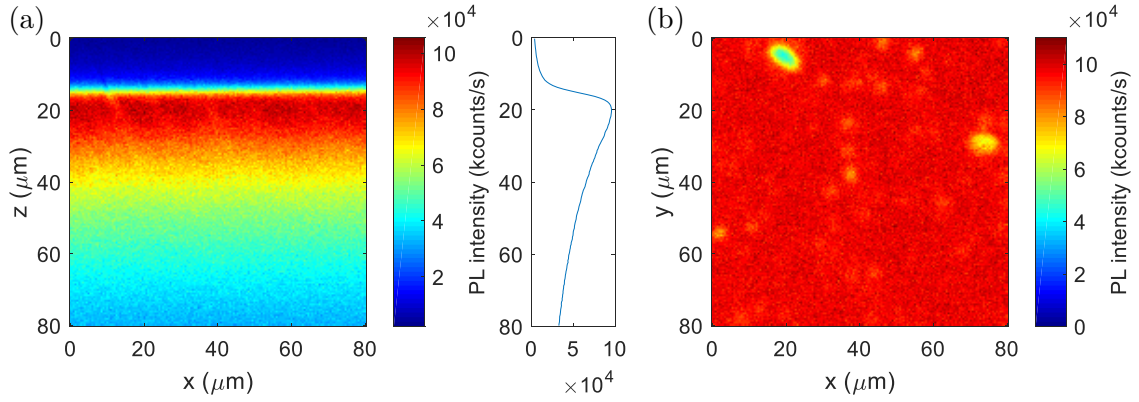

Figure 2.7: To determine the relative NV concentration, PL maps of the NV-diamond are taken (a) in depth (XZ scan), left subplot shows the line average of the PL intensity; (b) in XY plane.

For the depth scan, one must be aware that due to the high refractive index of the diamond (∼2.4), the distance that the stage has moved (also the value shown on the Z-axis in the map, denoted as z), is not equal to the actual depth in the diamond of the laser focus (denoted as z'), Figure 2.8. The depth z' is always larger than the distance z, with a constant factor given by the diamond refractive index n_d and the numerical aperture (NA $= n_a sin\theta_a$, where $n_a \approx 1$ is the refractive index in air) of the objective:

$$\frac{z'}{z} = \sqrt{\frac{n_d^2 - \mathrm{NA}^2}{1 - \mathrm{NA}^2}} \tag{2.10}$$

As an example, for the setup that uses an objective with NA=0.95, $z' \approx 2.21z$, meaning 1 μm in the depth map covers ∼2.21 μm depth in diamond in reality.

The Equation 2.10 is deduced using simple ray optics with the Snell' law $n_a sin\theta_a = n_d sin\theta_d$. For a small NA, from the Equation 2.10, the optics can be approximately stretched by the refractive index of the diamond, i.e. $z'/z \approx n_d \approx 2.4$. This approximation can be also deduced from matrix optics by assuming small angles relative to the propagation direction.

As the next step, the averaged PL intensity needs to be calibrated by other methods

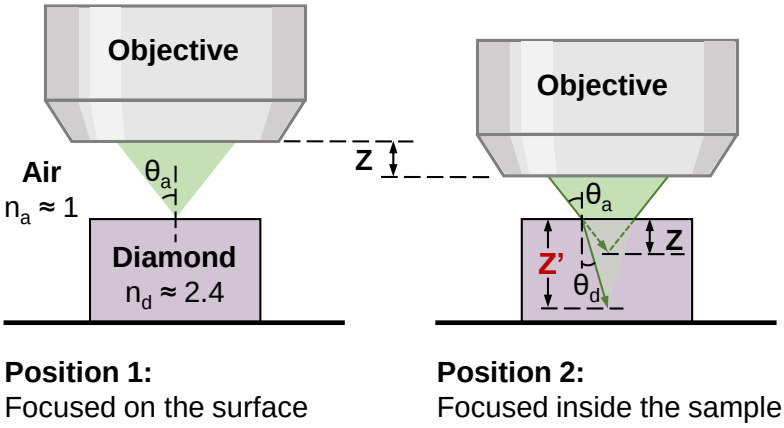

Figure 2.8: Different focus positions: the relation between stage moving distance z and actual focusing depth z' in the diamond.

to obtain the absolute value of the NV concentration. Here this thesis uses the UV-Vis absorption spectroscopy and the known literature value of the absorption cross-section of the NV center at 532 nm, σ_{532}, for the calibration. The NV absorption band covers a range around 450 nm to 700 nm with its ZPL at 637 nm. As shown in Figure 2.9, the NV absorption band is subtracted with its absorption 'base' (fitted from the two ends before and after the band using an exponential function) to obtain the absorption coefficient μ_{532}. The absorption coefficient is measured and deduced using the same method as described in Section 2.1. The NV concentration $[NV]$ can be given by the relation:

$$[NV] = \mu_{e\_532}/\sigma_{532} = c \cdot \mu_{532} \tag{2.11}$$

In [125] an absorption cross-section $\sigma_{532} = (0.95 \pm 0.25) \cdot 10^{-16}$ cm^2 has been given for the absorption coefficient in natural logarithm, μ_{e_532}. For an absorption coefficient in a common logarithm, μ_{532}, a coefficient c can be deduced from Equation 2.11 using the literature value of σ_{532} above to calculate the NV concentration. Moreover, with this σ_{532} value one can obtain $[NV]$ in cm^{-3}, the $[NV]$ in ppm still needs another conversion factor. The coefficient c in cm·ppm for the common logarithm based absorption can be converted from σ_{532} following this relation:

$$c = \frac{\ln(10)}{10^{-6}} \cdot \frac{m_C}{\rho_{dia}} \cdot \frac{1}{\sigma_{532}} \tag{2.12}$$

where ρ_{dia}=3.51 g/cm^3 is the diamond density, and m_C=1.99×10^{-23} g is the atomic mass for ^{12}C. From this we get $c = 0.14 \pm 0.04$ cm·ppm, this value can be directly

applied to Equation 2.11, which gives total NV concentrations in ppm.

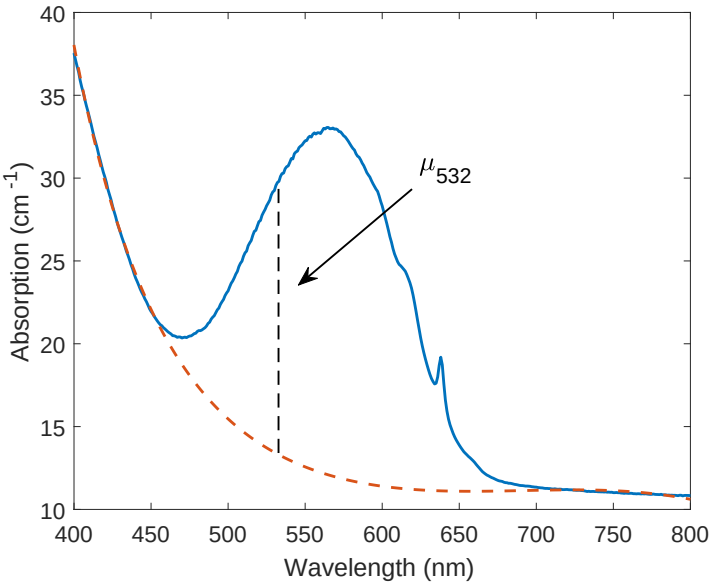

Figure 2.9: The absorption coefficient μ_{532} is given by subtracting the NV band with the absorption base.

From the UV-Vis spectrum, one can estimate the absolute value of the NV concentration, without calibrating by other methods. However, for low NV concentrations (below 50 ppb), the NV absorption band is very weak or undetectable at room temperature. On the contrary, an NV-PL signal can be detected for NV-ensembles with very low concentrations in bulk diamonds, even down to a single NV center. The PL measurement has high accuracy to compare NV emission between different samples, but the conversion to absolute concentration values carries ∼30% error, which is induced by the absorption cross-section's literature value error (i.e. the error of σ_{e_532}).

A series of CVD and HPHT diamonds were measured with both the PL and UV-Vis method, then compared the results of the two methods, Figure 2.10. The PL intensity of CVD samples is highly consistent with the UV-Vis result, showing an approximately linear correlation, while for HPHT samples the two methods show a larger discrepancy. A likely explanation is the inhomogeneity of the HPHT sample, as we take the UV-Vis spectrum with a collimated light beam (with a diameter of ∼2.5 mm), it averages the absorption of different sectors in the HPHT diamond. In comparison, the PL measurement is only taken in small sample regions. As the NV concentration in HPHT diamonds can be very different from sector to sector,

a large-scale PL measurement and a spatially resolved UV-Vis measurement will be more helpful. Furthermore, [122] has shown the variation of quantum efficiency in HPHT sectors with very high nitrogen density, which makes the two methods inconsistent and dependent on the nitrogen content of different samples.

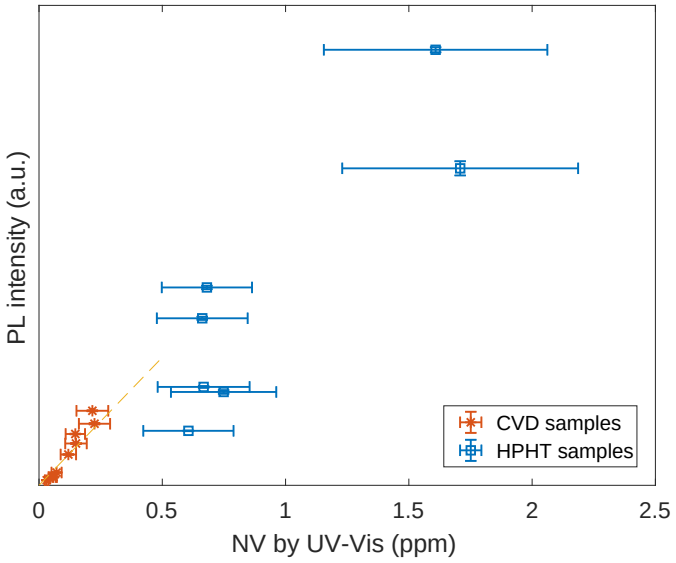

Figure 2.10: Calibration of NV-PL by UV-Vis method. For CVD diamonds with lower nitrogen concentrations, the PL intensity shows a linear correlation with the UV-Vis result, while for HPHT diamonds the result shows a large discrepancy.

In this regard, to calibrate a PL system to determine the absolute NV concentration, homogeneous CVD diamonds are much more reliable. The calibration is needed for each setup, and for different laser powers. In this thesis, 10 μW is used for all samples when determining the NV concentration by the PL method. With this laser power, a stable NV charge state distribution is suggested, which will be discussed in the next section.

2.2.2 NV charge state analysis

Apart from the total NV concentration, another key point is the NV charge state distribution, i.e. the NV^-/NV ratio. This thesis analyzes the NV^-/NV ratio based on the NV emission spectrum, which does not require harsh experimental conditions (e.g. cryogenic setups for cryo-UV-Vis measurements, complex sample preparation steps for EPR measurements, etc.). The NV emission spectrum is easily taken at

room temperature using the setup described in Figure 2.6. The laser power of 10 μW is chosen for a stable charge state distribution. At this level of the excitation power, the NV diamond shows its intrinsic NV-charge-state distribution, higher powers lead to stronger photo-ionization, which transfers more NV^- into NV^0. For instance, raising the laser power from 10 μW to 100 μW can result in a $\sim$10% drop in the NV^-/NV ratio [123]. Since there is still the question of whether the photo-ionization is influenced by the nitrogen and NV densities, it is important to avoid the changes that are introduced by the laser power when comparing different diamond materials, but only to compare their intrinsic properties.

The acquired NV emission spectrum is separated into the NV^- and NV^0 components respectively to analyze their ratio, Figure 2.11. The feature of each charge state component is given by a reference spectrum. The NV^- reference was measured from a sample that exhibits only NV^- at low laser power (an irradiated HPHT Ib diamond), while the NV^0 reference was taken by exciting the NV center with a blue laser (405 nm), where only NV^0 centers are excited. The reference spectrum should be always taken by the spectrometer that acquires the to-be-analyzed spectrum, since different spectrometers with varying spatial resolutions can influence the 'shape' of the spectrum, using a mismatched reference spectrum will deteriorate the fitting performance.

A weighted sum of the two references is fitted to the acquired spectrum, determining the weighting factors that fit best by a least-squares method. By doing this least-squares fitting we obtain the photon number ratio (N_p^-/N_p^0) of the two charge states. Since the two NV charge states have different life times, the photon number ratio needs to be further corrected with the decays rates $\Gamma^- = 1/12$ ns^{-1} and $\Gamma^0 = 1/20$ ns^{-1}, respectively for the two charge states [73, 126], with the relation: $[NV^-]/[NV^0] = (N_p^-/N_p^0) \cdot (\Gamma^-/\Gamma^0)$. The ratio $[NV^-]/[NV^0]$ is the concentration ratio of the two charge states, it can be applied to the total NV concentration (Section 2.2.1) to calculate the concentration of each NV charge state.

Another fitting method, non-negative matrix factorization (NMF), is also used in the community to separate the NV spectrum. A large number of similar spectra (where it is required that many different charge state ratios occur) are required to train the algorithm to recognize the two components. The algorithm itself can 'build up' the feature for the NV^- and NV^0 component, no actual reference spectrum of them is needed. In other words, one can say that the NMF method helps to create an artificial reference for the two charge states. If enough suitable feeding spectra

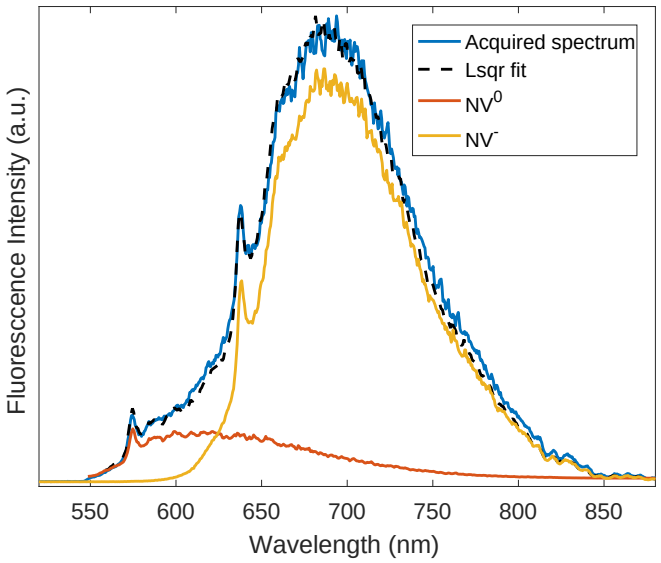

Figure 2.11: Calibration of NV-PL by UV-Vis method. For CVD diamonds with lower nitrogen concentrations, the PL intensity shows a linear correlation with the UV-Vis result, while for HPHT diamonds the result shows a large discrepancy.

are applied to train the algorithm, it has the chance to create artificial references that are very close to the real NV^- and NV^0 spectrum. However, it needs to be pointed out that the method can sometimes create NV^0 components containing parts that should come from NV^- (for instance a part of the NV^- ZPL). This will definitely influence the analysis of the NV^-/NV ratio. In this regard, one should be careful when using this method, and add enough good feeding spectra to improve the algorithm. The least-square fitting with two reference spectra does not require scores of feeding spectra, as long as the reference spectra are acquired properly, the fitting result turns out to be satisfactory. Therefore in this thesis, the least-square fitting is used to determine the NV charge state.

2.3 Determining other related defects in diamond

Apart from the P1 center, other nitrogen-related defects also play roles in the NV research: the total nitrogen concentration $[N]$, for instance, is an important candidate. The total nitrogen concentration indicates the nitrogen incorporation efficiency during the growth. The ratio of P1 centers to total nitrogen atoms also correlates to the NV creation efficiency, as nitrogen atoms in other forms can influence the NV

formation. Furthermore, as $[N]$ influences the NV decoherence significantly [13], investigating and improving its conversion rate has big advantages. The established standard to determine $[N]$ is secondary ion mass spectroscopy (SIMS). This method has the disadvantage of damaging the diamond surface, which limits its application scenarios. Optical-spin measurements, instead, can also estimate $[N]$ without damaging the sample. Double electron-electron resonance (DEER) is the up-to-date protocol to achieve a good estimation of the nitrogen concentration [127], however this is only a very local measurement.

As shown in Section 2.1, FTIR and UV-Vis spectroscopy are powerful tools to determine defect concentrations in diamonds. Apart from the N_s^+ center (1332 cm^{-1}) that has been discussed (Figure 2.2), nitrogen aggregations can be also determined by the FTIR. For instance, the A center, which is the neutral nitrogen pair, has a main peak at 1282 cm^{-1}. The B center, which consists of a carbon vacancy surrounded by four substitutional nitrogen atoms, has a more complex feature including the main peak at 1175 cm^{-1}, a sharp line at 1332 cm^{-1} (which actually superposes the NV_s^+ peak), minor features at 1,100, 1,010 cm^{-1} and a characteristic plateau from 1,290 to 1,210 cm^{-1} [107]. The determination of the A- and B-center densities varies slightly for different types of diamonds, which [107] has discussed in detail.

Other nitrogen-related centers, like the NVH^- center, can be identified in the FTIR spectrum at 3123 cm^{-1} [113], while its concentration is normally determined by EPR. The H2 (NVN^-) and H3 (NVN^0) centers can be identified in both the diamond PL and UV-Vis spectrum, with a ZPL at respectively 986 nm and 503 nm. Specifically, the concentration of H3 centers in ppm can be determined using the relation[128, 129, 107]:

$$[H3] = 0.5\mu_{485} \tag{2.13}$$

where μ_{485} is the absorption (in cm^{-1}) of the H3 center at 485 nm measured at room temperature. According to the reference, when using this formula, the background absorption underlying the H3 center absorption must be subtracted correctly.

The UV-Vis and FTIR methods above are used to determine the existence of the mentioned nitrogen-related defects for the diamond samples in this thesis. The absolute concentration of these defects is not discussed, but the qualitative research of their features helps to improve the growth and treatment procedures.

Chapter 3

3 P1 incorporation and NV creation during CVD growth

Magnetometry with NV-ensembles exhibits a considerably improved signal-to-noise ratio and sensitivity compared to single NV centers, which both ideally improve with the square root of the number of sensing spins [12, 13]. NV centers are formed from single substitutional nitrogen (P1 centers, Chapter 2), thus a high NV^- concentration requires enhanced incorporation of P1 centers in diamonds. Nevertheless, the nitrogen impurities are also the main decoherence source of the NV spin, which limits the coherence time T_2 [91, 92, 93] for quantum sensing. These competing parameters create challenges for improved sensitivity in magnetic field sensing [40, 94], which requires both high NV^- concentrations and long coherence times.

This chapter studies the P1 incorporation, NV creation, NV charge state distribution and the coherence time, T_2, after CVD growth. The material consideration for high sensitivity is discussed. Based on that, two diamond series span a broad range of nitrogen content (varying nitrogen flow rates over 4 orders of magnitude) are investigated to understand the correlation between the P1 and NV concentration, and T_2 after growth. The properties and limits of the as-grown NV-doped CVD diamond are discussed, as well as the challenge raised by higher nitrogen-doping levels. The study in this chapter plays an important role as the first step to obtain optimized diamond material for sensing applications. The results of this chapter and Chapter 4 lead to the publication [116] of the author.

3.1 Material consideration for sensitivity

State-of-the-art magnetometers with NV-ensembles exhibit sensitivities at the $\mathrm{pT}/\sqrt{\mathrm{Hz}}$ level [102]. While competing technologies, for instance superconducting quantum interference devices (SQUIDs), can achieve sensitivities at the $\mathrm{fT}/\sqrt{\mathrm{Hz}}$ level and below [13, 63], they are often realized as bulkier devices. These technologies can also require specific temperature conditions, for example vapor cell magnetometers (which are also known as the optically pumped magnetometers, OPM) is operated at high temperatures. NV-diamond sensors can be used at room temperature and can be integrated as compact, portable devices, this enables more potential applications that are hardly realized by other technologies [51, 65, 66, 67, 68, 69]. The key challenge for NV-based magnetometry is therefore to improve sensitivity. On one hand, developing novel NV-magnetometers for improved sensitivity has been intensively studied [57, 130, 131, 75]. On the other hand, the NV-diamond itself also limits the sensitivity. Optimizing NV-diamonds plays an important role and lays a foundation for high-sensitivity magnetometry applications from the material side.

The sensitivity of the magnetometer represents its precision in a way that is independent of the measurement time, in other words it is normalized by the bandwidth and it gives the error, therefore the sensitivity should be as small as possible. For NV-ensemble-based magnetometry, the shot-noise limited sensitivity η is determined by the coherence time and the NV density [40, 94, 75], which can be simplified as a general form:

$$\eta \propto \frac{1}{C\sqrt{I \cdot \tau}} \tag{3.1}$$

where C is the measurement contrast, I is the PL intensity of NV centers, which is magnified by the NV concentration (physical definitions see Section 1.2). The coherence time τ can be set to either T_2 or T_2^* for AC or DC magnetometry respectively (Section 1.2). The relation shows that a large $C\sqrt{I \cdot \tau}$ leads to better sensitivity, thus both a high NV fluorescence and a long coherence time are preferred. One must be aware, the contrast C is significantly influenced by the NV charge state ratio [59]: NV^0 centers contribute as a fluorescence background deteriorate the contrast. Therefore, a stable NV charge state distribution and a higher NV^- fraction also need to be taken into account.

To briefly sum up, the NV-diamond should be optimized for a high NV^- concentration, a high $\mathrm{NV}^-/\mathrm{NV}$ ratio, and a long coherence time. However, the three key requirements influence and are limited by each other. The coherence time $\mathrm{T_2}$ is set

by fluctuating magnetic dipoles surrounding and coupling to the NV centers. It has been suggested [132, 102] that for nitrogen concentration above ∼0.5 ppm, nitrogen electrons are the major source of decoherence. For lower concentrations typically the nuclear spins of ^{13}C are the dominating magnetic dipole noise limiting the coherence time, the diamond strain can also play a role [133]. Bauch *et al.* [102] have suggested a model linking nitrogen concentration and coherence time as:

$$\frac{1}{T_2([N])} = B_{NV-N} \cdot [N] + \frac{1}{T_{2,other}} \tag{3.2}$$

where $B_{NV-N} = 2\pi \times (1.0 \pm 0.1)$ kHz/ppm is the nitrogen-dominated NV decoherence rate, $[N]$ is the nitrogen concentration (determined by the secondary ion mass spectroscopy (SIMS) in their work), and $T_{2,other} = 694 \pm 82$ μs comes from the decoherence factor independent of nitrogen. The model should be generally applied for diamonds with spin concentrations [N] $\gg$ [NV], where NV-NV dipolar interactions are negligible. In this chapter, the discussion about coherence time is in the same case where [N] $\gg$ [NV] is fulfilled.

As the P1 center is the starting point to form the NV center, a high NV^- concentration comes from a high total nitrogen doping level, which deteriorates the coherence time. Moreover, while converting P1 centers to create NV^- centers, non-negligible NV^0 centers are often formed, this also reduces the ODMR contrast. Contrary demands for high NV fluorescence, long coherence times and high NV^- fractions call for a balance between them. This also brings the main challenge while optimizing diamond material for improved sensitivity. For this purpose, the nitrogen-doped CVD growth performs competitive as it is highly controllable to obtain prospective combinations of these three factors.

Discussions in previous works about material-limited sensitivity were mostly focused on the 'seesaw' of the nitrogen density and coherence time: one always needs to consider the trade-off between the long coherence time and the high nitrogen density. For instance, Edmonds *et al.* [59] have discussed the merit of [P1]×T_2^*, which keeps on increasing until P1>10 ppm for neutral abundance 1.1%^{13}C diamonds and P1>0.1 ppm for depleted 0.005%^{13}C diamonds, after that the merit stays consistent. They have suggested that P1 concentration ranges in 10-15 ppm are most interesting, since higher P1 concentrations will not further enhance [P1]×T_2^* (thus improve the sensitivity), and to keep relatively low P1 concentration and long T_2^* may provide advantages such as improved measurement duty cycle. Additionally, for lower P1 concentrations, achieving a decent long T_2^* in practice requires better

control of other dephasing sources.

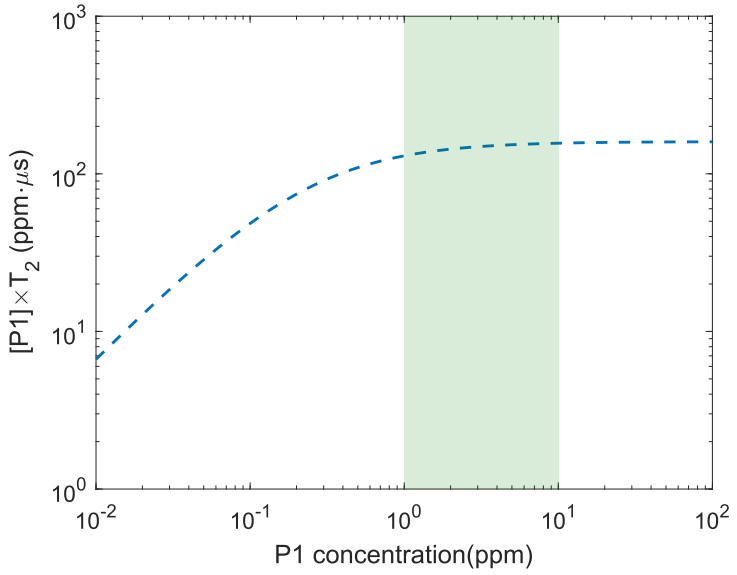

Figure 3.1: When assuming [P1] is proportional to [N], [P1]×T_2 as a function of P1 concentration can be determined according to Bauch's model [102]. The value of [P1]×T_2 saturates for [P1]$\gtrsim$1 ppm, which makes the regime 1-10 ppm most interesting.

For the coherence time T_2, a similar approach can also help to determine the material limits. Figure 3.1 shows [P1]×T_2 as a function of the P1 concentration according to the model in Equation 3.2. The value of [P1]×T_2 increases with [P1], then saturates for [P1]$\gtrsim$1 ppm and reaches a plateau. The desired P1 concentration ranges from 1-10 ppm for the same reason discussed above. Here their relation is plotted by assuming that the P1 concentration is proportional to the total nitrogen concentration, in practical cases it is more complicated, which will be discussed in Section 3.3.

Studying the trend of [P1]×T_2 is the very first step to analyze the material-limited sensitivity. As-grown diamonds are the proper material to look into the relation between [P1] and T_2, as most of the P1 centers are not converted into NV centers at this stage. With knowing the interesting regime of the P1 concentration, the next step is to consider that P1 centers can be only partially converted into NV centers, and the value of [NV^-]×T_2 influences the sensitivity directly (Equation 3.1). Therefore, two key points are crucial for further analysis of the sensitivity: firstly, the mechanism of the P1 center conversion and NV center creation; secondly, how T_2 changes when converting more P1 centers into NV centers. This and the next

chapters discuss these key points based on the actual experimental results and show general rules of the interrelation between the P1 concentration, NV concentration, NV charge states, and T_2. Specifically, this chapter studies the as-grown diamond as a starting material (which is also interested in some applications for its advantages, see discussions in the next section), and the next chapter investigates the treated (e-beam irradiated and annealed) diamond to show the optimization approach. The results give further indications of the material limits for improved sensitivity.

3.2 P1 and NV creation with varying nitrogen in growth

Directly after CVD growth, NV-fluorescence is usually detectable in the nitrogen-doped diamond. Some NV centers are formed directly during the growth, additionally, a growth temperature >400°C can mobilize local vacancies to combine with P1 centers and form NV centers (and the temperature is normally lower than the point where NV centers start to dissociate significantly). Working with in-situ formed NV centers (which means NV centers formed during the growth) is appealing for its technological simplicity as it does not require any irradiation or annealing steps. Moreover, for applications that require particularly long coherence times but with less demand for high NV concentrations, the as-grown NV-diamond can be favoured [24], since the irradiation step promotes the formation of other defects (and more NV centers), which brings new decoherence sources. In this sense, understanding the in-situ NV creation and P1 incorporation plays an important role. To this end, two 'Nitrogen series' have been grown to map concentrations of P1 centers and NV centers created by different nitrogen flows, showing how NV centers correlate to P1 centers; and how NV charge states behave in this phase.

The two nitrogen series were grown with a varying N/C ratio altered by the N_2 to CH_4 flow ratio into the CVD reaction chamber (Figure. 3.2). In the chamber, these gases make up the plasma for the reaction. For the two series, the CH_4 flow was constant while the N_2 flow was changed to realize the variation of the N/C ratio. Nitrogen series #1 was grown on 4×4 mm HPHT type IIa substrates (New Diamond Technology). The substrates have been pre-characterized for the EPR measurement, which showed an undetectable P1 concentration. Other optical characterizations on this series were not influenced by the substrate, as localized experiments were

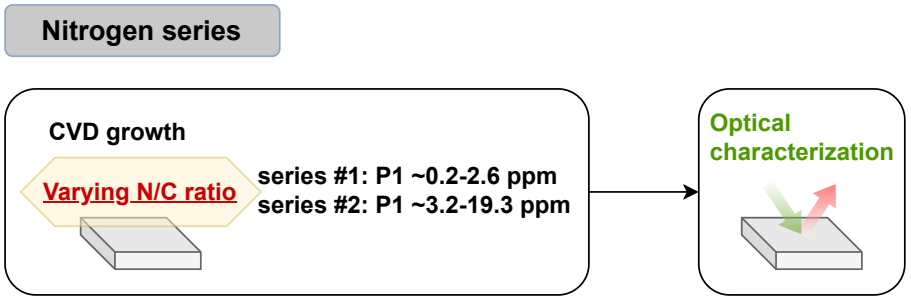

Figure 3.2: Characterization of in-situ NV creation in the Nitrogen series. The series was grown with a varying N/C ratio, resulting in P1 concentrations ranging from 0.2-20 ppm: 0.2-2.6 ppm for series #1 and 2.6-20 ppm for series #2.

conducted (which did not through the thickness of the whole sample that includes the substrate). Nitrogen series #2 was grown on 3×3 mm CVD substrates (Element Six, general grade SC plate CVD). They were laser-cut from the substrate after growth, i.e. no substrate contributes to the characterization for these series. To ensure comparability of the series grown on different substrate types, test growth runs were conducted on each type of substrate with the same growth conditions, followed by optical characterizations. The in-situ NV and P1 creations showed consistency between the two substrate types. For more details on the growth and sample preparation see Appendix A.

P1 concentrations of the two series were given from X-band continuous wave EPR spectra collected at room temperature. Nitrogen series #1 was measured by the spectrometer Bruker ELEXSYS E500 with a microwave frequency of 9.45 GHz (by Brett C. Johnson, RMIT), and Nitrogen series #2 was measured by Bruker ELEXSYS E580 with 9.84 GHz (by Rémi Blinder, Uni Ulm). Both spectrometers were fitted with a Bruker super-high-Q probe head (ER4122 SHQE). Two different EPR facilities were used simply due to accessibility issues at the time. The precision and comparability of the results are ensured by independent calibration in each facility. The same analysis (background subtraction and double integration) was employed. For the Nitrogen series #1, before each measurement, an HPHT diamond (secondary calibration) sample with a known spin number was measured to quantify the spin number in each sample. For the Nitrogen series #2, determination of the spin concentrations was performed using the built-in spin-counting feature, from the acquisition software (xEPR). For some sample orientations, it was found that the cavity could not be properly critically coupled. This effect can be due to the fact

that sample edges, made of graphite-like carbon, are conducting. Proper sample orientation was chosen to enable critical coupling. This consists in putting two opposite edges of the square samples parallel to the sample insertion axis. For that cavity, such orientation ensures that no current loop will be created, because of the perpendicularity of the electric microwave field (TE102 mode) to two of the sample edges. The EPR measurement for P1 concentration carries a ∼6% error.

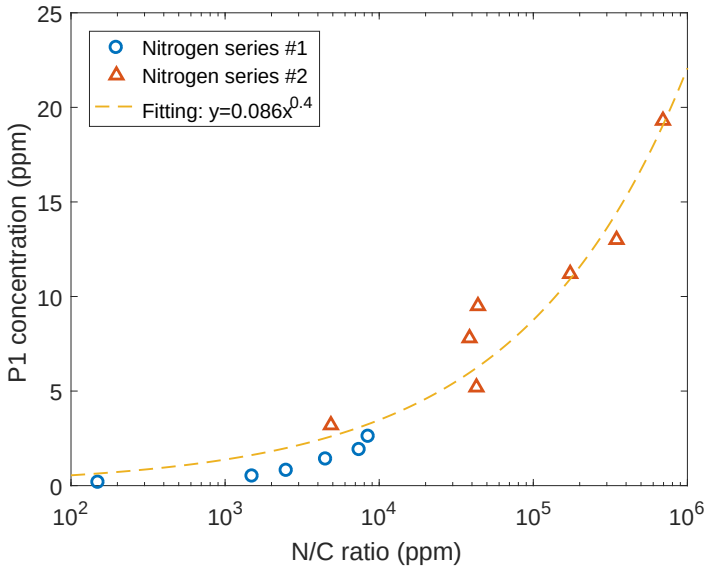

Figure 3.3: The as-grown P1 concentration is positively but sub-linearly correlated to the N/C ratio. The P1 concentration measured by EPR carries a relative error of ∼6% (not implemented in the plot).

The N/C ratio in the two series varied from 150 to 10^6 ppm during growth, resulting in an incorporated P1 concentration from 0.2 to 20 ppm (Figure 3.3). The result shows that the P1 concentration is positively correlated to the N/C ratio, with roughly P1$\sim 0.09\sqrt{\mathrm{N/C}}$, showing a clearly sublinear scaling (be aware that the N/C ratio in Figure 3.3 was plotted in logarithmic scale). This means the incorporation of P1 centers into the diamond lattice gets worse with higher nitrogen densities in the reacting space. Additionally, with higher N/C ratios (for Nitrogen series #2), the P1 incorporation shows larger scattering around the fitting. This also indicates that to create CVD diamonds with higher P1 concentration, the quality stability is more challenging and optimization of parameters for specific regimes can be required.

As shown in Figure 3.4a, the as-grown NV^- concentration is proportional to the P1 concentration, although a potential sub-linear or 'saturation' at higher P1 concentration is suggested by the last data point. For both nitrogen series, an average

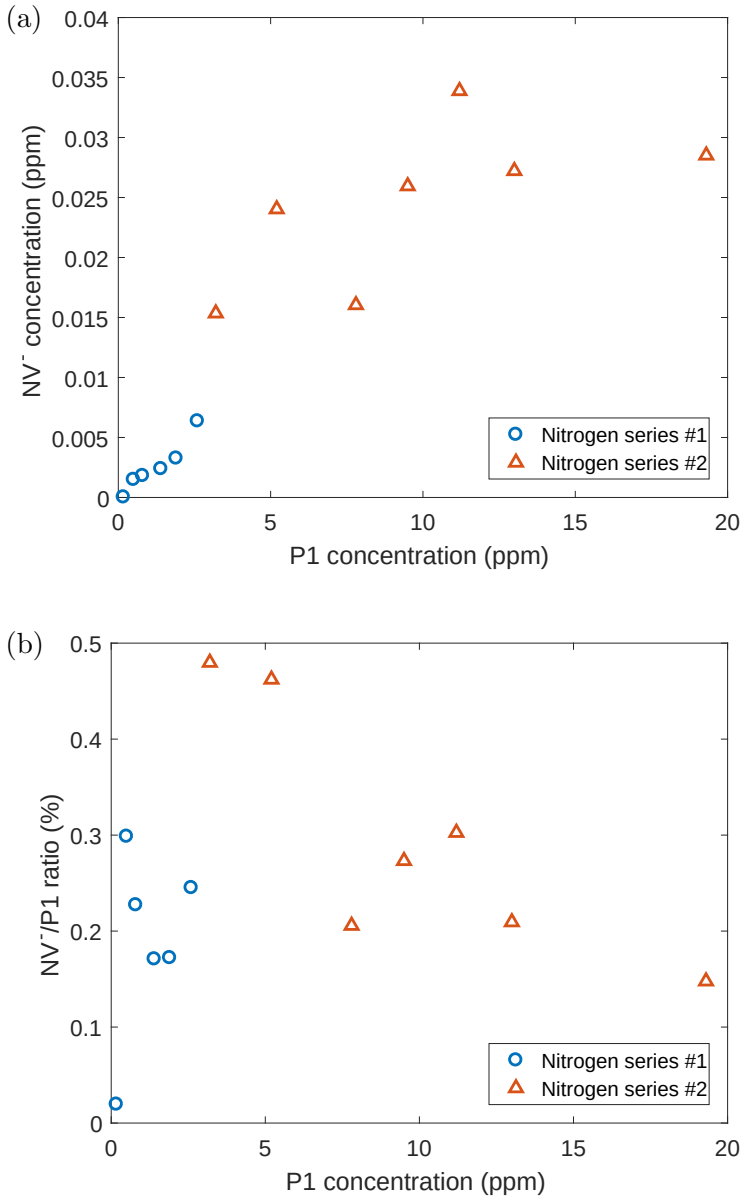

Figure 3.4: The as-grown NV^- concentration is proportional to the P1 concentration, with an average NV^-/P1 ratio of roughly 0.25%.

NV^-/P1 ratio of ∼0.25% (in the range of 0.18-0.3%) has been observed for different P1 concentrations (Figure 3.4b), with a larger variation around the fitting in Nitrogen series #2. A potentially decreasing NV^-/P1 ratio at higher P1 concentration is suggested by Nitrogen series #2, nevertheless, the scattered data makes it difficult to conclude a linearly decreasing trend. The NV^-/P1 ratio of the two series is in the same order as previously reported values (∼0.1% by Deák *et al.* [134] and ∼0.5% by Edmonds *et al.* [59]). The highest in-situ created NV^- concentration is around

33.9 ppb, which is much higher than normal as-grown HPHT diamonds, in which NV centers are largely dissociated under their growth conditions. However, one must be aware that the precondition for a consistent NV/P1 ratio is the same 'growth recipe' except for the nitrogen flow. Changing other growth parameters/conditions will also influence the NV/P1 ratio. This will be discussed in more detail in Section 3.4.

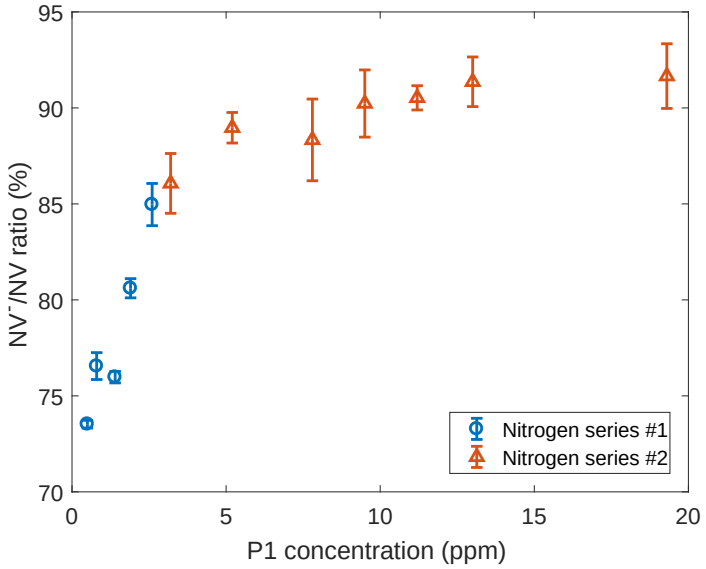

Figure 3.5: In the as-grown nitrogen-doped samples, the NV^-/NV ratio increases slightly with the P1 concentration.

After growth, the NV^- dominates with a NV^-/NV ratio above 70% for most of the samples (Figure 3.5). The low NV/P1 ratio shows that more P1 centers than vacancies were formed and NV creation in growth is vacancy-limited. A large number of P1 centers provide electrons to charge the NV^- center, which is consistent with the domination of NV^- and makes the charge state mostly independent of the P1 center density: with the P1 concentration varying over two orders of magnitude, the NV^-/NV ratio has only slight changes. Nevertheless, the NV^-/NV ratio still shows a clear increasing trend with increasing P1 concentration, indicating that the mean distance between P1 and NV centers is also relevant for the NV charge state distribution, not only for the NV/P1 ratio. This is surprising, as it is normally thought that the NV charge state is only determined by the NV/P1 ratio and thus the electron availability, but the result in Figure 3.5 shows that it is not the case and the mean distance should be the correct explanation. Details of P1 and NV creations see Table 3.1.

Table 3.1: P1 incorporation and NV creation in as-grown nitrogen series.

Series	Sample	N/C (ppm)	As-grown P1 (ppm)	As-grown NV^- (ppb)	As-grown NV^-/NV (%)
Nitrogen series #1	NDT-26	150	0.2	0.03	-
	NDT-14	500	-	0.2	-
	NDT-07	1500	0.5	1.5	73.5 ± 0.2
	NDT-34	2500	0.8	1.8	76.6 ± 0.7
	NDT-01	4500	1.4	2.4	76.0 ± 0.3
	NDT-02	7429	1.9	3.3	80.6 ± 0.5
	NDT-12	8500	2.6	6.4	85.0 ± 1.1
Nitrogen series #2	Cas-40	9722	3.2	15.3	86.1 ± 1.6
	Cas-48	42777	5.2	21.3	89.0 ± 1.8
	Cas-68	77142	7.8	16.0	88.3 ± 2.1
	Cas-44	87499	9.5	25.9	90.2 ± 0.8
	Cas-51	173571	11.2	33.9	90.5 ± 0.6
	Cas-49	347143	13.0	27.1	91.4 ± 1.3
	Cas-50	694286	19.3	28.5	91.7 ± 1.7

3.3 Coherence time of as-grown NV-doped diamonds

As discussed in Section 3.1, a high NV fluorescence and a long coherence time are preferred for improved sensitivity. The coherence time, however, is immensely suppressed by the nitrogen concentration in the diamond. This section studies the T_2 behavior of the nitrogen series, and how they change by the irradiation and annealing treatments.

The coherence time T_2 in this thesis was measured using the Hahn-echo protocol [135], Figure 3.6. On top, the figure shows the laser and microwave sequences, at the bottom is the Bloch sphere indicates the spin orientations at specific points of the sequence. At the position ① the laser initializes the spin to the $|0\rangle$ state, the first $\pi/2$ microwave pulse then rotates the spin to +y direction on the Bloch sphere, position ②. The spins are left to freely precess for a time τ_p (position ③), then rotated by a π pulse to the -y direction (position ④). Then, in the second free precession time τ_p, any phases that the spins might have accumulated with respect to the rotating frame will be unwound (position ⑤) [136]. In the end, a final $\pi/2$ pulse rotates the spins to the direction of $|0\rangle$ for the read-out and initialization by the laser for the next round. In the experiment, the free precession time τ_p is increased until any phase relation is randomized and the spin signal saturates, indicating a

completely mixed state. The decay envelope of the signal for the increasing τ_p then gives the coherence time T_2.

The measurement in this thesis was conducted with a home-built widefield microscope (by Di Wang and David Simpson, Uni Melbourne). A modulated 532 nm excitation laser (Laser Quantum opus) was focused onto the samples at a power of 100 mW with a spot size of 0.25 mm, then the NV-PL from a small central region of (16×16 μm) was collected by an sCMOS camera (ANDOR ZYLA 5.5 sCMOS). The Hahn-echo protocol was conducted with MW π time of 120 ns and readout laser time of 8.5 μs and repeated for 20 ms. The initial laser polarization time was 50 ms and the background magnetic field was 700 G. The microwave was delivered via an omega-shaped gold resonator with an inner diameter of 0.3 cm. The collected PL count from the dark state projection Hahn-echo sequence $(\pi/2)$-(τ_p)-(π)-(τ_p)-$(\pi/2)$ was referenced [24] against an immediate secondary spin-echo measurement with an addition π-pulse to the bright state projection, i.e. pulse sequence $(\pi/2)$-(τ_p)-(π)-(τ_p)-$(3\pi/2)$. The T_2 time is extrapolated from the exponential function $f(t) = a \cdot exp(-t/T_2) + c$, and the error of T_2 is given by the fitting error (95% confidence interval).

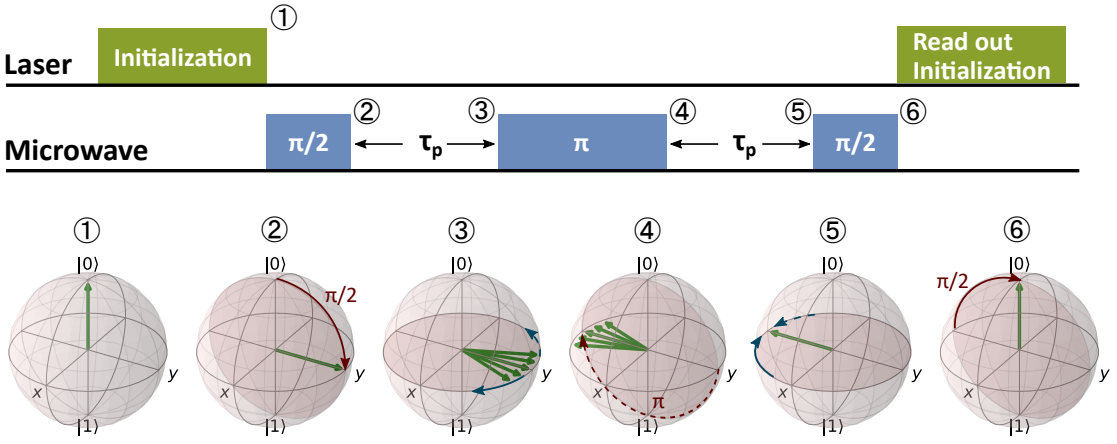

Figure 3.6: Hahn-echo sequence and its Bloch sphere depiction for T_2 measurement. The explanation is in the text.

After growth, the Nitrogen series #1 showed significant NV fluorescence, which correlated positively to the P1 concentration (Section 3.2). Its Hahn-echo coherence time T_2 is shorter for higher P1 concentration (blue circles in Figure 3.7a), which agree well with Bauch's model [102] (Section 3.1). The series shows 498 μs for 0.2 ppm P1, while only 53 μs for 2.6 ppm P1 (details see table 3.2).

Bauch *et al.* determined the total nitrogen concentration in the crystal by the

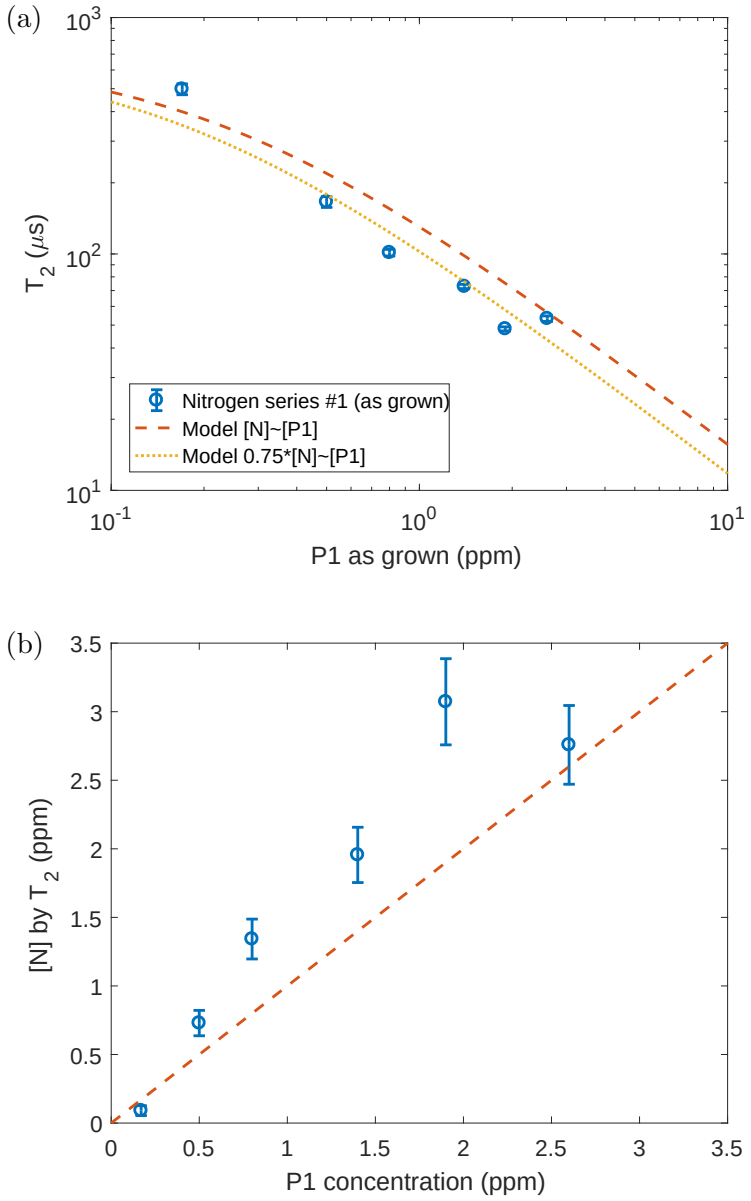

Figure 3.7: The coherence time T_2 of the Nitrogen series #1 measured by Hahn-echo (a) is limited by the nitrogen concentration, well agree with Bauch's model discussed in Section 3.1. (b) The nitrogen concentration calculated from T_2 is in scale with the P1 concentration measured by EPR.

secondary ion mass spectroscopy (SIMS), while the results here discuss the P1 centers measured by EPR (Section 2.1). SIMS is normally not sensitive enough for detecting ^{14}N with low concentrations, for which measuring the total nitrogen concentration of Nitrogen series #1 has technical difficulties. As P1 centers should be the main nitrogen-related defects in this series, the study on P1-T_2 relation still shows a high

consistency with the model. The two curves in Figure 3.7a show the model predicting the coherence times for P1 concentrations constituting 100% of [N] (red dashes) and 75% of it (orange dotted). Other nitrogen-related defects were not detectable in this series, however, since for a higher nitrogen-doping level (Nitrogen series #2) NVH^- centers were observed, a [P1]/[N]<100% is expected as well for Nitrogen series #1 (but other defects were just under the detection limit). For the curve 0.75∗[N]∼[P1] (75% [N] being P1 centers), the coherence time T_2 of the nitrogen series showed high consistency with the model, indicating that 75% can be the estimated [P1]/[N] ratio for this series. Figure 3.7b illustrates the correlation between measured [P1] and [N] calculated from T_2 according to equation 3.2, also showing that other nitrogen-related defects exist in the series, but with minor influences.

For Nitrogen series #2, the P1 concentration varying from 3.2 to 20 ppm crosses almost an order of magnitude, which induces larger variations in diamond properties. Considerable NVH^- centers and other undefined spins were observed in the EPR result (Table 3.2), and P1 centers are no longer dominant for such high nitrogen-doping levels. The results in the table show that the [P1]/[N] ratio is varying for different nitrogen-doping levels: for higher nitrogen-doping levels, other nitrogen-related defects (for instance NVH^-) show larger potential to form, thus the [P1]/[N] ratio decreases. While for Nitrogen series #1 most of the samples fit well with the model [P1]/[N]≈75%, the sample NDT-26 in this series (the one with the lowest P1 concentration) shows a longer coherence time than the model suggests. If it is true that the [P1]/[N] ratio decreases with the increasing nitrogen concentration, the long coherence time of NDT-26 can be explained, as its nitrogen concentration is very low that [P1]/[N]>75% is expected. Moreover, as its P1 concentration (0.17 ppm) is near the border where nitrogen starts to act as the main decoherence source, other properties of this sample play a role for its long coherence time (see more discussion of the model in Section 3.1).

In this context, for Nitrogen series #2, P1 centers are not the dominant defect anymore and the P1-T_2 relation is no longer in agreement with the model by Bauch *et al.*, Figure 3.8(a). Most of the T_2 in this series are lower than the model suggests, and show a large scattering without a clear decreasing trend. The existence of other nitrogen-related defects in this series, as discussed above, invalidates the assumption that 100% or 75% of nitrogen atoms in the samples are in the form of P1 centers. NVH^- concentrations in this series increase with the P1 concentrations, they can be even as much as P1 centers (Table 3.2). Taking them into account, the model then can be corrected by assuming that P1 and NVH^- centers are the main

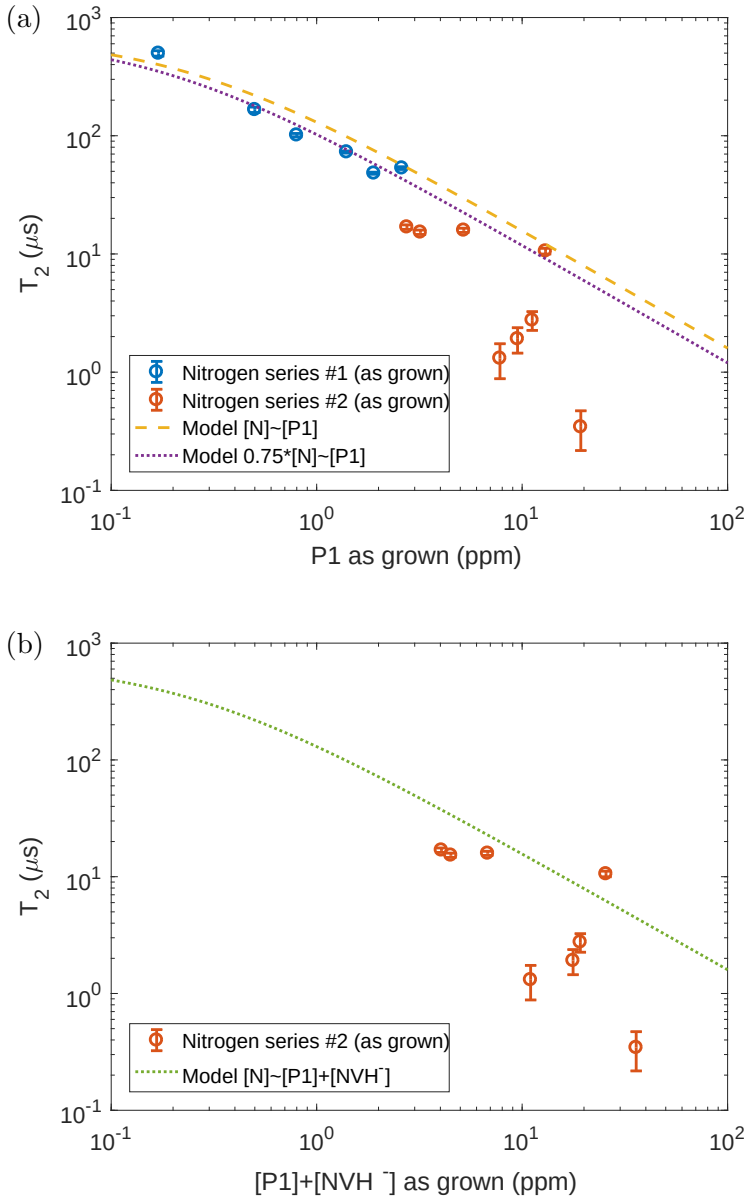

Figure 3.8: For higher nitrogen-doping levels (Nitrogen series #2), (a) the P1-T_2 relation does not follow the model as P1 centers are no longer dominant in the total nitrogen concentration. (b) Taking non-negligible NVH^- centers into account, T_2 results still show a large scattering around the model.

nitrogen-related defects (Figure 3.8(b)). However, the T_2 values still show large fitting errors with the corrected model (even with similar distribution, as the NVH^- concentration is almost proportional to the P1 concentration). This indicates that either other undefined nitrogen-related defects exist in these samples, or other contributors rather than nitrogen need to be considered as the decoherence source. As

this series also shows darker coloration (grayish) for higher nitrogen-doped samples (will be discussed in Section 5.1), more complex influence factors are also expected for its T_2, which needs further investigations.

To conclude briefly, the results show that for low nitrogen concentrations the P1 incorporation is more stable (with an almost consistent [P1]/[N] ratio) than at high nitrogen concentrations, and the T_2 is less influenced by other nitrogen-related defects - this makes the merit of [P1]×T_2 easily controllable, which is the first step to optimize the sensitivity from the material side (Section 3.1). Localized optimization is required for high nitrogen concentrations in order to improve the P1 incorporation, which will be discussed in the next section.

Table 3.2: Spin densities (measured by EPR) and Hahn-echo T_2 in as-grown nitrogen series. P1 concentration brings a ∼6% error, while for the NVH^- and other spins larger error ∼20% has to be considered.

Series	Sample	As-grown P1 (ppm)	As-grown NVH^- (ppm)	Other spins (ppm)	As-grown T_2 (μs)
Nitrogen series #1	NDT-26	0.2	-	-	497.7 ± 26.2
	NDT-14	-	-	-	288.9 ± 31.3
	NDT-07	0.5	-	-	166.1 ± 8.7
	NDT-34	0.8	-	-	101.3 ± 3.3
	NDT-01	1.4	-	-	72.8 ± 1.5
	NDT-02	1.9	-	-	48.2 ± 1.0
	NDT-12	2.6	-	-	53.3 ± 1.4
Nitrogen series #2	Cas-40	3.2	1.3	0	15.3 ± 0.7
	Cas-48	5.2	1.6	2.7	15.9 ± 0.6
	Cas-68	7.8	3.2	8.5	1.3 ± 0.4
	Cas-44	9.5	8.2	7.8	1.9 ± 0.5
	Cas-51	11.2	8.0	10.2	2.8 ± 0.5
	Cas-49	13.0	12.6	18.7	10.6 ± 0.6
	Cas-50	19.3	16.6	17.5	0.3 ± 0.1

3.4 Other growth conditions for P1 incorporation and NV creation

The two nitrogen series were grown with varying nitrogen flow (thus varying N/C ratio) but fixed other parameters. The N/C ratio is the most relevant parameter that influences nitrogen incorporation in diamonds. The results above showed that at the lower end of the N/C ratio, the P1 incorporation and NV creation are stable with

a clear trend, while for a higher end, growth parameters show a stronger and more complex inter-dependency. Changing only the nitrogen flow brings large variations in diamond properties, e.g. P1 and NV creation efficiency and coherence time, later this thesis will also talk about their influence on diamond absorption (Section 5.1) and birefringence (Section 6.2). Localized optimization of growth parameters is required for each N/C ratio, which can help to improve the diamond quality remarkably. Julia Langer has conducted growth with varying parameters/conditions apart from the nitrogen flow (growth details see [137]), here this section discusses relevant conditions and how they influence the P1 incorporation and NV creation.

Based on the growth protocol of the sample Cas-50 from Nitrogen series #2, this section studies samples with a fixed nitrogen flow and varied other growth parameters, to understand how these parameters influence the P1 incorporation and NV creation (Figure 3.9 and Table 3.3). Figure 3.9(a) and (b) show respectively how P1 concentration and NV/P1 ratio change with the altered growth parameters.

Varying the methane flow directly changes the N/C ratio, e.g. lower methane flow leads to higher N/C ratios, thus higher P1 concentrations are expected. The result (sample Sn-73) confirms that. However, it was also found that too low methane flow leads to worse structural quality of the diamond, and the diamond shows higher potential to break during the growth [137]. In this sense, the methane flow should be set low for pursuing high P1 incorporation, while remaining high enough for a stable diamond structural quality.

Changing other parameters are less intuitive than the methane flow, as the N/C ratio remains constant. Some interesting facts can be observed from the result:

- Reducing the growth pressure leads to worse nitrogen incorporation: the sample exhibits fewer P1 and NVH^- centers.
- Lower total gas flux reduced the P1 incorporation, while remaining the NVH^- creation at a high level.
- Higher oxygen flow can promote nitrogen incorporation, meaning both the P1 and NVH^- concentration increase.

The NV creation, however, is relatively stable when compared to the P1 centers. The NV concentration is not increased significantly for higher P1 concentrations, and the NV/P1 ratio changes by these altered parameters, meaning that the ratio is no longer around 0.25% as discussed in Section 3.2 (but still in a regime <1%).

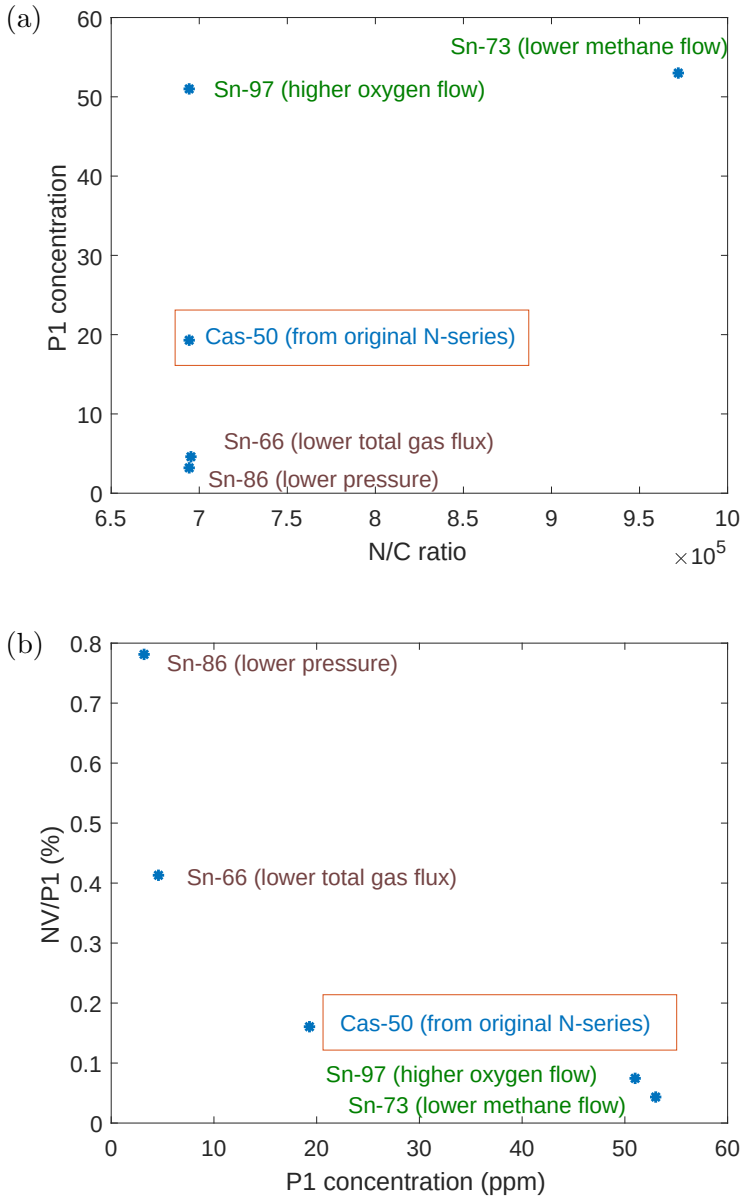

Figure 3.9: Based on the growth protocol of the sample Cas-50 (Nitrogen series #2), different growth parameters (with fixed nitrogen flow) change the P1 incorporation and NV creation remarkably.

Lower methane and higher oxygen flow promote the incorporation of P1 centers, while the NV creation is not enhanced in scale. For applications that prefer as-grown NV diamonds, this low NV/P1 ratio can be problematic as the high P1 concentration suppresses the NV coherence time (Section 3.1). Same NV concentration levels with fewer P1 centers can be beneficial. Nevertheless, for applications pursuing high NV concentrations (and a balance with the coherence time), a higher initial P1

Table 3.3: Varying growth parameters and their influences on the P1 incorporation and NV creation.

Sample	Parameters	P1 (ppm)	NV (ppb)	NVH^- (ppm)
Cas-50	Original protocol from Nitrogen series #2	19.3	31	16.6
Sn-66	Lower total gas flux	4.6	19	20
Sn-73	Lower methane flow	53	23	39
Sn-86	Lower pressure	3.2	25	2
Sn-97	Higher oxygen flow	51	38	35

concentration still has great value, and the low NV/P1 ratio can be overcome by after-growth treatments such as irradiation and annealing, which will be discussed in the next chapter.

Apart from the growth parameters, other growth conditions can also play important roles. For instance, the holder size shows a clear connection with nitrogen incorporation during the CVD growth. Larger holder sizes tend to improve the P1 incorporation, the NV/P1 ratio and other diamond properties (e.g. structural quality, absorption and homogeneity of birefringence). Details have been discussed earlier in [138] and [137].

General rules of the P1 incorporation, NV creation, NV charge state and the NV coherence time of the as-grown CVD diamond, as well as their interrelations are given in this chapter. The results show that after growth, nitrogen-doped CVD diamonds can acquire sufficient NV^- concentrations (up to 30 ppb), as well as long coherence times (up to 500 μs) for sensing requirements. The sensitivity can be further improved by irradiation and annealing steps after growth, which converts P1 centers into NV centers efficiently, increasing the NV/P1 ratio. According to Equation 3.1, with an enhanced NV PL signal I and a consistent coherence time τ, the sensitivity η can be improved. By optimizing the irradiation, one can maximize the P1-to-NV conversion rate, while performing the optimal combination of high NV PL signal, charge stability, and long T_2 time. The next Chapter discusses the optimization of the after-growth treatment to further improve the material performance.

Chapter 4

4 Optimizing NV center creation by after-growth treatments

Nitrogen-doped CVD growth can create diamonds containing NV centers up to tens of ppb level, however, they are still only a very small fraction of the incorporated P1 centers (<1%). Further conversion from P1 centers to NV centers is possible, and in many cases more favorable: for instance when requiring higher NV concentrations up to ppm levels (which is interesting for many NV-ensemble based sensing techniques [60, 102, 57]), it is not achievable by as-grown nitrogen-doped diamonds. Additionally, a low NV/P1 ratio in as-grown diamonds can deteriorate the sensitivity, as a high P1 concentration leads to short coherence time, while a low NV concentration provides limited NV fluorescence signal (which was discussed in Section 3.1). After-growth treatments, such as irradiation and annealing, exhibit remarkable benefits for enhancing the NV concentration and thus improve the sensitivity, which is often in demand by the creation procedure of the NV diamond.

This chapter investigates electron-beam (e-beam) irradiation and subsequent annealing steps on nitrogen-doped CVD diamonds to further create NV centers. The treatment conditions are optimized to maximize the P1 to NV^- conversion ratio, while remaining a stable NV charge state (meaning a high NV^-/NV ratio). Limits and criteria of the e-beam irradiation and annealing treatments on NV creation are suggested, as well as general rules to determine optimal irradiation fluences for different P1 densities. Furthermore, the change of T_2 on treated samples is also investigated, aiming for optimal combinations of enhanced NV^- concentrations with long coherence times to achieve improved sensitivities. The results of this chapter and Chapter 3 lead to the publication [116] of the author.

4.1 Further NV creation by after-growth treatments

Last chapter showed that after growth, nitrogen-doped CVD diamonds already contain remarkable NV center concentrations up to tens of ppb level. A large amount of the incorporated P1 centers (at the ppm level) still remain in the diamond, which can be further converted into NV centers. Problems arise for the sensitivity due to the low NV/P1 fraction (as discussed in Section 3.1), the high P1 concentration limits the coherence time τ while the low NV concentration can only exhibit weak fluorescence signal I, leading to small merit of $\sqrt{I \cdot \tau}$ thus a worse sensitivity. Another issue is that a high P1 concentration can also suppress the NV fluorescence [122] thus further deteriorating the sensitivity.

To further convert P1 centers into NV centers and thus enhance the NV concentration efficiently, subsequent irradiation and annealing treatments are commonly conducted, which have been discussed in previous works [120, 59]. The irradiation step creates vacancies in diamond, while the annealing step mobilizes vacancies [1, 84, 134, 79], enables P1 centers to trap them to form NV centers [27, 85, 86]. Different irradiation types can be applied for vacancy creation, including irradiation with electrons, ions, high-energy photons or neutrons [81, 82, 83]. For the NV-ensemble creation in bulk diamonds, electron irradiation is normally preferred, as it creates mainly isolated vacancies [13] but not multi-vacancies or vacancy clusters, homogeneously, while preventing further crystal damage. Di-vacancies or clusters are often created during the annealing after irradiation with high-energy (high-mass) particles like ions, neutrons, etc., which create multiple vacancies along their path through the material, i.e. close to one another. Moreover, with electron irradiation, one can achieve a penetration depth up to millimeters [83], which ensures homogeneous vacancy creation through the bulk diamond plate.

The irradiation fluence and electron energy are the two key parameters for e-beam irradiation. The fluence influences the vacancy concentration linearly, while the energy should have less influence on the vacancy number but decide the penetration depth [83]. Table 4.1 shows the theoretical values of the vacancy concentration and penetration depth for different electron energies. The table is extended from [83] with a calculation of vacancy concentrations in ppm. Here the table only shows the concentration with 1×10^{17} e/cm^2 irradiation fluence, other fluences result in concentrations that scale linearly to these values (e.g. for 0.25 MeV, a fluence of 1×10^{17} e/cm^2 can create 0.42 ppm vacancies, while for 2×10^{17} e/cm^2 it is 2×0.42=0.84 ppm). Depending on the initial P1 concentration in diamond, different vacancy concentrations

are required to achieve the sufficient and optimal creation of NV centers.

Table 4.1: Vacancy creation by e-beam irradiation, deduced and extended from [83].

Electron energy (MeV)	(Vacancies/electron)/cm	Vacancies for 1×10^{17} e/cm^2 (ppm)[1]	Penetration depth (mm)
0.25	0.74	0.42	<1
1	1.74	0.99	∼1
2	2.15	1.22	∼2.8
5	2.18	1.62	∼7.5
10	3.42	1.94	>7.5

[1] Calculated using the ^{12}C mass 1.99×10^{-23} g, and the diamond density 3.51 g/cm^3

The annealing step can be conducted after irradiation (also called 'subsequent annealing'), or during the irradiation (also called 'in-situ annealing' or 'high-temperature irradiation'). Although the in-situ annealing exhibits higher NV creation efficiency [79], it is challenging for higher temperatures and for controlling the temperature stability. The subsequent annealing, on the contrary, has been well established and is now still the mainstream process for its experimental simplicity. Different annealing conditions affect the NV creation significantly, which will be discussed in Section 4.2 with more details. Only subsequent annealing has been conducted for samples in this thesis, no in-situ annealing conditions are discussed.

E-beam irradiation and subsequent annealing steps on nitrogen-doped CVD diamonds enhance the creation of NV centers and the NV/P1 ratio. While pursuing high NV/P1 ratios, keeping a high NV$^-$/NV fraction is also crucial, as NV^0 centers are detrimental for two reasons: firstly it cannot be used for sensing and contributes as a fluorescence background that weakens the ODMR contrast [59], thus reduces the sensitivity (equation 3.1); secondly, more NV^0 indicates a lack of electron availability, which leads to stronger photo-ionisation [95], i.e. more NV$^-$ is converted into NV^0 when pumped with green light. When a P1 center and a vacancy combine into an NV center, it then needs other P1 centers as the donor to provide an electron to charge NV$^-$ [99, 100, 90, 101]. Consequently, when large amounts of P1 centers are converted to NV centers, an insufficient remaining P1 concentration potentially leads to more NV^0 formation rather than NV$^-$. In this sense, the irradiation condition should be optimized to maximize the P1 to NV$^-$ conversion rate (not to NV), while remaining a high NV$^-$/NV ratio. By systematically studying different treatment conditions, the next sections optimize the e-beam irradiation and annealing treatments for the NV creation and show general approaches to achieve

the optimization. Coherence time T_2 of treated samples are also discussed, showing optimal combinations of enhanced NV^- concentrations with long coherence times, which leads to improved sensitivities.

4.2 Annealing conditions for NV creation

In this chapter, e-beam irradiation and subsequent annealing steps were conducted for the CVD series to create vacancies and to ensure that vacancies are trapped by P1 centers and form NV centers. Annealing condition at 1000°C for 2 h was chosen in this thesis based on literature (which is discussed below) and previous experimental experience. Under such relatively low annealing temperature (<1200°C) and a good vacuum condition ($\leq 10^{-5}$ mbar during the annealing), the crystal quality is stable (Chapter 6). Surface damage rarely occurs under such annealing conditions, which, if happens, can be removed by a polishing step with a loss in the sample thickness of only several microns (which is acceptable considering the thickness of the bulk diamond plate is at hundreds of micron). Consequently, the main concern for the annealing condition should be the mobility of vacancies and the formation of nitrogen-related defects. The goal, to briefly conclude, is to create as many NV centers as possible, while changes in the coherence time should be also monitored.

Three important temperature nodes should be kept in mind when considering the annealing condition: firstly, 400°C is where vacancies and nitrogen atoms introduced by implantation migrate and annihilate with each other [88, 89], this is also one of the reasons why NV centers can be directly formed during the CVD growth, as the growth temperature is normally above 400°C. Secondly, above 800°C the diffusion of vacancies becomes significant [89, 49]. Then above 1000°C the NV centers tend to dissociate and possibly form other defects [49].

The subsequent annealing after irradiation is often chosen to be above 800°C to ensure the vacancy mobility, the exact temperature and duration need to be considered carefully based on the behavior of NV creation. Acosta *et al.* [27] and Eaton-Magaña *et al.* [139] have pointed out that the NV concentration keeps on increasing with the annealing temperature from ∼600°C and reaches a plateau at around 850°C, then it is stable until 1000°C [140]. From 1000°C to 1200°C, a decrease in total NV concentration has been observed, [86], where NV^- seems to drop dramatically and NV^0 decreases, leading to a reduced NV^-/NV ratio. (Interestingly, for the in-situ annealing of ion-implantation, NV^- seems to keep stable in this

temperature range, while NV^0 are largely dissociated, thus an increasing NV^-/NV^0 ratio has been suggested [141].) Also at this stage, more NV centers change their orientations [142]. In conclusion, the optimal annealing temperature for an enhanced NV^- concentration should sit in the range between 850°C and 1000°C.

The effect of annealing procedures on the NV coherence time has been also investigated in previous works [143, 141, 49, 94]. An elongated coherence time has been achieved for single NV^- centers by modestly increasing the annealing temperature from 800°C to 1000°C [141] (for 2 h); or for NV ensembles by annealing with higher temperatures, for instance 1200°C for 12 h [143] or 1500°C for 2 h [94]. In this regard, considering that the suitable temperature for NV creation ranges in 850-1000°C, the high end of 1000°C can be an optimal option for a potential benefit in the coherence time.

A typical annealing duration of 2-2.5 h at this temperature has been conducted [27, 79, 59], as a longer annealing time would not further enhance the NV concentration, while even showing the potential to lose NV concentrations [126, 144].

Based on the discussion above, a standard, subsequent annealing procedure at 1000°C for 2 h was conducted for samples discussed in this work as the last step to create NV centers. Higher temperature annealing (>1500°C) can be also interesting, as other diamond properties (rather than the NV creation) can profit from the procedure. This will be discussed in Chapter 5 with more details. Appendix B lists out some important temperatures and how they influence the NV creation and related diamond properties for an overview.

4.3 Optimizing electron-beam irradiation

To understand how the fluence and energy of the e-beam irradiation influence the NV creation, thus to optimize the irradiation conditions, two 'Irradiation series' have been grown, as shown in Figure. 4.1. The samples have been grown on 3×3 mm CVD substrates (Element Six, general grade SC plate CVD), then laser-cut from the substrate after growth, i.e. no substrate contributes to the characterization for these series. Fixed growth parameters have been applied to the series, resulting in the same initial P1 concentration of ∼2.2 ppm (estimated from the UV-Vis spectrum). Then the two series have been irradiated with respectively 2 MeV and 1 MeV electrons, with varying fluences. The annealing was performed after irradiation at

1000°C for 2 h in vacuum (∼10^{-5} mbar during the heating), according to the discussion in Section 4.2. Optical characterization has been conducted between each procedure and after the final annealing step. (Details of the contributions were listed in Section 1.4.)

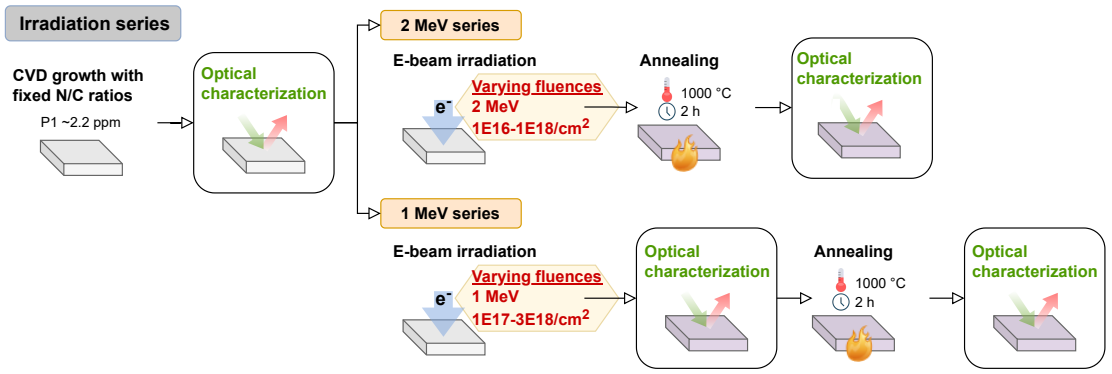

Figure 4.1: Flowchart of the NV creation in two Irradiation series. The two series were grown with varying nitrogen concentrations, then irradiated and annealed under the same conditions

The twp series show high PL consistency after growth (Figure 4.2, black markers at the bottom), indicating a stable NV concentration grown with the same protocol, and a stable NV/P1 ratio (as the P1 concentrations are all ∼2.2 ppm). After treatment, the total NV concentration increased significantly, positively correlated to the irradiation fluence (blue markers), with strong variations in the NV charge state distribution (orange and magenta markers). It can be observed that a remarkable charge state transition starting from 1×10^{17} e/cm^2 where NV$^-$ creation saturates and mostly NV^0 is produced with increasing fluence. Around 1×10^{17}-2×10^{17} e/cm^2 seems to be the optimal point with still enough P1 centers in the diamond to charge NV centers, but no excess which is positive for longer coherence times. The highest P1 to NV$^-$ conversion rate in this series was ∼8.9% for 1×10^{18} e/cm^2, however, a poor NV$^-$/NV ratio of only 53% was achieved. For 2×10^{17} e/cm^2 the P1 to NV$^-$ ratio was ∼7.3%, maintaining an NV$^-$/NV ratio of 66%, indicating better robustness against photo-ionization.

The 1 MeV series showed similar behavior in NV concentration and charge states, but shifted towards higher fluence by an order of magnitude (Figure 4.3), the optimum then shifted in a range of 1×10^{18}-3×10^{18} e/cm^2. This strong influence of the electron energy is in contrast to theoretical calculations (Table 4.1) which predict that the 2MeV irradiation with 1×10^{17} e/cm^2 creates roughly 1.22 ppm vacancies, while for

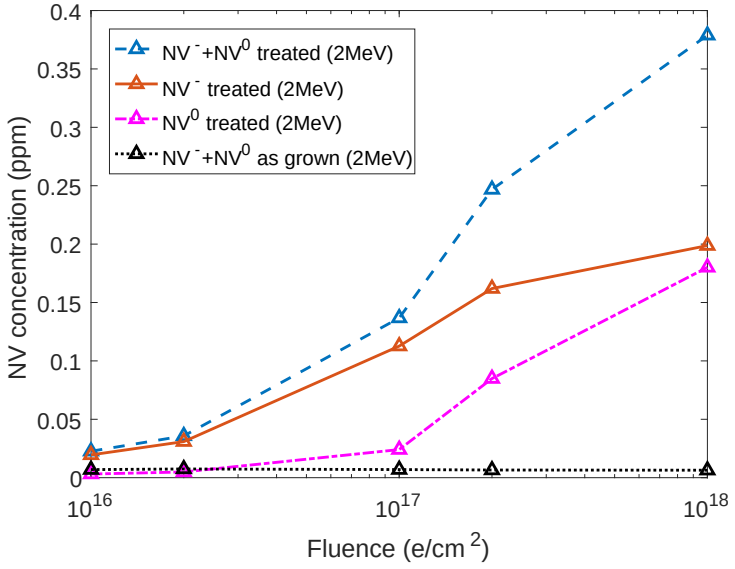

Figure 4.2: NV creation by e-beam irradiation (2MeV series). With different irradiation fluences, the total NV concentration increases with a turning point of $\sim 1\times10^{17}$-2×10^{17} e/cm^2, above which NV$^-$ centers are rarely created and mostly NV^0 centers are created for higher fluences. This turning point is taken as the optimal fluence.

1 MeV it is around 0.99 ppm with the same fluence, the vacancy concentrations differ slightly but not by an order of magnitude. Experimentally, the results contradict this and show that the question of the influence of electron energy on vacancy creation needs to be reconsidered. However as the two different energies were performed at different facilities, which might induce differences in the irradiation speed, the controlling method of the fluence, etc, studies of varying energies in the same facility can give more indications or confirm the result in the future.

For the same irradiation conditions, the NV concentration also depends on the initial P1 concentration. Four HPHT diamonds (Element Six, P1>20 ppm) were irradiated with 1 MeV electrons and the same fluences as for the 1 MeV CVD series, as an extension of the study for higher P1 concentrations (Figure 4.4). Compared to the 1 MeV CVD series, HPHT Ib diamonds showed higher NV concentration (exhibiting only NV$^-$, no NV^0) than the CVD series, since they contained initially more P1 centers (>20 ppm rather than 2.2 ppm in the CVD series) before irradiation. Their P1 to NV$^-$ conversion ratios (<3%) after treatments are however lower than the CVD series. This indicates that the vacancies created via irradiation were not fully converted into NV centers in the CVD series. However, the deviation between the HPHT series and the CVD series is small at low fluences and only becomes significant

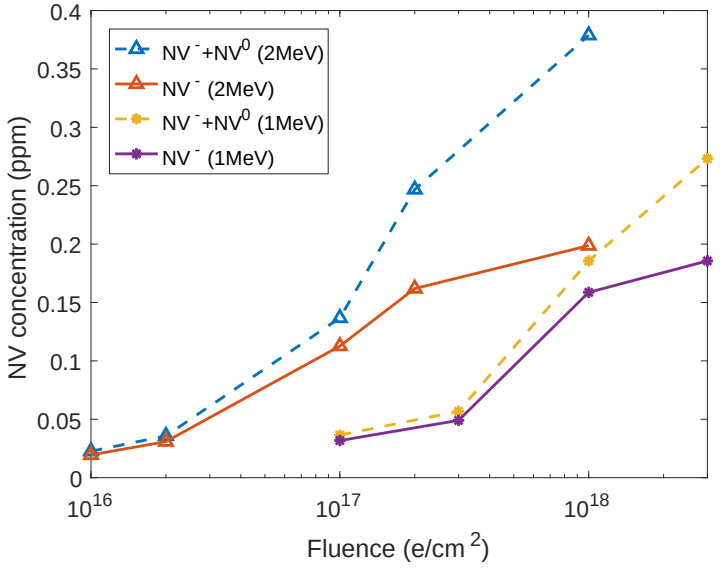

Figure 4.3: Compare different irradiation energies (1 MeV and 2 MeV): the whole NV creation and relative charge state show similar behavior, but a shift in the irradiation fluence of approximately one order of magnitude occurs. The optimal fluence for 1 MeV is at 1×10^{18}-3×10^{18} e/cm^2. The initial P1 concentration for all samples was ∼2.2 ppm.

when the NV creation reaches a point where it is also deteriorated in the creation of the NV$^-$ state.

Section 3.2 discussed vacancy-limited NV charge state distribution after CVD growth, as much fewer vacancies than P1 centers were in the diamond. After irradiation, it went to the point that the vacancy concentration (up to ∼30 ppm for 3×10^{18} e/cm^2 with 1MeV from the calculation according to Table 4.1) was in the same order with (or even higher than) the P1 concentration (2.2 ppm), vacancies have not been fully converted after annealing and the NV creation was P1-limited. Since NV$^-$ centers are charged by P1 centers, it was suspected that the NV$^-$/NV ratio is dependent on the remaining P1 centers after conversion to charge the NV centers. As support, for the two CVD irradiation series, their P1 concentrations have been measured twice, as after growth $[P1_{grown}]$ and after irradiation and annealing $[P1_{remain}]$. After treatment, the NV$^-$/NV ratio seems in fact to be determined by the ratio R_{re}=NV/P1$_{remain}$, independent of irradiation fluence or energy (Figure 4.5). When R_{re} >10%, the NV$^-$ ratio starts to decrease largely. As P1$_{grown}$ is partially converted to NV centers (and possibly other defects) during the treatment, $[P1_{remain}]$ as the final state is always less than $[P1_{grown}]$. The conversion rate from P1$_{grown}$ to NV centers after treatment, denoted as R_{con}=NV/P1$_{grown}$, always fulfills

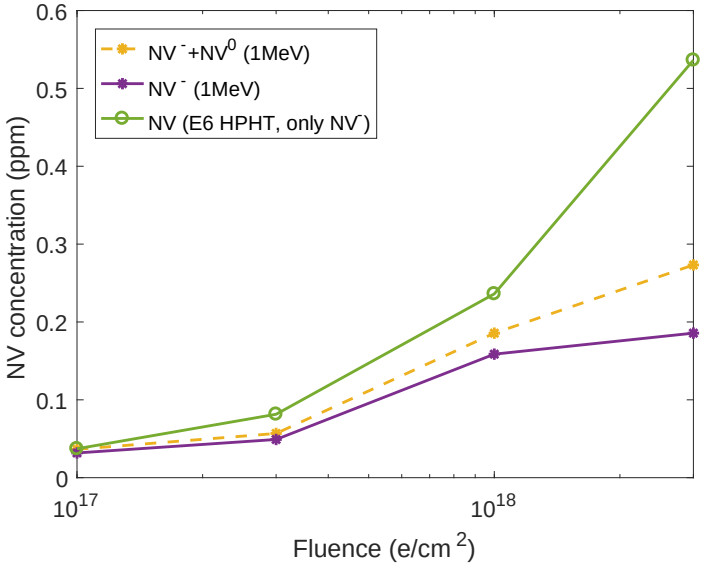

Figure 4.4: Initial P1 concentrations influence the total NV creation and the relative charge state: irradiated with the same fluence, the HPHT samples (P1>20 ppm) show higher NV concentrations than the CVD series (P1∼2.2 ppm), and they still exhibit only NV^- after high-fluence irradiation.

$R_{con} < R_{re}$, consequently R_{con} <10% is required to achieve NV^-/NV>80%. Given that the photo-ionization can be largely promoted by higher green laser power [123], the NV^-/NV ratios here were measured with lower laser power (10 μW confocal, details see Section 2.2) represent the intrinsic NV-charge-state distribution and usually get worse at high power densities. Therefore to achieve a high charge state stability, the author takes R_{con} <10% as an important criterion for the fabrication.

Another criterion that can be interesting for some applications is R_{re} ∼35%, for which half of NV centers will be in the neutral form NV^0. This means to remain NV^- dominated, $R_{re} < 35\%$ is required. For an initial P1 concentration of 2.2 ppm, the optimum can be set depending on different purposes. When focusing on the NV-charge-state stability, an optimum is suggested at 1×10^{17} e/cm^2 for 2MeV electron, or 1×10^{18} e/cm^2 for 1MeV electron, resulting in an NV^-/NV ratio of ∼82-86%. When focusing on the total NV creation, the optimum can be set to 2×10^{17} e/cm^2 with 2MeV electron, or 3×10^{18} e/cm^2 with 1MeV electron, resulting in an $P1_{grown}$ to NV^- conversion rate R^-_{con} of ∼7.3-8.4% while remaining an NV^-/NV ratio of ∼66-68%. (More details see table 4.2)

Previous literature has often tried to achieve high conversion ratios without regard

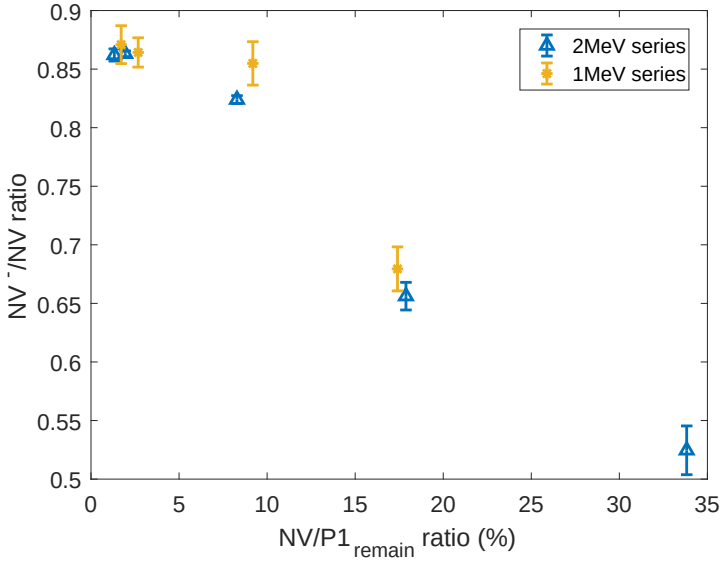

Figure 4.5: Criteria for the e-beam irradiation on nitrogen-doped bulk CVD diamond: for $NV/P1_{remain}$ >10%, the NV charge state shifts significantly towards NV^0; for $NV/P1_{remain}$ >35%, NV^0 potentially becomes the dominant charge state. Errors are defined as in Figure 3.4.

Table 4.2: NV charge states distribution and P1 to NV conversion ratios of different irradiation energies and fluences. All samples have an initial P1 concentration of ∼2.2 ppm.

Series	Sample	Fluence (e/cm^2)	NV^-/NV (%)	$NV/P1_{remain}$ (%)	$NV^-/P1_{grown}$ (%)
2 MeV series	I2-01	1×10^{16}	86.2 ± 0.5	1.3	0.9
	I2-02	2×10^{16}	86.3 ± 0.2	1.9	1.4
	I2-04	1×10^{17}	82.4 ± 0.3	8.3	5.1
	I2-05	2×10^{17}	65.5 ± 1.2	17.6	7.3
	I2-08	1×10^{18}	52.5 ± 2.1	33.3	8.9
1 MeV series	I1-39	1×10^{17}	87.1 ± 1.6	1.7	1.4
	I1-50	3×10^{17}	86.4 ± 1.3	2.7	2.2
	I1-28	1×10^{18}	85.5 ± 1.9	9.5	7.2
	I1-29	3×10^{18}	67.9 ± 1.9	15.3	8.4

for the NV charge state. The results in this section show that the NV charge state needs to be taken into account. The two criteria that are given from the results should be generally applied for CVD diamonds that use the same treatments to create NV centers.

It was also noticed that previous works have applied different methods to determine the NV concentration, which was discussed in Section 2.2. Until now there is no

systematic study of consistency between different methods. Nevertheless, Section 2.2 also pointed out that NV-PL-based methods are most commonly used, and it is an excellent way to evaluate the NV concentration, as it links directly to the sensing applications. Comparisons between results obtained by different methods should be treated carefully, in this thesis the method introduced in Section 2.2 is used consistently. The trends and rules that are discussed for the NV creation should be generally applicable in CVD diamonds.

Table 4.3: NV creation ratios in related works.

Reference	NV^-/NV	$NV^-/P1_{grown}$	Type
This work	85.5%	7.2%	Bulk, nitrogen-doped, high [NV]
Edmonds *et al.* [59]	62%	18.2%	Bulk, nitrogen-doped, high [NV]
Schloss *et al.* [60]	65.5%	14%	Bulk, nitrogen-doped, high [NV]
Herbschleb *et al.* [24]	∼100%	unspecified	Bulk, phosphorus-doped, low [NV][(1)]
Lühmann *et al.* [61]	unspecified	75%	Near-surface spot;[(2)] sulphur and nitrogen implanted, high [NV]

[(1)] No nitrogen doping or implantation has been conducted.
[(2)] Spot with a diameter∼20 μm, penetration depth<0.1 μm limited by the implantation technique.

The NV creation ratios in related works are listed in Table 4.3. For similar NV-creation processes (Schloss *et al.* [60] and Edmonds *et al.* [59]) to this thesis, the individually achieved conversion and charge state ratios follow the general criterion that was put forward above, i.e. $NV^-/NV<80\%$ for R_{con} >10%. The author also acknowledges that these limitations can be potentially overcome by additional treatments. For instance, Herbschleb *et al.* [24] and Lühmann *et al.* [61] have shown that doping or implanting with other n-type impurities (e.g. phosphorus or sulfur) can improve the conversion efficiency and the NV^- fraction. The explanation is that these additional n-type impurities provide more electrons to charge NV^- rather than only P1 centers as the donor. Although these works were driven by different aims in NV creation and have shown limitations in their processes, they still inspire a possible direction to improve the NV creation in bulk nitrogen-doped CVD diamond. Co-doping with another electron donor during CVD growth can be a potential pathway, namely doping with nitrogen and another impurity simultaneously, to remain

a high P1 concentration while providing more electrons to charge NV^- in a later process.

4.4 Spectral study for irradiation and annealing

The PL study after irradiation and annealing steps provides an overview of the 'final state' for the NV creation. The spectral study gives further insight into the defect transformation, especially the vacancy creation, the vacancy charge state's behavior, and how they influence the NV creation during the treatment steps. This section studies the absorption spectrum of the 1 MeV series in the UV-Visible range to visualize the defect transformations via irradiation and annealing. A new approach to measure an indication of the resulting NV charge state before annealing is identified, i.e. before NV centers are even created - this can be used to assess fluences before annealing.

Figure 4.6a shows the absorption spectra after irradiation with different fluences. Subtracting the irradiated spectra from the as-grown ones, see Figure 4.6b, one can clearly identify the creation of single vacancies and distinguish its negatively charged and neutral forms. The irradiated spectra showed a significant change in a band centered at ∼365 nm, reported to be the ND1 absorption band caused by negatively charged single vacancies (or V^-) [147, 148], with three small peaks at 393 nm, 375 nm and 384 nm, corresponding to its zero phonon line (ZPL) and two phonon replicas respectively. The result demonstrated that the ND1 band increased with irradiation fluence, conforming with the argument that electrons should mainly create isolated vacancies, which accept electrons from the electron-donating P1 centers. For a strong irradiation fluence, for instance 3×10^{18} e/cm^2 curves in Figure 4.6, a significant GR1 band (corresponds to V^0) appeared, showing a ZPL at 741 nm and a broad feature from ∼500-750 nm [107]. GR1 centers are normally generated by high energy irradiation, although a high nitrogen concentration can promote the conversion from GR1 to ND1 [107, 148]. At this stage of the processing, the vacancies are the main electron acceptors and these will be converted to NV centers in the subsequent annealing step. The main electron donors are the P1 centers. Assuming that the vacancies are charged by the P1 centers and that with increasing vacancy creation, there might be a point where the availability of electrons is limited by the P1 density, this point could be identified by the appearance of neutral vacancies (GR1 centers) instead of negatively charged vacancies (ND1 centers). As

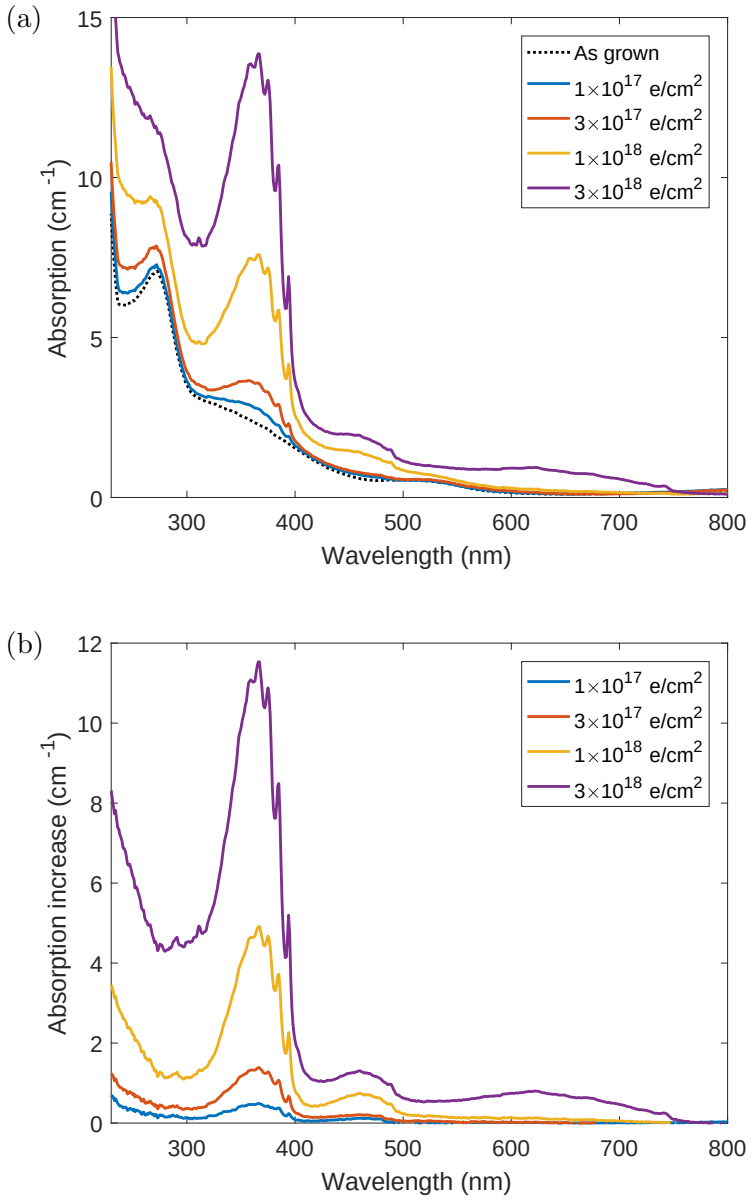

Figure 4.6: (a) Absorption spectra (absorption A defined by Equation 2.4) and (b) absorption increases (the irradiated spectrum subtracted by the as-grown spectrum) of the 1 MeV irradiation series after irradiation, before annealing. The spectra show clear ND1 bands (V^-, with a ZPL at 393 nm and two phonon replicas at 375 nm and 384 nm), increasing with the irradiation fluence. For the highest fluence (3×10^{18}e/cm^2), the GR1 band (V^0, with a ZPL at 741 nm and a side band at ~500-750 nm) can be observed. Additionally, an absorption band at ~460 nm appears after irradiation, which links to a defect containing nitrogen atom bound to interstitial carbon atoms [145, 146].

the vacancies are converted to NV centers during annealing, the appearance of neutral vacancies before annealing might indicate the appearance of neutral NV centers after annealing. This is supported by the fact that only the sample with irradiation fluence of 3×10^{18} e/cm^2 shows a strong GR1 band after irradiation and significant NV^0 centers after annealing, see Figure 4.3. Thus, the appearance of GR1 centers in irradiation can potentially be used to determine the ideal fluence for NV creation, even before annealing.

Additionally, the spectrum after irradiation showed an increase in the 'ramp', which was defined by Khan *et al.* describing the gradual increase of absorption with decreasing wavelength [113]. It has been suggested that the 'ramp' could be related to vacancy clusters [117, 118], however, this can hardly explain the increase of the 'ramp' induced by e-beam irradiation, as electrons should not create significant multi-vacancy defects, at least for low fluences. Moreover, the 'ramp' fell down again after annealing (Figure 4.7), but the annealing temperature (1000°C) was below the dissociation point of vacancy clusters (∼1500°C) [107]. To conclude, the defect that increased the 'ramp' was induced proportional to the irradiation fluence, it can be largely annealed out at 1000°C, this suggests that single vacancies can contribute to the 'ramp'. But the exact cause of the 'ramp' and how it influences the NV formation still needs further investigation. Furthermore, a center with ZPL at 489 nm (and a phonon side band centered at ∼460 nm) appeared after irradiation. The 489 nm center was attributed to a defect containing nitrogen atom bound to interstitial carbon atoms [145, 146], after annealing it vanished due to its low-temperature-stability [148].

After annealing, vacancies were captured by P1 centers to form NV centers, resulting in a significant decrease in the ND1 band and an increase in the NV band (ZPL at 637 nm for NV^-, phonon side band across to ∼450 nm), Figure 4.7. The ZPL for NV^0 (575 nm) is not visible and only the broad side band of NV^- can be seen for low fluences, but for the highest fluence (3×10^{18} e/cm^2), due to the high concentration of NV^0, the ZPL for both NV^- and NV^0 can be observed. For high fluences, isolated vacancies were not fully annealed out, which was particularly obvious for 3×10^{18} e/cm^2 irradiation in Figure 4.7b, that both ND1 and GR1 bands remained a considerable intensity. The reason can be either that the annealing temperature or duration was insufficient to convert all single vacancies, or more likely, P1 centers were much less available due to already high conversion, leading to a worse combination rate and a higher proportion of NV^0–which has been confirmed by the NV-PL result (Figure 4.4). The absorption and PL behavior of the series drove to the same

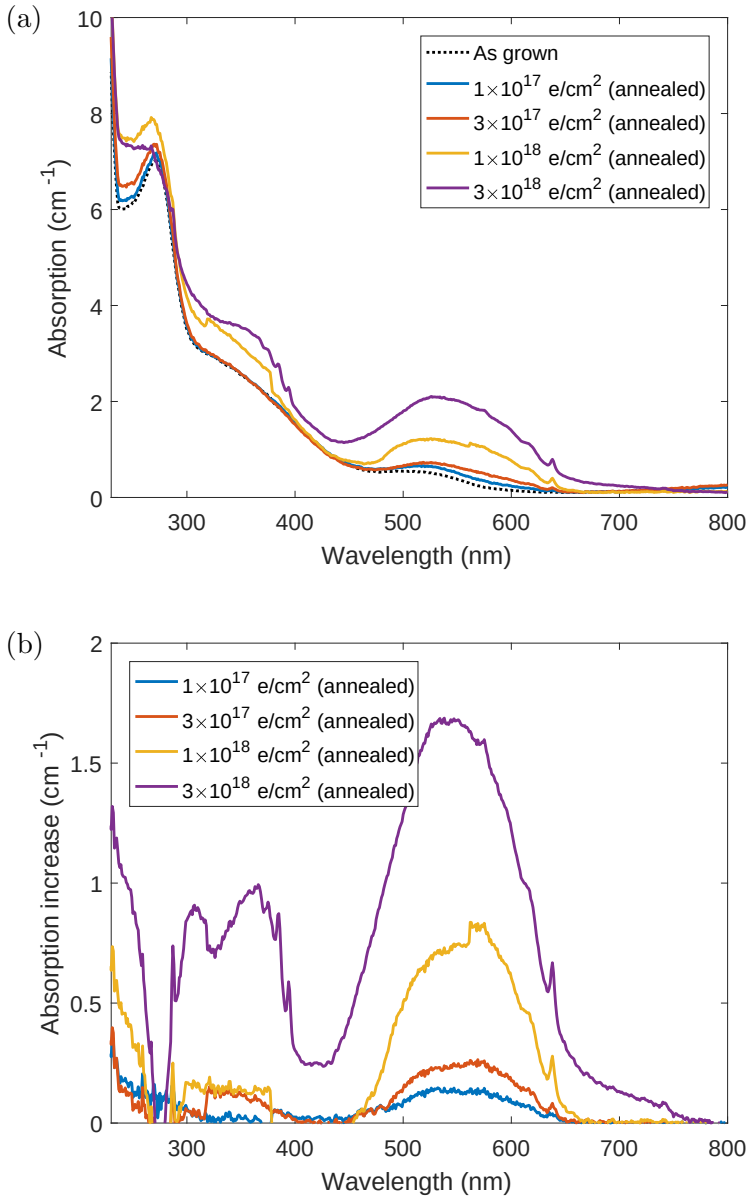

Figure 4.7: (a) Absorption spectra (absorption A defined by Equation 2.4) and (b) absorption increases (the annealed spectrum subtracted by the as-grown spectrum) of the 1 MeV irradiation series after annealing. The spectra show significant decreases in the ND1 band and increases in the NV band. The NV concentration is proportional to the irradiation fluence. For the highest fluence, both V^- and V^0 centers were not fully converted.

conclusion, that an optimal fluence should be between $1{\times}10^{18}$ to $3{\times}10^{18}$ e/cm^2 in 1 MeV irradiation for diamonds with 2.2 ppm P1 centers. This gives further support to the assumption that the appearance of GR1 centers after irradiation can indicate the NV^0 creation after annealing. Thus, the UV-Vis spectrum can help to decide if

further irradiation is appropriate, therefore it can be used to determine the optimal irradiation fluence sufficiently before annealing.

4.5 NV creation for varying initial P1 densities

After investigating different irradiation conditions on samples with the same P1 density, in turn as the next step same irradiation conditions were applied to samples with varying P1 densities. As shown in the floatchart (Figure 4.8), Nitrogen series #1 (0.2-2.6 ppm P1) was irradiated with 2×10^{17} e/cm^2 fluence, Nitrogen series #2 (3.2-19.3 ppm P1) with 5×10^{17} e/cm^2, both with an electron energy of 2 MeV. For the details of the two series see Section 3.2 and Appendix A.

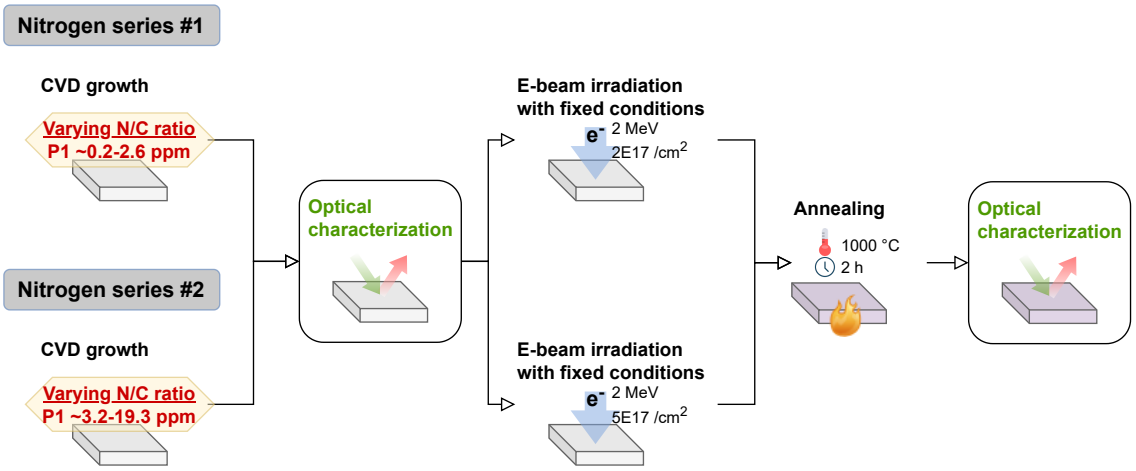

Figure 4.8: After-growth treatments on the two nitrogen series. Both series were irradiated with 2 MeV electron energy, the fluence for Nitrogen series #1 was 2×10^{17} e/cm^2, for Nitrogen series #2 was 5×10^{17} e/cm^2. After irradiation they have been annealed at 1000°C for 2 h.

This fluence was chosen based on the discussion of optimal irradiation conditions in previous sections. For 2.2 ppm P1 (2 MeV irradiation series in Section 4.3), an optimal fluence regime sits in 1×10^{17}-2×10^{17} e/cm^2. Therefore a fluence of 2×10^{17} e/cm^2 is rational for the Nitrogen series #1 with a highest P1 concentration of 2.6 ppm, since this should achieve optimal conversion for the samples with high P1 concentration. The Nitrogen series #2 covers a much larger range of the P1 concentration than the series #1, to find a suitable fixed fluence for it therefore needs more consideration, since different P1 concentrations call for different optimal fluences and the samples with high nitrogen in the series #2 showed an increasingly dark coloration.

If choosing an optimal fluence for the highest P1 concentration (19.3 ppm) in this series, for all other samples with lower P1 concentrations the fluence will be too high. A fluence suitable for the middle range of P1 concentration (i.e. ∼10 ppm) can prevent from over-irradiating almost all samples, and potentially help better observe the dynamic of NV charge state changes under the same irradiation conditions. Here comes the question, what should be the optimal irradiation fluence for 10 ppm P1 concentration? Assuming the optimal fluence is linear to the P1 concentration, then the optimal range for 10 ppm should be 4.5×10^{17}-9×10^{17} e/cm^2. From this range, an irradiation fluence of 5×10^{17} e/cm^2 was decided for this series.

Figure 4.9 illustrates the NV concentration and charge state ratio of the series #1 after irradiation and annealing (also see Table 4.4). The NV creation was P1-limited under this irradiation condition, leading to a positive correlation between the NV and initial P1 concentration. The sample with 2.6 ppm P1 concentration shows the highest NV concentration and NV^-/NV ratio, as the fixed irradiation condition was optimized for a slightly lower P1 concentration of 2.2 ppm. This means the P1 concentration in this sample should be enough to charge the NV^- center, compared to the optimum in the irradiation series. In the end it contains 168 ppb NV^- centers with 67% NV^-/NV ratio, $R^-_{con} \sim 6.5\%$. For the other samples with P1<2.6 ppm, more NV^0 presented due to over-irradiation, meaning the irradiation-induced vacancies converted too many P1 centers to NV centers, such that the remaining P1 concentration was no longer able to provide electron charges to the NV centers. This signifies the high relevance of limiting irradiation in order to preserve the charge state of the NV^- center and confirms the determined optimum for NV^- creation from Section 4.3. Consequently, the NV^-/NV ratio (Figure 4.9(b)) showed a linear correlation to the initial P1 concentration, providing evidence that the optimal fluence can be positively correlated to the as-grown P1 concentration.

Nitrogen series #2 was expected to show similar behavior. Since the irradiation fluence was chosen to be the optimum for 10 ppm P1 concentration, the samples with lower P1 concentration were expected to be over-irradiated and show a low NV^-/NV ratio, while samples with higher P1 concentration should be insufficiently irradiated, and therefore remain a high NV^-/NV ratio. The total NV concentration might exhibit an increasing trend (although might not be linear), positively correlated to the initial P1 concentration, as the initial P1 concentration influences the NV creation under the same irradiation fluence.

However, the experiment data does not meet the expectation, Figure 4.10 and Ta-

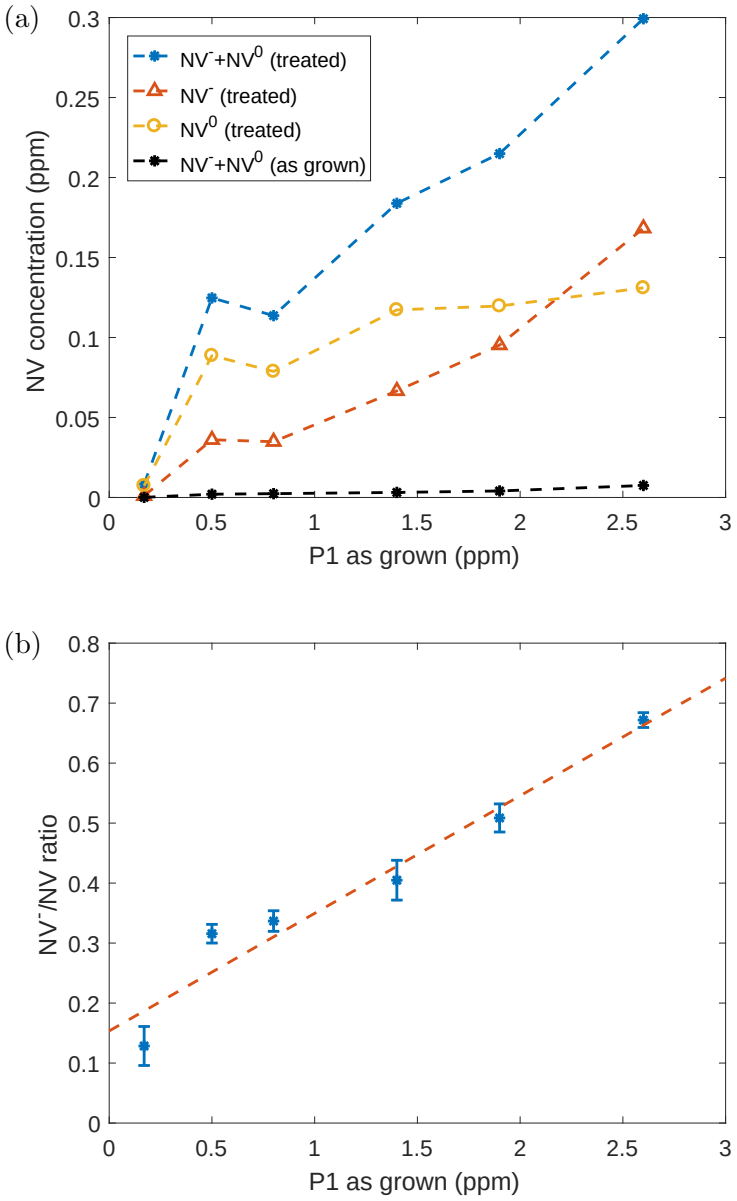

Figure 4.9: The Nitrogen series #1 has been irradiated with 2 MeV, 2×10^{17}e/cm^2, which was optimized for ∼2.2 ppm P1 concentration. After irradiation and annealing, (a) the NV concentration increased with the increasing as-grown P1 concentration. The fixed fluence leads to different NV charge state distributions (illustrated by the connecting lines). (b) The NV^-/NV ratio showed a linear correlation with the as-grown P1 concentration.

ble 4.4. Although the average NV concentration of the series #2 is higher than the series #1 (which can be explained by the 2.5 times higher irradiation fluence), no clear trend of the NV creation is shown as a function of the initial P1 concentration,

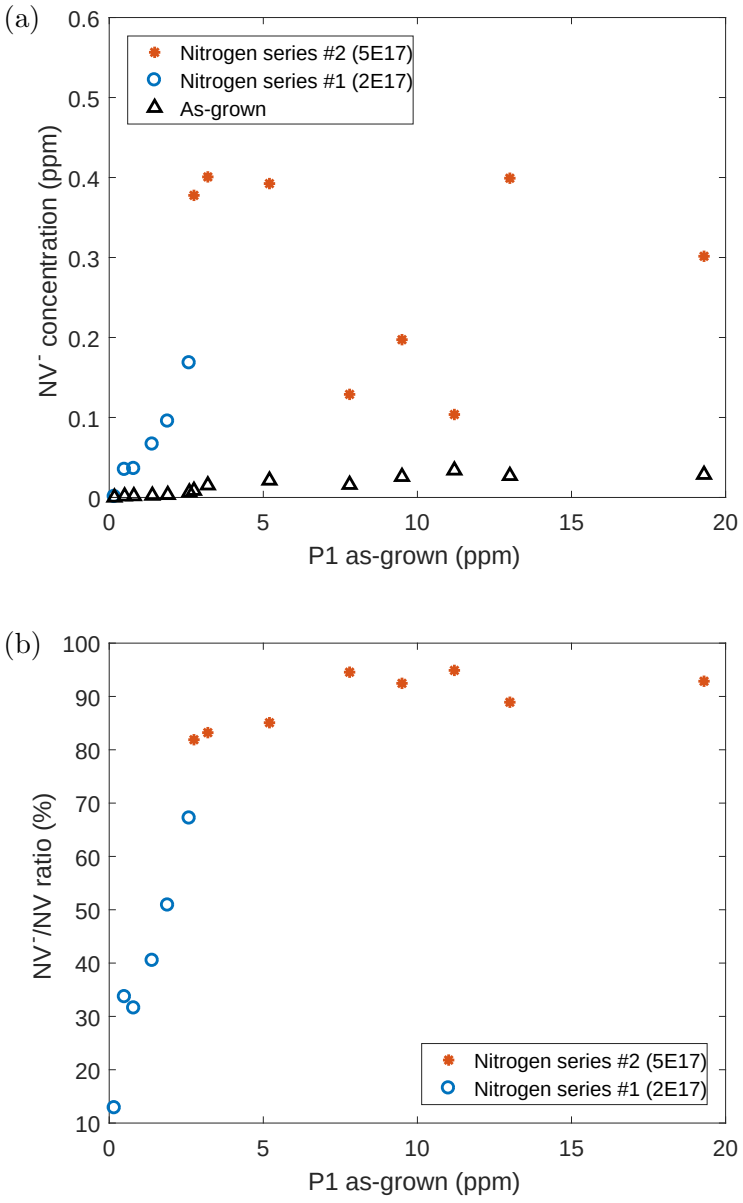

Figure 4.10: The Nitrogen series #2 has been irradiated with 2 MeV, 5×10^{17}e/cm^2. After irradiation and annealing, (a) the NV concentration does not show a clear trend, (b) the NV$^-$/NV ratios are all above 80%. No significant over-irradiation has been observed for lower-P1-density samples.

different from the series #1 that shows an almost linear correlation. The three samples around 10 ppm (i.e. sample Cas-68, -44 and -51), for which the optimal fluence has been chosen, even show lower NV concentrations than the other samples. The NV$^-$/NV ratios are all above 80% and none of the samples have been over-irradiated. To better understand the P1 conversion in this series, their P1 concentrations were

measured after treatments ($[P1_{remain}]$) by EPR. It was found that a large percentage of the converted P1 centers were not turned into NV centers but formed other defects. Possible candidates might not include NVH^-, as the EPR measurement shows that after treatments, the NVH^- band decreases with the P1 band. The overall low NV creation rate can be due to the formation of other nitrogen-related defects, or simply because the irradiation fluence was not high enough for the series with such electron energy (as no remarkable over-irradiation appears for lower-P1 samples). It is also interesting to further investigate if vacancies were bound by other defects than P1 centers. Given that these samples were dark, they probably had a very high density of intrinsic defects, which are likely to bind vacancies as they could release stress locally (discussed in Chapter 6). Different defects and varying defect densities between samples might have led to this unusual behavior.

Table 4.4: NV creations of the nitrogen series after treatments. Nitrogen series #1 was irradiated with 2×10^{17} e/cm^2 while for series #2 a fluence of 5×10^{17} e/cm^2 was chosen, both with 2 MeV electron energy.

Series	Sample	A-grown P1 (ppm)	Treated P1 (ppm)	Treated NV^- (ppb)	Treated NV^-/NV (%)
Nitrogen series #1	NDT-26	0.2	-	1	12.8 ± 1.7
	NDT-14	-	-	10	38.4 ± 3.3
	NDT-07	0.5	-	36	31.6 ± 1.6
	NDT-34	0.8	-	35	33.7 ± 3.0
	NDT-01	1.4	-	67	40.5 ± 3.3
	NDT-02	1.9	-	95	50.9 ± 2.3
	NDT-12	2.6	-	168	67.2 ± 1.2
Nitrogen series #2	Cas-40	3.2	-	401	83. 2
	Cas-48	5.2	3.8	392	85.1
	Cas-68	7.8	6.6	129	94.5
	Cas-44	9.5	7.8	197	92.5
	Cas-51	11.2	-	104	94.9
	Cas-49	13.0	5.8	399	88.9
	Cas-50	19.3	13.2	302	92.9

It was noticed that in series #2, directly after growth, the three samples around 10 ppm P1 (i.e. sample Cas-68, -44 and -51) and the sample with the highest P1 (i.e. sample Cas-50) exhibited grayish coloration and less transparency (i.e. are more absorptive) than the other samples. This can contribute to their unexpected low NV concentration after irradiation: either the cause of the grayish coloration deteriorates the conversion from P1 centers to NV centers, or/and it suppresses the NV fluorescence. Additionally, the grayish color of these samples can also link to

their short coherence times (Section 3.3). These many clues indicate that the grayish coloration of high-nitrogen CVD diamonds is in general harmful to the material properties. To understand its causes and investigate how to relieve this problem during the growth or via after-growth treatments, absorption experiments were conducted and are discussed in Chapter 5.

4.6 Improved material-limited sensitivity after treatments

As discussed in the last section, irradiation and annealing can largely enhance the NV concentration in CVD diamonds, leading to a stronger fluorescence signal I. This is the first approach to a better sensitivity according to the discussion in Section 3.1: a large value of $\sqrt{I \cdot \tau}$ is required, where the coherence time τ is another key factor. To elongate the coherence time of NV-ensemble by after-growth treatments is rather difficult. In this regard, the treatments should be chosen to be focused on increasing the NV density and thereby the intensity I. However, the coherence time should not decrease to give a true gain in sensitivity.

Therefore the T_2 of the Nitrogen series #1 was measured before and after treatments (details of contributions see Section 1.4). Figure 4.11 shows their T_2 as a function of the as-grown P1 concentration before and after irradiation. After treatment, the T_2 stays approximately consistent, for some samples the T_2 is even elongated, while for all of them the NV concentration increased significantly (Figure 4.9a).

More details of NV^- concentrations and T_2 times of the series are listed in Table 4.5. After irradiation and annealing, the series obtains an NV^- concentration of 1-168 ppb with a T_2 time of 46-549 μs. The longest T_2 time achieved in this series, 549 μs (NDT-26), is comparable to previously reported T_2=600 μs for NV ensembles [4] in diamonds with a natural abundance of 1.1% ^{13}C, but our NV concentration is higher (1 ppb NV^- centers in this work vs. $\sim$0.18 ppb NV centers in Stanwix *et al.*). The longest T_2 in this series is also close to reported T_2 times for single NV of $\sim$600-650 μs [3, 149]. Thus this sample is a significant achievement of long coherence time with comparatively high NV density.

As discussed in Section 3.1, considering that the coherence time is restricted by the P1 concentration, the product of them ([P1]$\times$T$_2$) has an upper boundary which

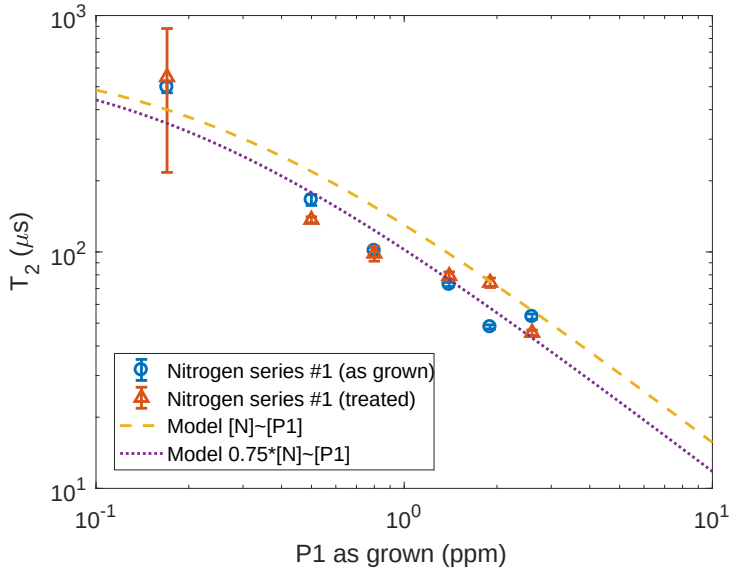

Figure 4.11: Coherence time T_2 of Nitrogen series #1 after irradiation and annealing stays consistent with the as-grown result, some are even elongated (details see Table 4.5). The error is given as discussed in Sec 3.3.

limits the sensitivity in theory, and this is the main consideration of the material-limited sensitivity. According to equation 3.1, the NV fluorescence signal I plays a more direct role than the P1 concentration, making the merit of $[NV^-]\times T_2$ even more important than $[P1]\times T_2$. Since P1 centers can be only partially converted into NV^- centers, P1 centers can never fully attribute to the signal I, however, enhancing the P1 to NV^- conversion rate can push the sensitivity closer to the limit. The product of NV^- and T_2 ($[NV^-]\times T_2$) in this CVD series increased from 20-70 times via optimizing the e-beam irradiation, leading to an increase in the $\sqrt{I \cdot \tau}$ factor of around 4-8 times (Table 4.5). On the other hand, the ODMR contrast C is equally important to the $\sqrt{I \cdot \tau}$ as C appears linearly in the sensitivity - this calls for a high NV^-/NV ratio. In this series, as discussed in Section 4.5, the sample NDT-12 with 2.6 ppm P1 shows the highest NV^-/NV ratio after irradiation and annealing steps. All other samples with lower nitrogen concentrations–although they have longer T_2–contain high proportions of NV^0 centers. By adapting irradiation fluences for corresponding P1 concentrations, high NV^- concentrations and NV^-/NV ratios can be both satisfied. That, coupled with the optimization of the growth for long T_2 times (to improve the crystal quality and reduce other dephasing sources except for nitrogen), provides possibilities to further improve the sensitivity, by modulating the combination of NV^- concentrations and T_2 times.

Table 4.5: NV creation, coherence time T_2 and improvement of sensitivity for Nitrogen series #1 after treatments.

Sample	As-grown NV^- (ppb)	Treated NV^- (ppb)	As-grown T_2 (μs)	Treated T_2 (μs)	Magnification $\sqrt{I \cdot \tau}$
NDT-26	0.03	1	497.7 ± 26.2	549 ± 332	6
NDT-14	0.2	10	288.9 ± 31.3	329.3 ± 101.8	8
NDT-07	1.5	36	166.1 ± 8.7	136.9 ± 3.9	4
NDT-34	1.8	35	101.3 ± 3.3	98.5 ± 7.1	4
NDT-01	2.4	67	72.8 ± 1.5	79.1 ± 3.2	6
NDT-02	3.3	95	48.2 ± 1.0	74.2 ± 3.4	7
NDT-12	6.4	168	53.3 ± 1.4	45.5 ± 1.2	5

Chapter 5

5 Absorption study of nitrogen-doped diamonds

Magnetometry with NV-ensembles in bulk diamonds benefits from high NV concentrations (Section 3.1). Other diamond properties can also show decisive influences depending on the application demand. For advanced techniques requiring large sensing volumes, for instance multi-pass readout, optical cavity coupling or laser cavity sensing, specifically low absorption and low birefringence in the material are also crucial prerequisites [57].

This chapter studies the correlation between the nitrogen/NV concentration and the diamond absorption, and discusses the feasibility to combine high NV densities and low absorption. Furthermore, this chapter investigates methods to reduce the absorption for highly NV-doped diamonds, in order to improve the material quality.

5.1 Absorption coefficient at 700 nm

As discussed in Section 1.2, when excited by a green laser, the NV^- center shows an emission feature with a ZPL at 637 nm and a broad PSB centered at around 700 nm. Most of the NV-fluorescence is also located around the center of PSB, making this regime ($\sim$700 nm) of large importance for applications that are based on the NV emission. All optical readout suffers from absorption, for advanced techniques such as multi-pass configurations, optical cavity coupling or laser cavity sensing, the absorption of the signal light is the main optical loss inside the material. As an example, stimulated emission of NV^- centers [95] and laser-threshold magnetometry

(LTM) [52, 57] is a way to significantly enhance sensitivity. For them, a very low absorption at ∼700 nm is needed to achieve net optical gain and lasing. Understanding the source and cause of the absorption in this regime plays a crucial role to improve the material quality and the performance of the application.

Figure 5.1 shows a typical absorption spectrum of the as-grown CVD diamond. As also discussed in Section 2.1.2 for the diamond spectral analysis, the CVD diamond has three characteristic absorption bands: a 270 nm band for P1 centers [110, 111, 112]; a 360 nm band originates from vacancy clusters [113, 114]; and a 520 nm band, for which the cause is controversial but has been assigned to NVH^0 centers in [113].

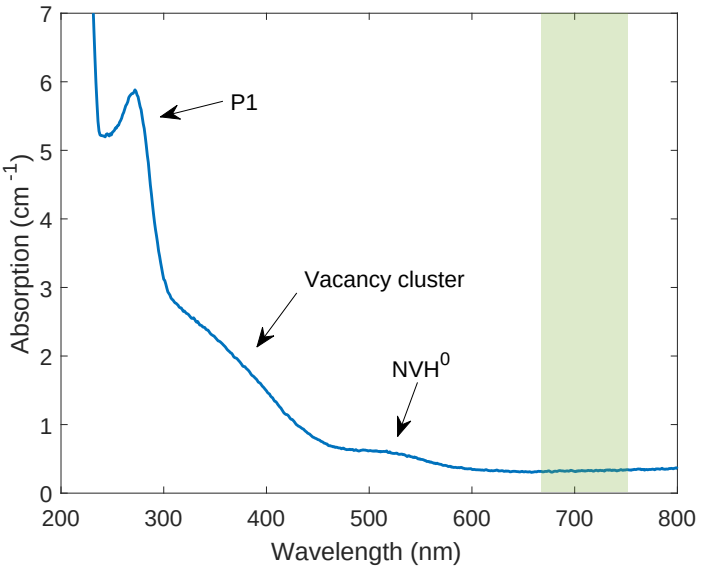

Figure 5.1: A typical UV-Vis spectrum of the as-grown CVD diamond with three absorption bands (270 nm, 365 nm and 520 nm). The absorption at ∼700 nm is most interesting for multi-pass configurations and techniques that require large detection volumes. The y-axis ('Absorption') in the spectrum is deduced using Equation 2.4, which differs from the 'absorption coefficient' (for the example given in Figure 5.2), details are discussed in the text.

For a precise study of the diamond absorption, diamond samples were measured with an integrating sphere in the range of 680-760 nm to gather all the transmitted light. This is different from the spectrum measurement in the whole UV-Vis range (200-800 nm), which was measured with the standard detector and the reflection was not taken into account when calculating the absorption A (Section 2.1.2, Equation 2.4). The absorption A is used to study the spectral features of the diamond, while measuring with the integrating sphere gives an absorption coefficient A_{coeff}

(also in cm^{-1}), which shows a more precise value of the diamond absorption for the strict comparison between samples. As a clarification, all UV-Vis spectra shown in this thesis are given as the absorption A, but all figures with the y-axis 'absorption coefficient' refer to A_{coeff}, and here the author explains the steps to obtain A_{coeff}:

In the spectrometer, the light beam has been collimated with a beam size larger than the sample, and a metal mask with a diameter of around 2.5 mm has covered the sample to ensure that only the light transmitted through the diamond sample can reach the sphere then collected by the detector. A dark-count calibration has been conducted with the empty mask (without the sample in the path, but still the same mask to ensure the same beam size). Diamond transmission at 680-750 nm and the theoretical value of the reflection are used to calculate the absorption coefficient in cm^{-1} (using a common logarithm base) as below:

$$A_{coeff} = -\frac{\log_{10}(\sqrt{4T_s^2 + (1 - 2R_t + R_t - T_s^2)^2} - 1 + 2R_t - R_t^2 + T_s^2)}{2dT_s} \tag{5.1}$$

where T_s is the measured transmission by integrating sphere, $R_t \approx 29.13\%$ is the theoretical value of the reflection, and d is the sample thickness. Derivation details of the absorption coefficient are introduced in [150]. In the following sections, one should be aware of the y-axis of the absorption figures, i.e. 'Absorption' refers to A given by Equation 2.4, while 'Absorption coefficient' refers to A_{coeff} given by Equation 5.1.

5.1.1 Cause of the absorption at 700 nm

From Figure 5.1 we can see that the three typical bands of the CVD diamond have no direct contribution to the wavelength at 700 nm. Nevertheless, other defects can have an absorption band in this region, here the author lists four possible candidates for nitrogen-doped diamonds.

The first is the H2 center (NVN^-), which has a ZPL at 986.3 nm and a very broad side band from ~600 nm to the ZPL. In some of the in-house grown high nitrogen samples, a large increase in the absorption at 650-800 nm were observed (e.g. some spectra in Figure 2.4). Due to the fact that the spectrum was only measured up to 800 nm, it is insufficient to the verdict that this increase is caused by the H2 center (without observing its ZPL). However, the smoothly increased feature without any sharp peak accords with the H2 side band, making the H2 center a very probable

candidate. The H2 center often appears during the creation of NV centers and it is also formed form the P1 center. It can be formed under similar conditions with the NV center and stable until 2100°C [107, 151]. In comparison the NV center starts to dissociate largely above 1200°C (Section 4.2). This brings difficulties to prevent the formation of H2 centers while pursuing high NV concentrations. Further investigation of its formation helps to achieve good combinations of high NV concentrations and low absorption at 700 nm.

The second candidate is a band centered at 730 nm, which is always present together with 520, 552 and 840 nm bands, but not correlated perfectly in intensity [107]. This band has been observed in high-nitrogen, high-hydrogen diamonds, however its origin has not been well defined. In our CVD samples such features were not found.

The third one is mostly seen in HPHT diamonds but not in CVD diamonds, it is a band centered at 710 nm associated with the vibronic side-band of the 794 nm nickel-related center [152]. With a high-temperature annealing at >1600°C, this band becomes more significant [107]. This band does not appear in our CVD diamonds as well.

The last one, which is often shown in irradiated diamonds, is the GR1 center (V^0). As discussed in Section 4.4, the GR1 center has a ZPL at 741 nm and a broad feature from ∼500 to 750 nm [107]. It is normally generated by high fluence/energy irradiation, although a high nitrogen concentration can promote the conversion from GR1 to ND1 (V^-) [107, 148]. Figure 4.6 has clearly shown that a high irradiation fluence (3E18 e/cm^2) can create a remarkable GR1 band for samples with 2.2 ppm P1, even with low electron energy (1MeV). In this regard, preventing over-irradiation and optimizing irradiation conditions are of great importance, not only for the NV charge state stability (Section 4.3), but also in order to avoid the GR1-induced extra absorption at 700 nm.

Apart from the point defect, non-diamond inclusions in the sample can have an even larger influence on the absorption. For instance, carbon nanoclusters contribute to very high absorption in the whole UV-Vis range, also resulting in a grayish coloration of the diamond [153]. The 'ramp' of the spectrum, which has been discussed in Section 2.1.2, also acts as a potential contributor to the absorption in the whole UV-Vis range.

5.1.2 Absorption coefficient of as-grown diamonds

This section investigates CVD diamonds with different nitrogen doping levels to learn the correlation between the P1- or NV-concentration and the absorption at 700 nm (Figure 5.2).

When varying only the N/C ratio during the growth, the absorption coefficient shows a super-linear correlation with the as-grown P1 concentration (Nitrogen series #1 and #2 in Figure 5.2(a), more discussion about the growth conditions see Section 3.2 and Appendix A). The super-linear fit in this figure was obtained with the two nitrogen series (the 'Snapshot series' was not included when fitting the data). For a larger amount of samples, which have different growth conditions but were all grown in the same reactor, their absorption also shows a super-linear correlation with the as-grown NV^- concentration (Figure 5.2(b), 'As-grown samples', be aware of the logarithmic scale in the y-axis). The fit in this figure was obtained with all the 'As-grown samples' (the 'Snapshot series' was again not included when fitting the data).

However, in earlier sections, the spectrum of our samples (Figure 2.4) shows that the extremely high absorption for higher nitrogen samples is not directly caused by P1 centers or NV centers. The P1 band, i.e. the 270 nm band, has a small bandwidth and no effect on 700 nm. The NV band (approximately from 400-700 nm) is very weak for all as-grown samples (with NV concentrations under the hundred ppb level), it also has negligible contribution to the absorption. The spectrum fitting (also see Figure 2.4) indicates two main factors that are accountable for the high absorption coefficient at 700 nm: one is the absorption increase at 650-800 nm, and the other is the fitting coefficient for the 'EL-offset', i.e. the offset for the whole spectrum without any specific band.

The increase in 650-800 nm is more significant for higher P1 concentrations. This supports the assumption that the feature is part of the side band of the H2 center (Section 5.1.1): the H2 center is also formed from the P1 center under similar conditions to the NV center, and its as-grown concentration can also show similar behavior as the NV center (Section 3.2), meaning a positive correlation between the as-grown H2 and P1 concentration. This assumption still needs further verification by measuring the spectrum in higher wavelengths to search for the H2 ZPL.

The offset of the whole spectrum is hardly connected to a single type of defect, it has a larger possibility to link to the diamond crystal quality. As the high nitrogen

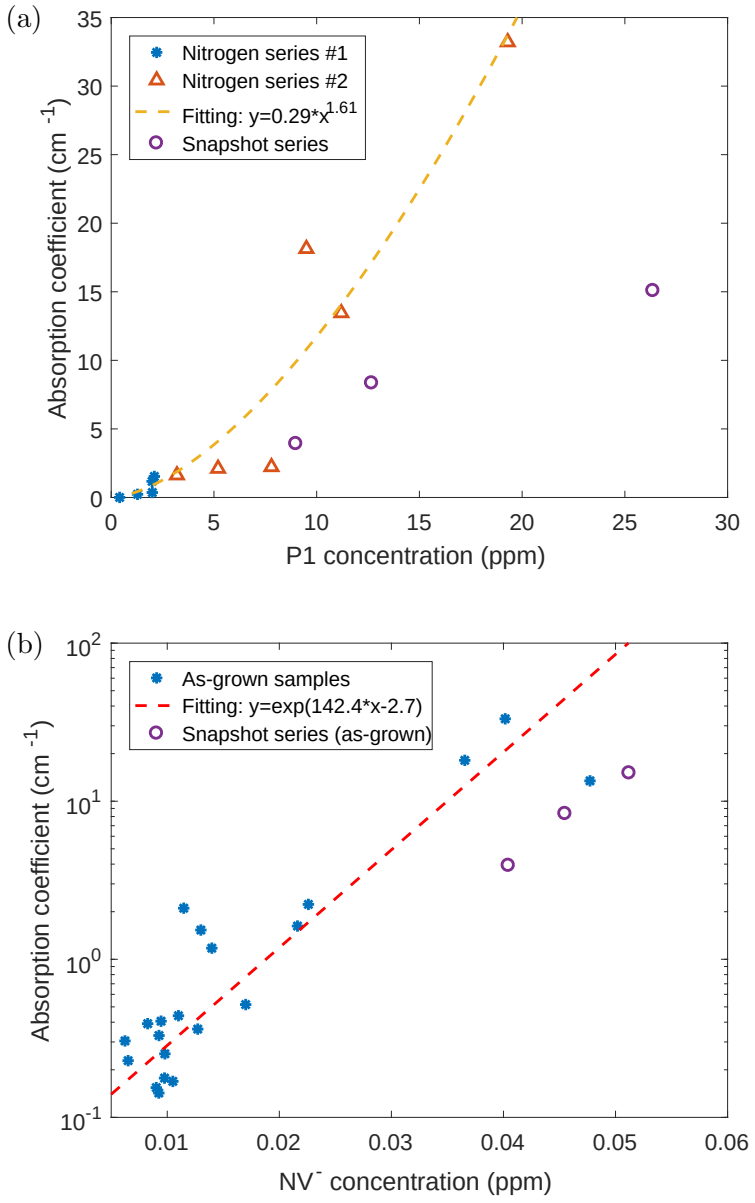

Figure 5.2: As-grown absorption coefficients (A_{coeff}, determination see Equation 5.1) at 700 nm for different (a) P1 concentrations, and (b) NV concentrations. The fits in the two plots were obtained with the two nitrogen series and the 'As-grown samples' respectively (the 'Snapshot series' was not included when fitting the data), the fits show a super-linear correlation between the absorption coefficient and the P1 or NV concentration. The 'Snapshot series' shows the optimized growth protocols that decrease the absorption for the same P1 or NV concentration.

samples (Nitrogen series #2) show dark, grayish color, the best explanation can be non-diamond carbon inclusions, which have been discussed in [153]. This also needs

further verification by the Raman spectrum. If it is the true explanation, then this high absorption for high nitrogen samples is more likely a fundamental issue in the nitrogen-doped CVD growth. Nevertheless, it also means that the appearance of the large spectral offset can be potentially reduced by the high-temperature annealing, especially the HPHT annealing, which can transform the carbon back into the diamond. The high-temperature treatment will be discussed in the next section.

To reduce the absorption during the growth, individual changes in growth parameters were applied for tests. Different oxygen or methane flow, total gas flow, pressure, holder geometry, etc. have been tried in order to understand their influences. These experiments were planned and conducted by Julia Langer and discussed in detail in [137]. A simplified conclusion is that reducing the absorption requires a localized optimization of the growth parameters for each P1 concentration. This means for different P1 concentrations, very different growth 'recipes' can be needed for an optimized crystal quality. Simply changing the N/C ratio does not lead to a constant crystal quality with only varying concentrations of nitrogen-related defects. The 'Snapshot series' in Figure 5.2 shows improved growth protocols, with a reduced absorption for the same P1- and NV level as the Nitrogen series #2. Adjustments in the oxygen or the methane flow have a relatively significant influence on reducing the absorption.

5.1.3 Absorption changes by irradiation and annealing

To acquire a high NV concentration, e-beam irradiation and subsequent annealing (at 1000°C) steps were conducted (Chapter 4). To achieve a good combination of high NV concentrations and low absorption, the influence of the after-growth treatments plays an important role. Section 4.4 discusses the absorption spectrum of the irradiation series and discussed the defect transformation during irradiation and annealing steps. The spectrum also shows how the absorption changes by the treatments. In this section, these spectra are re-arranged for single irradiation fluences, in order to directly compare absorption changes after each step (Figure 5.3).

For low irradiation fluences, the irradiation and the low-temperature annealing do not affect the absorption at 700 nm (Figure 5.3(a)). The irradiation does not create any defect with an absorption band in this regime, and the newly created NV band after annealing has a 'tail' that hardly extends to 700 nm. The absorption coefficient of interest stays consistent after the treatment.

In contrast, for high irradiation fluences, Figure 5.3(b), the creation of GR1 centers can significantly increase the absorption at 700 nm, as its absorption band covers a broad range from around 500 to 750 nm. The annealing treatment converts GR1 centers partially into NV^0 centers, leading to a decrease in absorption. However, GR1 centers are not fully converted, their remaining part still results in a higher absorption than the as-grown phase. This provides another reason why over-irradiation is harmful to the diamond quality, that the absorption coefficient thus the optical loss in the material is increased by such treatment conditions. As a review, the other reason (which was discussed earlier in Chapter 4) was that over-irradiation creates more NV^0 thus deteriorating the NV charge state stability and the ODMR contrast.

The annealing can compensate for the detriment of the over-irradiation to some extent, only in the sense of pulling down the absorption at 700 nm, at the cost of promoting the creation of NV^0. Consequently, one should avoid over-irradiating the diamond, an optimized irradiation condition is of great importance to acquire high-quality diamonds with high NV concentrations.

Nevertheless, the influence of the after-growth treatment is in general much less than the synthesis process. As shown in Figure 5.2 earlier, the different nitrogen doping levels can cause orders of magnitude increases in the absorption, if no localized optimization of the growth protocol has been applied. The appearance of GR1 centers by over-irradiation can never make a such high impact on the absorption changes. The most important role of the treatment is to achieve an improved combination of high NV concentrations and low absorption. Figure 5.4 shows how the treatment improves their combinations. After the treatment, the data points move towards higher NV^- with relatively consistent absorption coefficients. The different degree of the NV enhancement is due to varying irradiation fluences. The result shows that a good combination (NV^- >0.2 ppm with an absorption coefficient of $\sim$0.15 cm^{-1}) can be achieved by an optimized treatment. The author also points out that these results come from CVD diamonds with P1$\leq$3 ppm, for higher nitrogen samples the creation of the H2 center might have to be taken into account, which needs further investigations.

Further improvements can be approached in mainly three directions: the first is to further enhance the P1 to NV^- conversion rate, while remaining a high NV^-/NV ratio (this thesis shows an optimization in Chapter 4, while further improvement is possible with additional treatments); the second is to further optimize the growth protocol; the final one is to apply pre-treatments before the irradiation to reduce

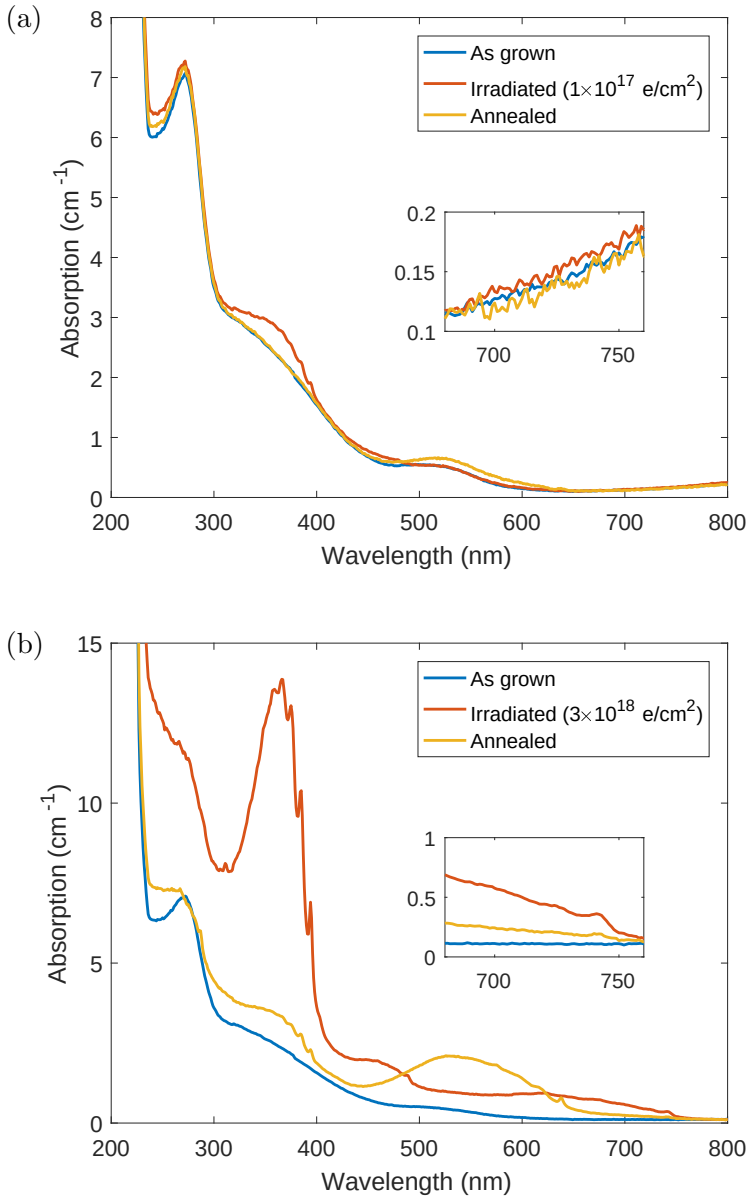

Figure 5.3: UV-Vis absorption (A, determination see Equation 2.4) spectrum respectively after growth, irradiation, and annealing steps for (a) 1×10^{17} e/cm^2 and (b) 3×10^{18} e/cm^2 irradiation fluence (both with 1 MeV electron energy). The annealing step was conducted with 1000°C for 2 h.

the absorption. Specifically, HT annealing is a promising candidate, which is known to be used for jewelry diamonds to obtain fancy colors [154]. The HT annealing has huge impact on the defect formation and the crystal structure, it can potentially help to reduce the absorption at 700 nm with proper treatment parameters. More details about it will be discussed in the next section.

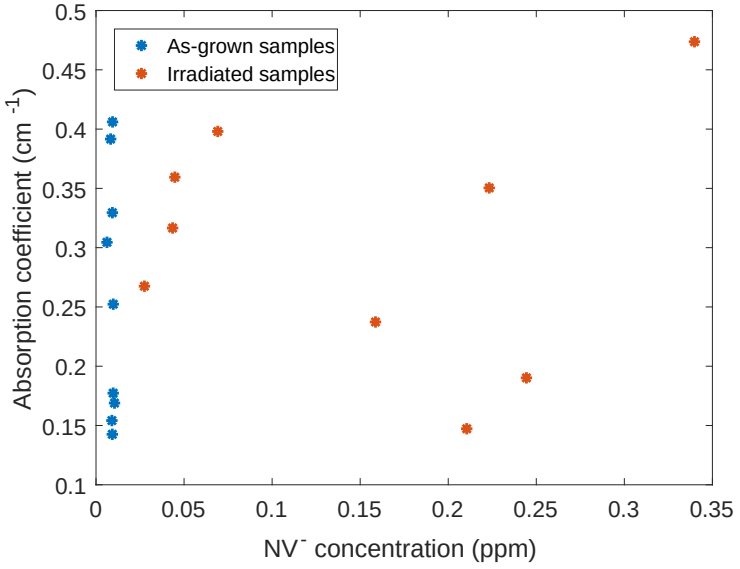

Figure 5.4: Irradiation and annealing steps enhance the NV concentration, while having minor influences on the absorption. The 'Absorption coefficient' on y-axis is given as A_{coeff} in Equation 5.1 (differs from A in Equation 2.4, details see text in Section 5.1).

5.2 High-temperature annealing for diamond absorption

High temperature (HT) annealing is commonly used to engineer the defect transformation and crystal quality of diamonds [155, 156, 151, 154, 157]. To further reduce the absorption at 700 nm of our CVD diamonds, this section tests both low pressure, high temperature (LPHT) and high pressure, high temperature (HPHT) annealing. The HT annealing step is conducted after growth before irradiation, since such a high annealing temperature (>1500°C) anneals out the NV center, which contradicts the goal of high NV concentrations.

Figure 5.5 shows the diamond-graphite equilibrium line [158, 159] and the operation regime of HPHT and LPHT annealing. Above the equilibrium line, graphite transforms into the diamond phase. Both LPHT and HPHT annealing were performed at temperatures of 1500-2500°C, LPHT annealing is conducted in the graphite regime (with low pressures), while HPHT annealing is conducted around the equilibrium line. This makes differences between the annealed diamonds in terms of structural integrity and graphitization. In [160] it has been pointed out that the behavior of major nitrogen-related defects at annealing temperatures below 1900°C does not

depend significantly on pressure. The two methods create the same nitrogen-related defects qualitatively, but the concentrations of these defects are varied substantially.

The author's interest in the two methods centers on two aspects: Firstly, how do they influence the absorption coefficient at 700 nm, and are they proper methods to reduce the absorption? Secondly, can most of the P1 centers survive during the annealing? As the P1 center is the key prerequisite for NV formation, the sacrifice in its concentration is unfavorable.

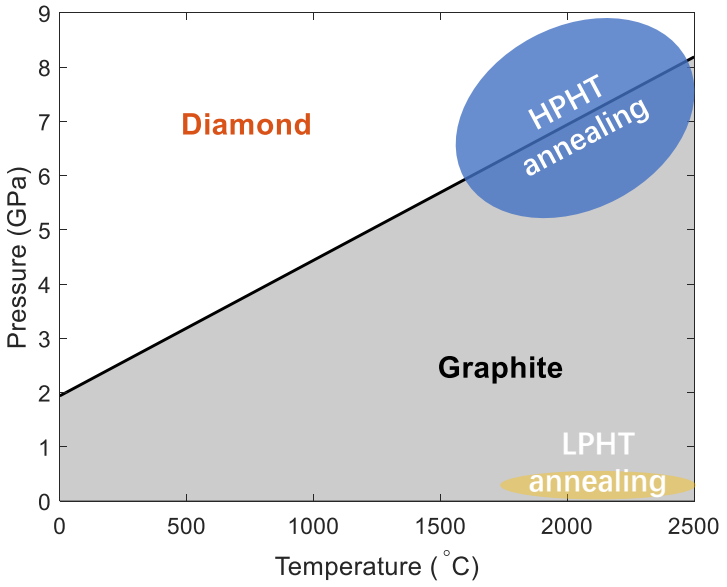

Figure 5.5: Diamond-graphite equilibrium line [158, 159] and the operation regime of HPHT and LPHT annealing.

The transition between single nitrogen atoms (P1, N_s^0 or C centers) and nitrogen aggregations during HT annealing depends largely on their initial concentrations. For instance, type Ib diamonds have large nitrogen content with C centers more than nitrogen aggregations. For this type of diamond, C centers start to aggregate and form A centers (a pair of nitrogen atoms) at 1500°C for initial nitrogen content >500 ppm, or at 1700°C for nitrogen content <500 ppm [107]. B centers (a carbon vacancy surrounded by four nitrogen atoms) and other three- or four-atom complexes only begin to form >2200°C. In contrast, type Ia and IIa diamonds contain mainly nitrogen aggregations rather than isolated nitrogen atoms. For these types of diamonds, it has been observed that the HPHT annealing at 1950-2300°C can promote the dissociation of the A center into C center [161, 162]. It appears that if P1 centers are dominant in the diamond (type Ib), the HT annealing has a high probability to aggregate them into A centers; on the contrary, if nitrogen aggregations

are dominant (type Ia or IIa), the HT annealing in certain conditions can enhance the creation of P1 centers. This equilibrium depends on initial concentrations and the treatment conditions (T, P, duration). In this sense, it is difficult to predict the changes of P1 centers by HT annealing for CVD diamonds with nitrogen content <50 ppm. Followed subsections show experimental results to discuss the influence of LPHT and HPHT annealing on CVD diamonds, in terms of absorption and P1 concentration changes.

5.2.1 LPHT annealing

LPHT annealing was performed on two CVD samples at 1800°C in vacuum for 10 min. The samples were grown under the same conditions, resulting in a P1 concentration of ∼5.5 ppm (P1 concentrations were determined from the UV-Vis spectrum, method see Section 2.1.2). Their spectra show very similar features, here Figure 5.6 showa one of those samples, which is representative, to discuss the changes by LPHT annealing.

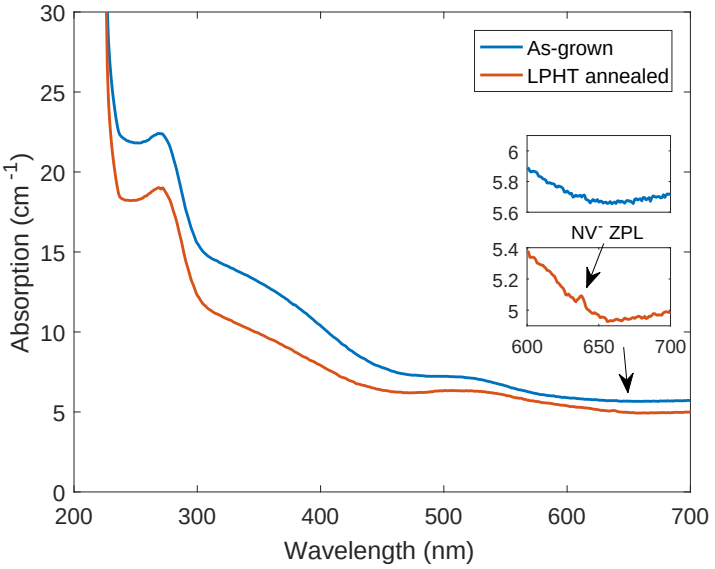

Figure 5.6: UV-Vis absorption (A, determination see Equation 2.4) spectrum before/after LPHT treatment. The absorption is reduced over the whole wavelength range (200-800 nm) after LPHT treatment.

After annealing, the absorption reduces in the whole UV-Vis range, although the reduction at 700 nm is not very significant. Unexpectedly, a clearer NV^- ZPL appears after annealing, although NV centers should be annealed out under such a

high temperature. A possible explanation is that NV centers are formed during the cool-down stage of the annealing. Unfortunately, since the temperature-time profile was not precisely recorded, this assumption can not be further verified. The P1 band (270 nm) looks also reduced in Figure 5.6, however, as other spectral components change as well, they can mask the real behavior of the P1 band. In this regard, the fitting method introduced in Section 2.1.2 greatly helps to analyze the spectrum to understand the changes in each component.

Figure 5.7 shows the fitting details for the spectrum in Figure 5.6. Comparing the extracted P1 band ('270 nm band', red), it is found that the P1 concentration stays consistent after annealing. It might be an indication that nitrogen already aggregated during the CVD growth, therefore a balance between the single nitrogen atoms and nitrogen aggregations was not broken by the LPHT annealing. However, this was not verified by the FTIR measurements due to the low sensitivity of the setup (the method to determine A- and B-centers by FTIR see Section 2.3). Further experiments are needed to investigate the concentration of nitrogen aggregations, which gives a better understanding of the equilibrium between nitrogen aggregation and single nitrogen during LPHT annealing. It is worth noting the reduction of both the 'ramp' and the 360 nm band, which both link to vacancy clusters [113]. The reduction of these two features indicates the dissociation of vacancy clusters, as their dissociation starts to be significant above 1500°C (the sample was annealed at 1800°C). The offset ('EL-offset') of the spectrum has only a small change, which appears to be the cause of the reduction of the absorption at 700 nm.

To conclude, the result shows that LPHT annealing can slightly reduce the absorption coefficient at 700 nm for CVD diamonds, while not changing the P1 concentration. The same treatment was conducted on HPHT diamonds and found a more significant influence on their absorption at 700 nm. From this, good combinations of high NV concentrations and extremely low absorption in HPHT diamond were achieved, which provides great advantages for advanced techniques requiring large sensing volumes. Further studies of LPHT treatments on HPHT diamonds with different atmospheres and duration, as well as subsequent irradiation are discussed in [150].

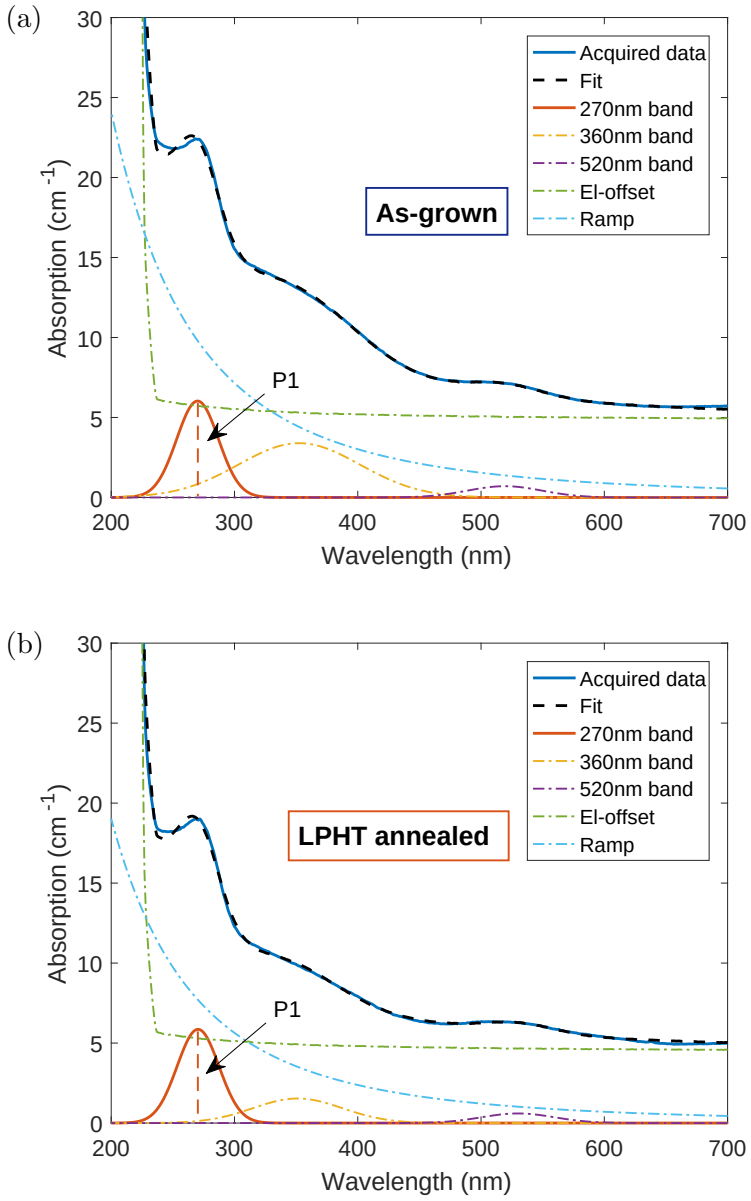

Figure 5.7: Extracting the 270 nm absorption band to calculate the P1 concentration before and after LPHT annealing (method see Section 2.1.2). The P1 concentration keeps consistent, while the 'ramp' and the 365 band show a significant reduction. The 'Absorption' on the y-axis is given as A in Equation 2.4.

5.2.2 HPHT annealing

For HPHT annealing, a CVD diamond with ∼10 ppm P1 centers has been grown (P1 concentrations were determined from the UV-Vis spectrum, method see Section 2.1.2). The annealing was conducted with 1850°C, 5-6 GPa for 10 min by an

external partner.

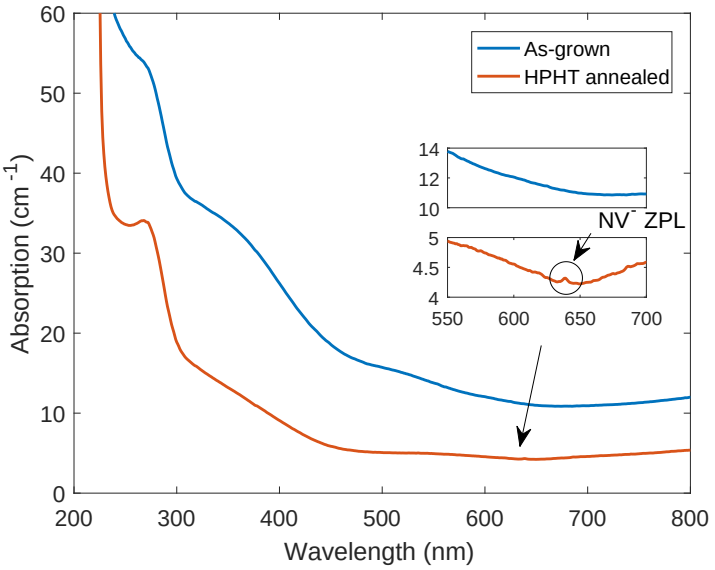

Figure 5.8: UV-Vis absorption (A, Equation 2.4) spectrum before/after HPHT treatment. The absorption coefficient is reduced over the whole wavelength range (200-800 nm) after HPHT treatment, while the spectral feature shows significant differences.

Figure 5.8 shows how the spectrum changes after annealing: HPHT annealing reduces the absorption in the whole UV-Vis range remarkably, which is more significant than the changes by LPHT annealing (Figure 5.6). A clear NV^- ZPL also appears after annealing (similar to LPHT), which can be created during the cool-down process.

The spectra were also fit to extract their components, Figure 5.9. The result shows that although the spectral features look very different after HPHT annealing, the P1 concentration stays consistent. The main changes lie in the 'ramp', the 360 nm band and the 'EL-offset'. The weakened 'ramp' and 360 nm band are similar to LPHT annealing, which is due to the dissociation of vacancy clusters. The 'EL-offset', noticeably, shows a large reduction after HPHT annealing. Its change acts as the main contributor to the significantly reduced absorption in the whole spectrum. This provides a piece of evidence for the earlier speculation in this thesis, that the high absorption (and grayish color) of the high nitrogen sample can originate from non-diamond carbon inclusions (Section 5.1). HPHT annealing conducted near the diamond-graphite equilibrium line has the chance to transform the inclusions into diamond, making the sample more transparent and reducing the absorption

coefficient.

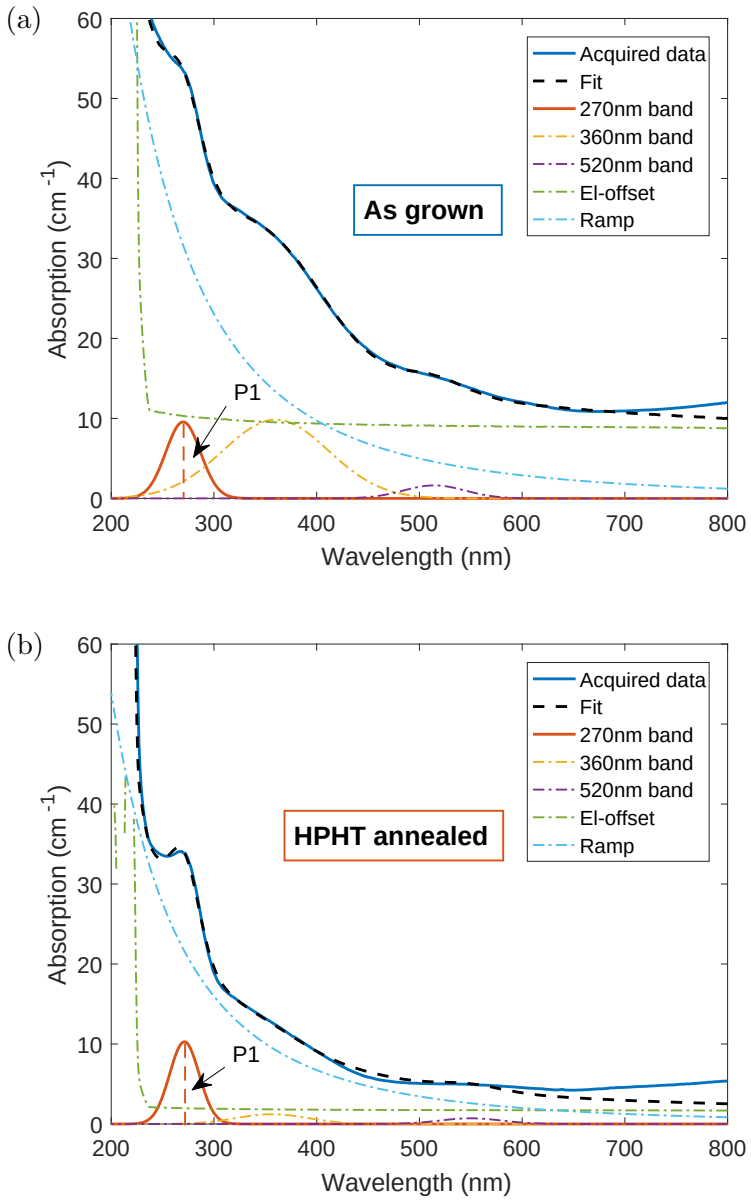

Figure 5.9: Extracting the 270 nm absorption band to calculate the P1 concentration before and after HPHT annealing (method see Section 2.1.2). The P1 concentration keeps consistent, while the offset ('EL-offset'), the 'ramp' and the 365 band show a significant reduction. For the HPHT treated spectrum, bad fitting occurs for >500 nm due to the existence of the NV band (around 480-650 nm) and a band covers 700-800 nm. The 'Absorption' on y-axis is given as A in Equation 2.4.

In conclusion, HPHT annealing is a powerful tool to improve the quality of high nitrogen CVD diamonds, in terms of reducing their high absorption while remaining

high P1 concentrations. LPHT annealing, in comparison, is less sufficient to reduce the large 'offset' of the absorption that is caused by carbon inclusions, but it shows a good performance in reducing absorption in HPHT diamonds. Both of them can be applied as standard treatment (before irradiation) for improved material. To that end, further investigation into treatment parameters is still needed.

Chapter 6

6 Birefringence study of nitrogen-doped diamonds

The diamond absorption and birefringence are the main contributors to the optical loss in material for applications that require large sensing volumes [150]: all optical readout suffers from absorption, advanced techniques such as multi-pass readout, optical cavity coupling or laser cavity sensing require specifically low absorption, and optical modes also suffer from birefringence in the material. Moreover, polarisation-selective addressing and readout of NV centers are also only possible without birefringence. Therefore, birefringence is a crucial property that largely influences diamond performance when it is applied as a sensing material. The nitrogen doping in diamonds arises the question of whether it induces an extra source of the birefringence, and how the birefringence behaves for different nitrogen doping levels and other growth conditions. When pursuing high NV^- concentrations for improved sensitivity (Chapter 4), the influence of the nitrogen content on birefringence also needs to be considered.

This chapter investigates birefringence in NV-doped diamonds and changes to birefringence during the NV creation process, and discusses the correlation between the birefringence and the nitrogen content in diamonds.

6.1 Birefringence measurement

Diamond is generally considered to be an isotropic crystal without or with weak birefringence. However, extended defects in diamonds such as dislocations gen-

erate strain fields that distort the diamond lattice [163]. This leads to localized birefringence patterns with randomly varying slow axes [164], which appear inhomogeneously in the crystal. Moreover, applied stress can also make the diamond structure anisotropic thus resulting in birefringence.

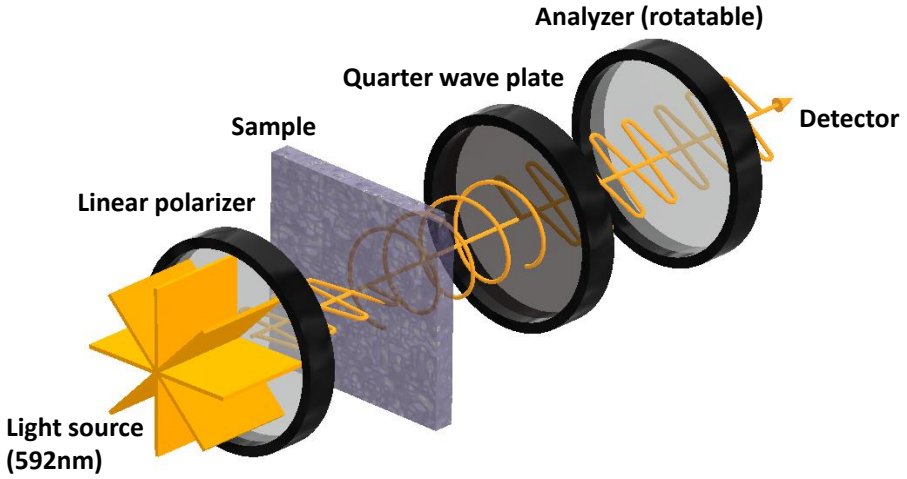

Figure 6.1: Schematic of Sénarmont principle for the birefringence measurement.

The birefringence in this thesis was measured with a commercially available polarimeter (Ilis StrainScope Flex), using the Sénarmont principle, as shown in Figure 6.1. A single wavelength light source (592 nm) gets linearly polarized (by a polarizer), then transmits through the birefringent sample and becomes elliptically (or circularly) polarized. A quarter wave plate ($\lambda/4$ plate) placed behind the sample (and oriented along the same axis as the initial polarizer) then converts the elliptically polarized light back into linearly polarized light. Finally, by rotating the analyzer behind the $\lambda/4$ plate, the shift in the polarisation angle α_r relative to the original polarisation before the sample can be measured. Form the polarization angle α_r, the optical retardation R (the phase difference between the two axes with different refractive indexes) can be deduced using the relation:

$$R = \alpha_r \cdot \lambda/180° \tag{6.1}$$

where λ is the wavelength, in our case it is 592 nm. Be aware that using this method, only the projection of the birefringent axes into the surface plane of the sample (i.e. orthogonal to the beam direction) is measured. By repeating this measurement with the polarizer and quarter wave plate rotated at multiple angles, the local direction of the slow and fast axis, i.e. the two directions with different refractive indices can be determined as a spatial map as well.

The birefringence Δn is given by:

$$\Delta n = R/d \tag{6.2}$$

where d is the thickness of the sample. Be aware that this measurement can resolve the birefringence with retardation and axis orientation locally in the x-y plane of the sample, it can not resolve the birefringence changes along the depth of the sample, Equation 6.2 is only valid by assuming the birefringence along the incident beam is homogeneous, which can be assumed for samples with a small thickness along the z direction, i.e. thin diamond plates.

A spatially resolved map of the retardation (R) is measured for the diamond. Ideally, a precise birefringence (Δn) map can be calculated from it, with a thickness profile for each pixel. However, such a thickness profile is difficult to obtain. Considering that our samples are well polished (Ra<0.5 nm) on both sides, and the miscut angle was controlled to be small, this thesis uses the average thickness of the sample to calculate the birefringence map.

6.2 Birefringence of as-grown diamonds

Figure 6.2(a) and (b) show respectively the birefringence map of a 3×3 sample and its bright-field image. Normally our samples have higher birefringence on edges, which can be created by the laser cutting process (to cut out the poly-crystalline edges of the sample). The diamond center is more homogeneous, however, small twists often appear, which have been suggested to be caused by dislocations [164]. The birefringence and its homogeneity in the sample center are the most relevant for lasing applications, here this section investigates their correlation with different growth parameters.

Several CVD series have been grown under different conditions (all in (100) orientation), and calculate their average Δn after growth in the center area (2.5×2.5 mm), Figure 6.3. Overall, the birefringence does not show a correlation with the thickness, indicating the formation of extended defects is not influenced much by the growth duration. The data points of 'Protocol 'NDT-12" (blue cross) provide further evidence. These samples were grown with the same parameters as the 'NDT-12' in Nitrogen series #1, (Table A.1) but different duration, leading to different thicknesses. This protocol was chosen to conduct repetitive growth for its intermediate nitrogen con-

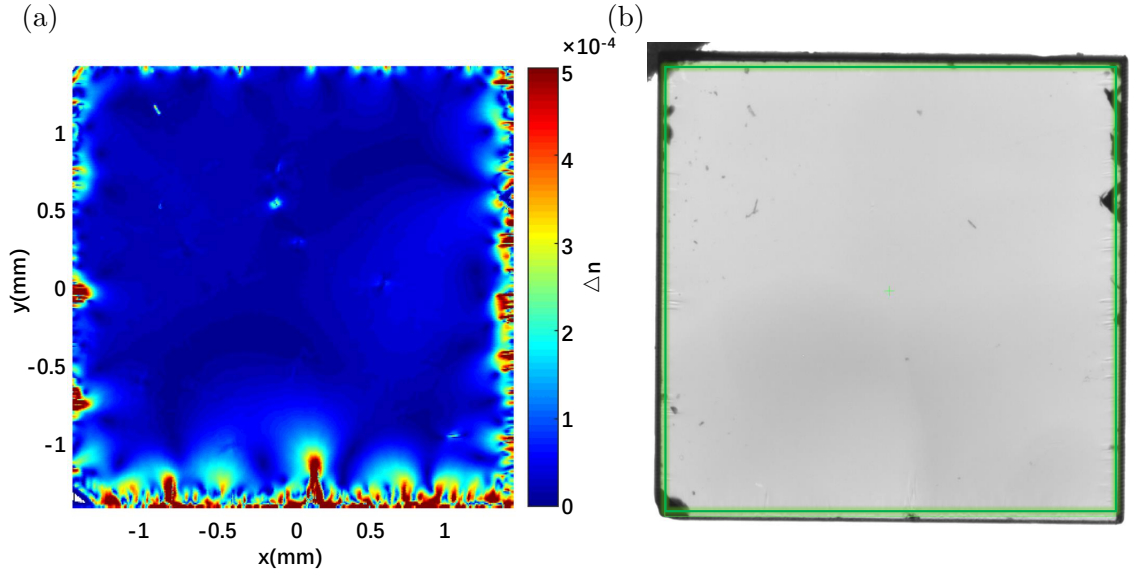

Figure 6.2: (a) The birefringence (Δn) map of a 3×3 mm sample and (b) its correlated bright-field image (the green box shows the measured region of (a)).

centration (∼2.6 ppm) and stable crystal quality. The birefringence of these samples is very similar for different thicknesses (500 μm or 850-900 μm). An expected deterioration with continued growth did not occur - so thicker samples can be grown without compromising crystal quality and without birefringence/strain propagating from the edges into the sample. This is a good sign for sensing applications that benefit from thick crystals and large sensing volumes.

When changing the growth pressure ('Pressure series', orange square), no remarkable difference in birefringence has been observed, however, more data points are needed to draw a conclusion. By changing the geometry of the holder ('Holder series', yellow triangle), one can reduce the average birefringence and improve its homogeneity. More details of the influence of the holder are discussed in [138].

Figure 6.3 shows that most of the changing parameters did not lead to a huge difference in the diamond birefringence, except for changing the nitrogen content (see 'Nitrogen series #2' on the plot, green stars in the gray region). The green data points show a large variation in the birefringence, covering a broad range over two orders of magnitude. This series, as well as the 'Nitrogen series #1' (purple asterisk) were introduced in previous chapters, they were grown with varying N/C ratios, resulting in a P1 concentration of 0.2-2.6 ppm for the series #1 and 3.2-19.3 ppm for the series #2 (Table 3.1). Nitrogen series #2 contains a broader range of the P1 concentration than the series #1, and also shows a much more significant

variation in the birefringence. It is reasonable to assume that the birefringence links to the nitrogen doping level during the growth.

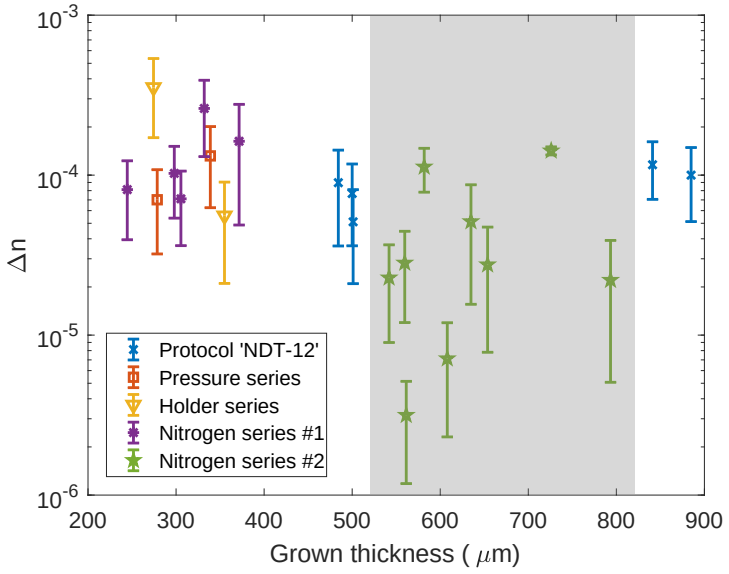

Figure 6.3: The birefringence of different growth series (after growth). The result has no significant correlation with the growth thickness. When changing different growth conditions, the nitrogen concentration shows a strong influence on the birefringence (Nitrogen series #2 in the gray region).

To figure out how the nitrogen content influences the birefringence, the average Δn and its standard deviation are plotted as a function of the P1 concentration (Figure 6.4). Surprisingly, both Δn and its standard deviation decrease with higher P1 concentrations, meaning that a higher incorporation level of P1 centers links to a lower and more homogeneous birefringence. For samples with the highest P1 concentrations, the Δn drops below 10^{-5}, which has been defined as the standard of 'ultra low' birefringence for diamond material [165]. A hypothesis to explain the correlation between low birefringence and high nitrogen content can be that nitrogen atoms help to prevent the formation of extended defects during growth. While the incorporation of a dopant like the nitrogen atom could be assumed to induce stress in the lattice due to different atom sizes, it might be the case that the substitutional nitrogen actually can help to release local stress in the growth caused by other defects. However, both a theoretical model and more experimental investigations are needed to have a deeper insight into this effect. It is noticed that the absorption coefficient of the two nitrogen series increases with the P1 concentration (Section 5.1.2). According to the discussion in the section, the increased absorption is mainly contributed by the 'offset', which can originate from the non-diamond

carbon inclusions. If this explanation is correct, it is difficult to conclude whether the low birefringence for high P1 concentrations is caused by the nitrogen atoms or by the inclusions, as they show a positive correlation to each other. The next section further studies the effect of after-growth treatments on the birefringence, which can potentially provide more clues to this question. To conclude, the birefringence reduces with increasing nitrogen doping in the CVD growth, which has not been reported by previous studies, and it can benefit the high nitrogen-doping growth.

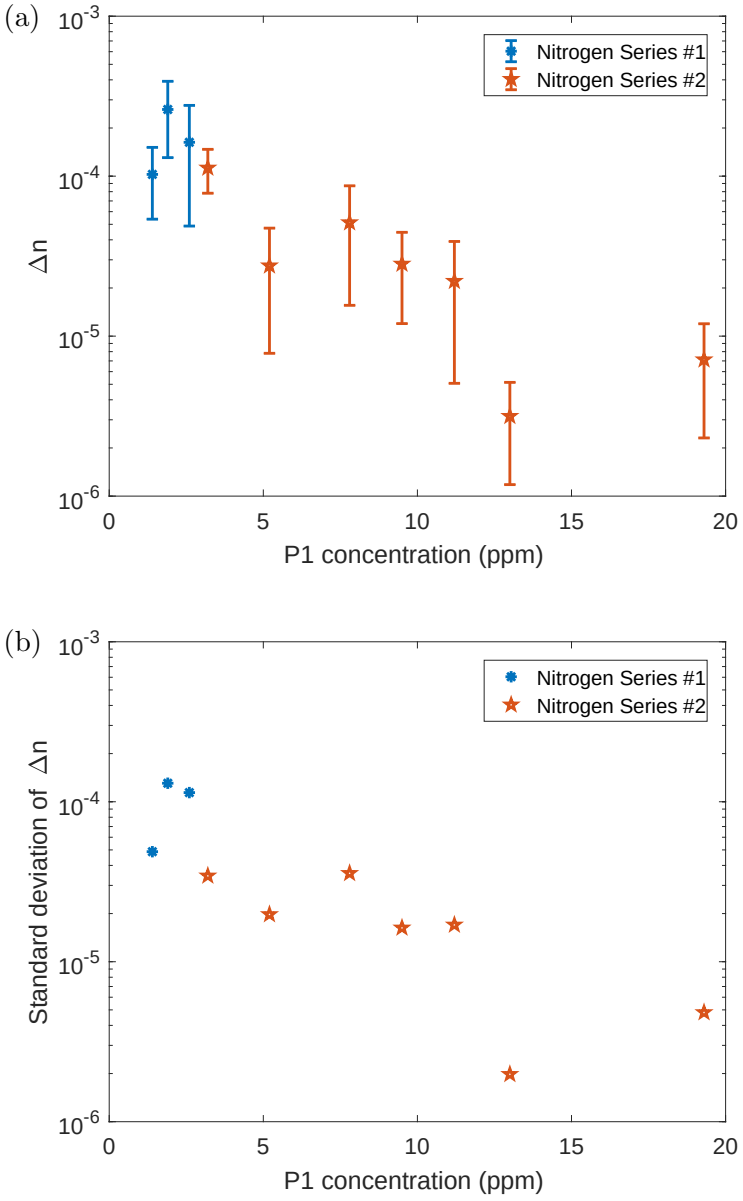

Figure 6.4: The birefringence Δn and its standard deviation decrease for higher P1 concentrations.

6.3 Birefringence changes via after-growth treatments

After growth, the diamond is often treated to enhance the NV concentration or for improved properties. This section studies both CVD and HPHT diamonds to discuss how these treatments affect the birefringence. Specifically, the influence of e-beam irradiation and the subsequent annealing is discussed, as well as the influence of high-temperature treatments (LPHT and HPHT annealing).

6.3.1 Electron-beam irradiation and subsequent annealing

To create more NV centers and thus achieve enough gain for the lasing, e-beam irradiation and annealing were conducted on both CVD and HPHT diamonds (Chapter 4). Figure 6.5 shows the birefringence (Δn) map for three samples before (left) and after (right) irradiation. Figure 6.5(a) and (b) show respectively two CVD diamonds with P1$\sim$10 ppm, they were both irradiated with 1 MeV energy and a fluence of 3×10^{18} e/cm^2. After irradiation, no significant change in the map can be observed for these samples, and their average birefringence stays consistent. Figure 6.5(c) shows an HPHT diamond with P1>20 ppm, which was irradiated with 2 MeV and 1×10^{18} e/cm^2. For this sample very slight changes were found in the birefringence map after irradiation, however, some regions have increased birefringence, while some others have decreased ones, two such regions are marked in the figure (white circles) as an example. The changes do not show a uniform trend. A possible explanation is that the irradiation under the conditions causes surface damages, which slightly changes the birefringence in a random way. It can be concluded that irradiation with high energy (1MeV) electrons and high dosage (3e18) does not affect the birefringence significantly. The overall changes introduced by irradiation are very small.

Furthermore, several HPHT samples were irradiated with 2 MeV, 1×10^{18} e/cm^2, followed by an annealing step at 1000°C for 2 h. Figure 6.6 shows three such samples as an example: (a) and (b) are thin diamond plates of around 250 μm, (c) is a thick plate of around 1300 μm. They all have a P1 concentration >20 ppm, after treatments their NV concentration increases from <1 ppb to >1 ppm level. All three samples show a decrease in the birefringence, while in (a) and (b) it is not as significant as in (c). As the irradiation has only weak (and random) influences on

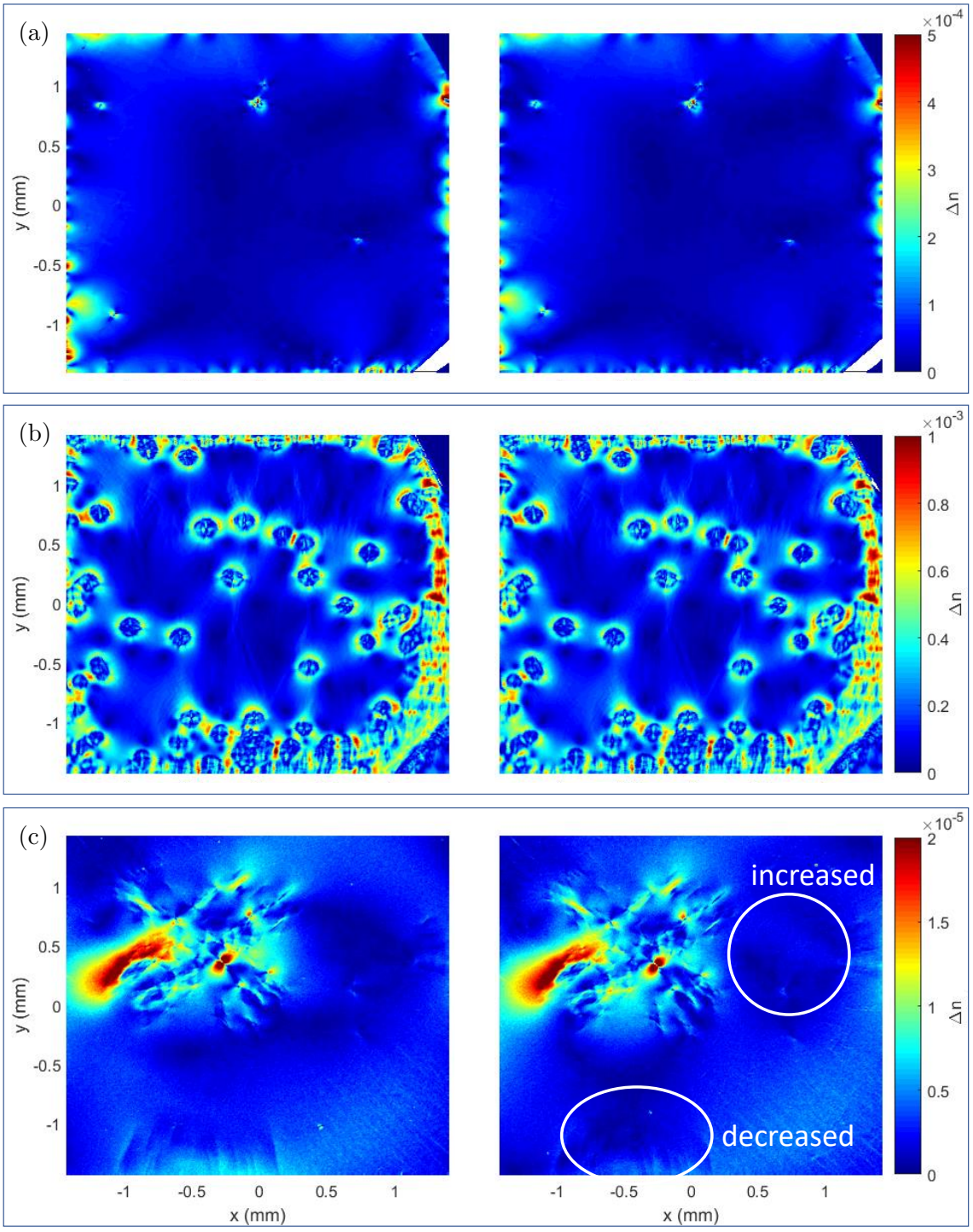

Figure 6.5: Birefringence before (left) and after (right) irradiation. (a), (b) CVD diamonds with P1∼10 ppm, irradiated with 1 MeV, 3×10^{18} e/cm^2. No significant change is observed after irradiation. (c) HPHT diamond with P1∼20 ppm, irradiated with 2 MeV, 1×10^{18} e/cm^2. Slight changes in some regions are observed, but without a uniform increasing/decreasing trend.

birefringence as shown in Figure 6.5 and discussed above, the decrease shown in the map is potentially mainly introduced by the annealing step. This decrease should not originate only from the surface changes, but also from the changes in the entire volume of the sample, as the thicker sample (Figure 6.6(c)) shows more reduction in the whole area than the thinner sample ((a) and (b)). A possible explanation is that vacancies and their positioning in energetically favorable positions (such as NV centers etc.) lead to a small release of local stress, which is similar to the assumption that more nitrogen-doping releases stress in the crystal (Figure 6.4). In this sense, irradiation and annealing steps can be considered as positive treatments to reduce birefringence, while largely enhancing the NV creation.

6.3.2 High-temperature treatment

In section 5.2 it was discussed that the high-temperature treatment (including LPHT and HPHT annealing) can reduce the diamond absorption, thus reducing the optical loss in the material. As high birefringence also contributes to optical loss, this section investigates the effect of high-temperature treatments on birefringence.

Figure 6.7 shows two HPHT samples before (left) and after (right) LPHT annealing at 1800°C for 48h in the H_2 atmosphere. LPHT annealing, which is operated in the graphite regime (Figure 5.5), has a high possibility to create cracks in the diamond [160]. Any crack will change the birefringence in a larger area, most of the time it will introduce a remarkable increase in the birefringence (Figure 6.7(a)). However, there were also samples found where no cracks occurred in the annealing. For those the birefringence stays relatively stable (Figure 6.7(b)). This is in contrast to the result shown in Figure 6.6, where annealing at 1000°C already reduced the birefringence. While one could expect that LPHT annealing with a much higher temperature leads to similar behavior, the results show that at such high temperatures, the possibility of crack formation is high with a very bad influence on the birefringence potentially in a large area, and in the case that cracks are avoided the birefringence appears constant. One possibility is that the low-pressure annealing itself does not influence the birefringence significantly (unless it creates cracks), but the defect transformation via irradiation plus annealing has the effect. However, by irradiation and subsequent annealing, the transformations mainly happened between point defects, this in principle should not have a large influence on the birefringence.

For HPHT annealing, Figure 6.8 shows two CVD samples. The samples were an-

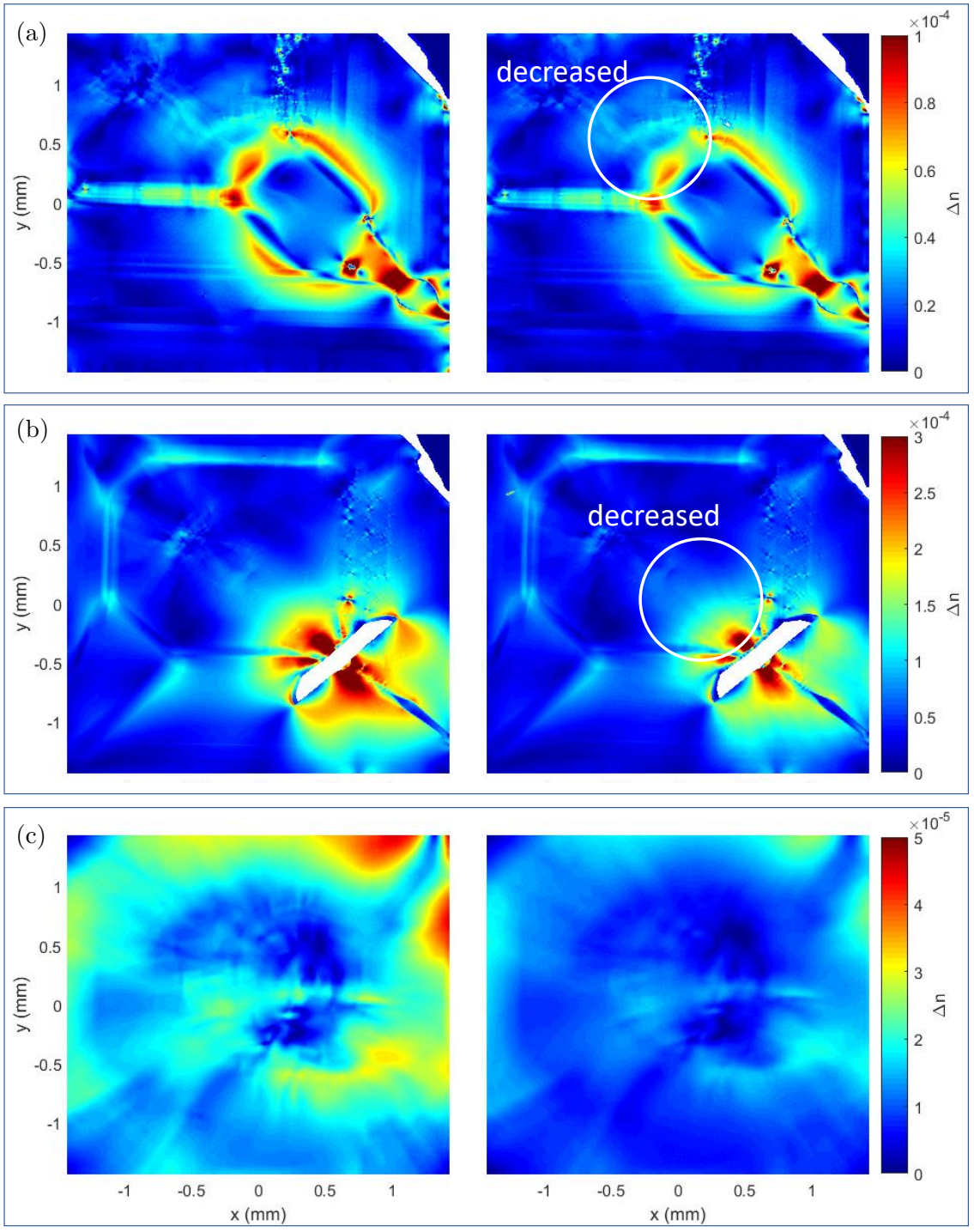

Figure 6.6: Birefringence before (left) and after (right) irradiation and annealing. All samples have the same irradiation and annealing conditions, i.e. they were irradiated with 2 MeV and 1×10^{18} e/cm^2, annealed at 1000°C for 2 h. (a), (b) Thin HPHT diamonds (∼250 μm). (c) Thick HPHT diamonds (∼1300 μm).

nealed at 1850°C, 5-6 GPa for 10 min. Although they have the same treatment conditions, they have different behavior after annealing. The sample in Figure 6.8(a) has a significantly reduced birefringence in the entire area after annealing, while the other sample in (b) does not show a significant decrease, but an increase in the top right corner along the edge of the sample 'notch'. This 'notch' was made by laser cutting to distinguish the sample surface, the result here shows that when it is cut to have a rough edge, it can induce additional birefringence during the annealing. In comparison, the sample in (a) has a well-cut 'notch' (with a smoother edge), the birefringence in this area did not increase after annealing, it simply followed the decreasing trend over the whole sample. Both the two samples show a lighter coloration after HPHT annealing, and their behaviors in the UV-Vis spectrum are also similar (decreased absorption in the whole range, with a stable P1 concentration).

Additionally, Section 6.4 showed that the birefringence decreases for higher nitrogen doping levels. The question is thereby raised, whether nitrogen atoms or non-diamond inclusions result in the birefringence decrease during the growth. HPHT treatment can anneal out a large amount of the inclusions in diamond (Section 5.2), but it either further reduces the birefringence, or shows weak influence only (Figure 6.8). In this regard, carbon inclusions in diamonds seem not to be the key reason for such a low birefringence in high-nitrogen samples.

To conclude, HPHT annealing can potentially decrease the birefringence in the overall crystal generally: even in the sample which cracked, Figure 6.8(b), a small amount of decrease appears on the opposite edge (for instance see the bottom left corner). The main issue that deteriorates the birefringence is the cracking, which is happened generally at such high temperatures (for both LPHT and HPHT annealing). Especially, the rough laser-cut surface/edge, or the existing crystal damage before annealing, show a higher potential to form cracks during the HT annealing treatment. In this regard, smooth and polished surfaces and edges are prerequisites to improve the HT annealing treatment, in the sense of reducing the birefringence - and this further improves the diamond quality for sensing applications.

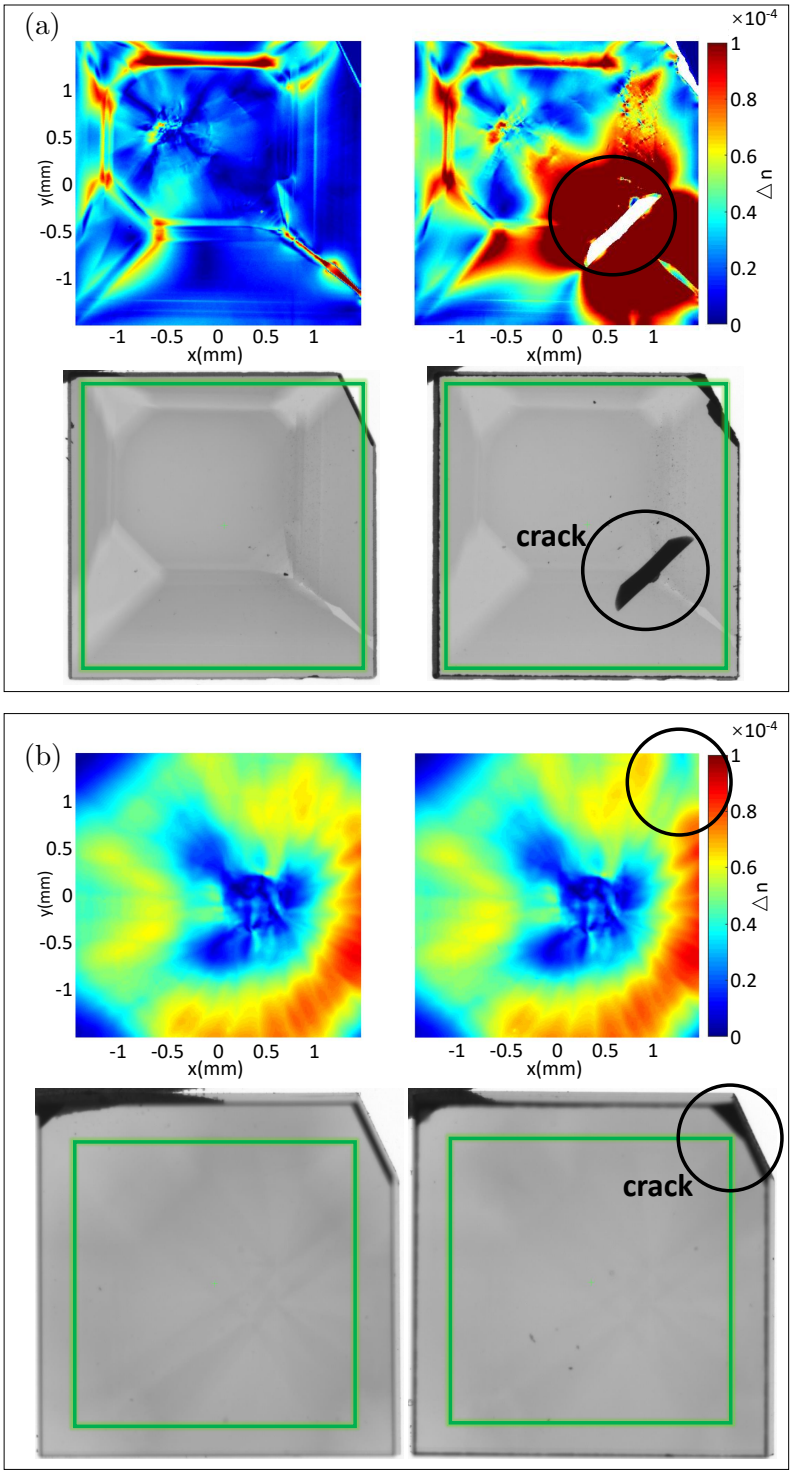

Figure 6.7: Birefringence before and after LPHT annealing for two HPHT diamonds. For both (a) and (b), upper: birefringence maps, lower: corresponding bright-field images (the birefringence was measured in the green block); left: before LPHT annealing, right: after LPHT annealing. LPHT annealing creates cracks that significantly influence the birefringence.

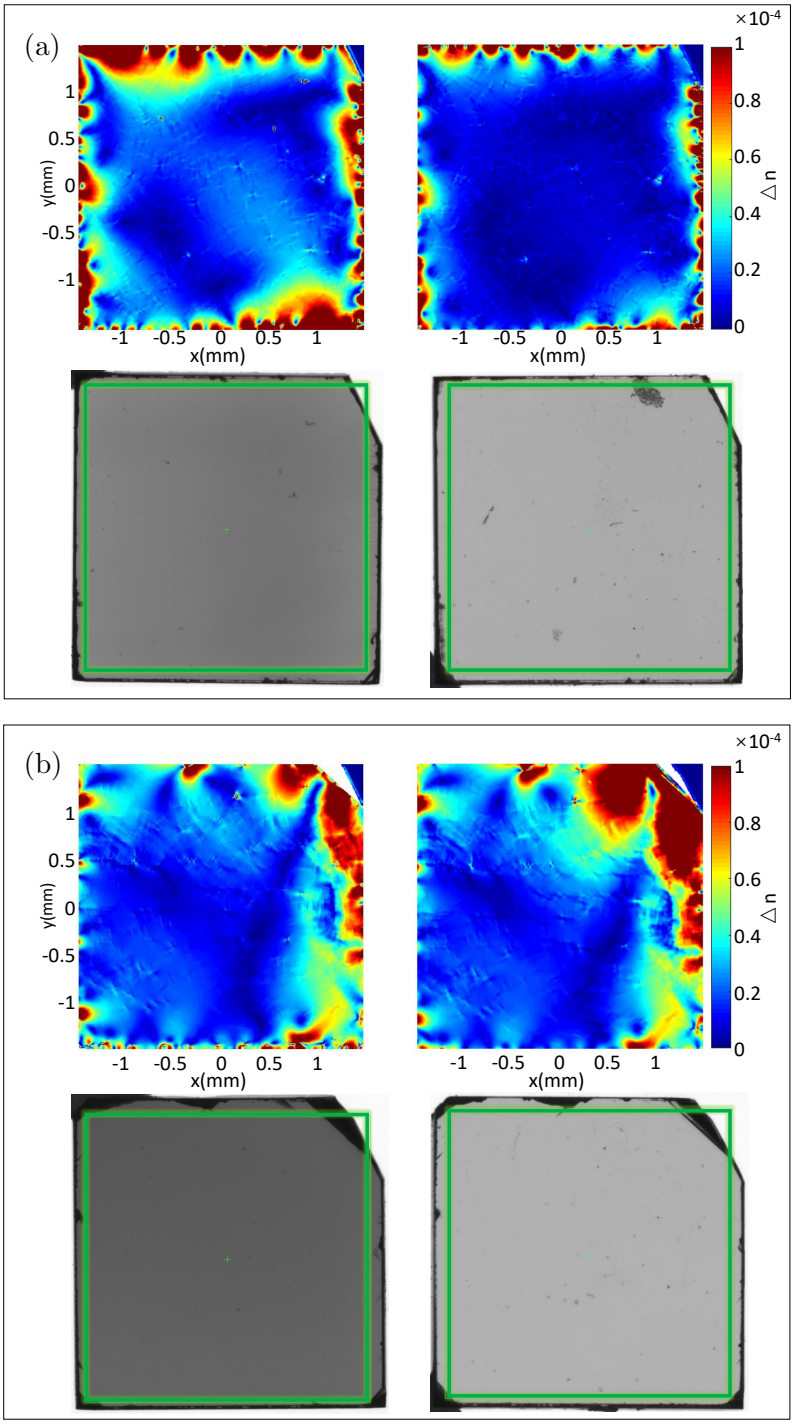

Figure 6.8: Birefringence before and after HPHT annealing for two CVD diamonds. For both (a) and (b), upper: birefringence maps, lower: corresponding bright-field images (the birefringence was measured in the green block); left: before HPHT annealing, right: after HPHT annealing. When annealing with the same conditions, (a) shows a decrease in overall birefringence, while (b) shows an increase in the top right corner, where the 'notch' of the sample is located.

Conclusion

This thesis systematically investigated the nitrogen-vacancy (NV) center formation and properties in bulk chemical vapor deposition (CVD) diamond. For improved sensitivity and material quality, this thesis shows results that balance the NV^- concentration with the coherence time T_2, the NV charge state stability, the diamond absorption and birefringence.

As a foundation of material characterization and optimization, this thesis introduced established methods to determine the concentration of nitrogen-related defects in diamonds. Importantly, the author developed new methods to determine the concentration of NV centers and substitutional single nitrogen atoms (P1 centers), which are the most relevant defects in this context. The author established the method to estimate the NV concentration from the NV photoluminescence (PL), then analyzed the NV charge state by separating the NV emission spectrum into a NV^0 and NV^- contribution via a least-square fitting. A new calibration was applied to the NV-PL method, using a series of CVD diamonds with varying NV concentrations. The new calibration shows a good linear fit for CVD diamonds with NV centers in the ppb level, it provided more reliable results than calibrations using HPHT diamonds, which have low homogeneity and too high nitrogen concentration that can suppress the NV fluorescence.

For P1 centers, the author developed a novel fitting method to determine its concentration via the 270 nm absorption band in the UV-Vis absorption spectrum, which is more widely accessible and easier to implement than the established EPR method. The fitting of the identified bands is a reliable way to extract the 270 nm band from the background, as seen by the good match between measurement and fit, and confirmed by the linear relationship between the EPR result and the author's method. The good agreement with EPR furthermore confirms the assumption that the 270 nm band indeed is mainly caused by P1 centers. This new fitting method performs well for diamond spectra without complex components overlapping with the fitting components. In other words, it can be widely applied to different dia-

mond types apart from as-grown CVD diamonds. Furthermore, the author deduced the absorption cross-section $\sigma = 1.96 \pm 0.15$ cm^{-1}·ppm^{-1} (for common logarithm) and $\sigma_e = 4.51 \pm 0.35$ cm^{-1}·ppm^{-1} (for natural logarithm), which can serve to rapidly determine P1 densities from UV-Vis measurements without the need to calibrate a setup via EPR. This also enables the determination of P1 concentration in a lower end that is hardly detectable by EPR or FTIR methods.

Using the new characterization methods (and other established methods), the author investigated nitrogen-doped CVD-grown diamond by varying the nitrogen to carbon (N/C) ratio in the plasma over a range from 150 to 10^6 ppm. It was found that neutral single substitutional nitrogen (P1 centers) are created with a dependence of $\sim 0.09\sqrt{\mathrm{N/C}}$ and created P1 densities in the CVD growth from 0.2 to 20 ppm. NV centers of 0.03-33.9 ppb were directly created during the growth with a fixed NV^-/P1 ratio of 0.25%. The coherence time T_2 of the NV center after growth showed the expected inverse relationship with P1 centers, and they spanned 48-497 μs for P1 concentrations at the range of 2.6-0.2 ppm respectively. For that range, the coherence time as a function of the P1 concentration agrees with a previous study, when assuming that 75% of the nitrogen was in the form of P1 centers. For higher P1 concentrations (3.2-19.3 ppm), the T_2 of the samples showed a large variation of the values and no longer fitted in the model (although still showed an inverse relationship between the T_2 and P1 concentration). Other nitrogen-related defects and potentially other decoherence sources need to be taken into account for high nitrogen diamonds in future studies. Additionally, this thesis discussed the possibilities to improve the in-situ created NV concentration by engineering the growth parameters. The created NV^- densities (up to ∼30 ppb) and coherence times (up to ∼500 μs) showed that as-grown nitrogen-doped CVD diamond can be used as a sufficient and reproducible sensing material.

Furthermore, the author investigated and optimized the fluence of high-energy electron irradiation (1 MeV and 2 MeV) for an enhanced NV concentration. The results show that increasing irradiation fluence increases NV concentrations, however, there is a certain optimal point, above which more fluence creates mainly additional NV^0 and hardly any more NV^-. This optimum for 2.2 ppm initial P1 was at 1×10^{17}-2×10^{17} e/cm^2 for 2 MeV and at 1×10^{18}-3×10^{18} e/cm^2 for 1MeV irradiation. With this optimum, this thesis achieved a P1 to NV^- conversion ratio of ∼7-8%, with an NV^-/NV ratio ∼66-86%. Higher ratios are possible but not desirable when the charge state is supposed to be negatively dominated. Since P1 centers are the main electron donors to charge the NV centers, the author interpreted the creation of

NV^0 above the optimum as not enough P1 centers are left to provide electrons to charge the NV center. The author also pointed out an important criterion for the conventional growth-irradiation-annealing procedure, that for CVD diamonds, the conversion rate from as-grown P1 to NV centers should be smaller than 10% to fulfill an NV^-/NV ratio above 80%. In the future, this might be overcome by introducing another electron donor to charge the NV^-.

Moreover, this thesis studied the absorption spectral behavior at the UV-Visible range to visually describe defect transformations during irradiation and annealing. The generation of the negatively charged vacancy V^- (ND1 band) was observed after irradiation before annealing, scaling with the fluence. Neutral vacancies V^0 (GR1 band) were also formed for high fluences. After annealing, V^- centers were largely converted, forming NV centers proportional to the irradiation fluence. It was found that the appearance of the GR1 band after irradiation can be an indicator of the NV^0 formation after annealing. This supports further the new model in this thesis, that for over-irradiated samples, the remaining P1 centers are not enough to charge vacancies (or NV centers), therefore neutral vacancies and later neutral NV centers tend to form. From that, the author suggests the UV-Vis absorption spectrum to be a useful tool to determine the optimal irradiation fluence, before annealing the sample.

Treating the samples with the irradiation and annealing protocol discussed above, coherence times T_2 stay consistent with the as-grown ones. This means the irradiation/annealing provides significant advantages for sensing and sensitivity by increasing the NV density and thus the signal strength without compromising the T_2. After treatment, a combination was achieved between 549 μs T_2 with 1 ppb NV^- and 45.5 μs with 168 ppb. The longest T_2=549 μs achieved in this thesis is comparable to T_2 reported previously for single NV [3, 149], as well as for NV ensembles [4], which are both around 600 μs. Compared to previous works, the results in this thesis show its advantages: firstly, for similarly long coherence times, higher NV concentrations were achieved in this thesis (1 ppb NV^- centers in this thesis vs. $\sim$0.18 ppb total NV centers in [4] or a single NV center in [3] and [149]); this thesis created good combinations of high NV concentrations and long coherence times in bulk diamond plates (when better combinations have been only reported for a small spot on the diamond, e.g. in [49]). Combining the enhanced NV^- concentration with long T_2 is an interesting pathway to improve sensitivities in sensing.

Optimizing the NV creation procedure is one of the key requirements for NV-laser

applications. The other key requirement is to reduce the optical loss in the material, which is mainly introduced by diamond absorption and birefringence. The absorption coefficient at around 700 nm is the region of interest, as it exhibits most of the NV fluorescence: this thesis studied the sources of the absorption in this regime and discussed the approach to improve it. The results show that the absorption coefficient at 700 nm increases remarkably with increasing nitrogen contents during the growth with a super-linear correlation. The spectrum shows that this large increase is mainly caused by the 'offset' of the spectrum, which has been suggested originated from non-diamond carbon inclusions [153]. It also needs to be pointed out that over-irradiation creates GR1 bands, which are superposed with the 700 nm regime and increase the absorption coefficient. The subsequent annealing at 1000°C for 2 h annealed out a part of the GR1 band, resulting in a decrease in the absorption. However, as neutral vacancies (GR1 band) can hardly be fully converted, the absorption after treatments were still higher than the as-grown phase. Consequently, avoiding over-irradiation is not only considered for an improved charge state stability, but also for a stable and low absorption. Understanding the sources of the absorption, this thesis also showed improvements in the absorption by optimizing growth parameters and after-growth treatments (which will be discussed below).

The diamond birefringence, in contrast, was found to be reduced for increasing nitrogen concentrations during the CVD growth. Additionally, high nitrogen samples also showed better homogeneity of the birefringence. The individual step of the irradiation or annealing (at 1000°C) showed very limited influence on the birefringence. Both increase and decrease occurred in the samples after the combination of the two steps (i.e. the irradiation followed by subsequent annealing), which appears to depend on the types of existing defects and how vacancies change them. Ultra-low birefringence $\Delta n < 10^{-5}$ is achieved for diamonds with a high nitrogen concentration (P1$\sim$20 ppm) in this thesis.

From the study, the author acquired an understanding of how diamond absorption and birefringence are influenced by the nitrogen content and after-growth treatments. For the goal to decrease the absorption and birefringence, thus reducing the optical loss, high temperature (HT) treatments were conducted, which have shown impressive performance for diamond coloration engineering. Low-pressure high-temperature (LPHT) annealing was conducted at 1800°C in vacuum and H_2 atmosphere, and high-pressure high-temperature (HPHT) annealing was conducted at 1850°C with 5-6 GPa. Using the novel fitting method (developed by the author and introduced in this thesis) to analyze the UV-Vis spectrum before and after

annealing, it was found that both of the treatments did not change the P1 concentration in CVD diamonds. They both reduced the 'ramp' and 360 nm band, indicating the dissociation of vacancy clusters. Most importantly, they both pulled down the 'offset' of the spectrum, leading to a decrease in the absorption coefficient at 700 nm: in particular, HPHT annealing had a stronger effect (reduced $\sim$5 cm^{-1}) than LPHT annealing (reduced $<$1 cm^{-1}). This also provided evidence that the 'offset' links to carbon inclusions, as HPHT annealing operated near the graphite-diamond equilibrium line has a chance to turn graphite back into the diamond (anneal out the carbon inclusions). For a similar reason, LPHT annealing operated in the graphite regime has a higher potential to create cracks in the diamond, which introduced a huge birefringence. Diamonds that were not burned during HPHT annealing show relatively stable (or even improved) birefringence. In conclusion, HT treatments are useful tools to improve the diamond properties after growth and before irradiation. They can significantly reduce the diamond absorption at $\sim$700 nm and have the potential to reduce the diamond birefringence, which leads to a reduced optical loss and improved material performance.

This thesis lays the foundation to further explore and improve NV-diamond properties for sensing applications: firstly, new characterization methods are established to reliably estimate the NV and P1 concentration; secondly, interrelations between diamond properties (N/C ratio, P1, NV concentrations, T_2, absorption and birefringence, etc.) are systematically investigated based on scores of diamond samples; thirdly, optimized NV-ensemble creation procedures in bulk diamond are suggested; finally, potential approaches for further improvement are also discussed based on experimental results. These enable the creation of optimized NV-doped diamonds for sensing applications, and provide a guideline for broader application fields that require NV-doped diamonds.

Zusammenfassung

In dieser Arbeit wurden die Bildung und die Eigenschaften von Stickstoff-Leerstellen (NV) Zentren in Diamant durch chemische Gasphasenabscheidung (CVD) systematisch untersucht. Diese Arbeit zeigt Ergebnisse zur verbesserten Empfindlichkeit und Materialqualität und zeigt die ZusammenhÃ¤nge verschiedener Eigenschaften auf, wie die NV^--Konzentration, die Kohärenzzeit T_2, die NV-Ladungszustandsstabilität, die Diamantabsorption und die Doppelbrechung, und wÃ¤gt diese gegeneinander ab.

Als Grundlage für die Materialcharakterisierung und -optimierung wurden in dieser Arbeit etablierte Methoden zur Bestimmung der Konzentration von stickstoffbezogenen Defekten in Diamant eingeführt. Vor allem entwickelte die Autorin neue Methoden, um die Konzentration von NV-Zentren und substitutionellen einzelnen Stickstoffatomen (P1-Zentren) zu bestimmen, die in diesem Zusammenhang die wichtigsten Defekte sind. Die Autorin entwickelte eine Methode zur Schätzung der NV-Konzentration aus der NV-Photolumineszenz (PL) und analysierte dann den NV-Ladungszustand durch Aufteilung des NV-Emissionsspektrums in einen NV^0- und einen NV^--Beitrag mittels eines Least-Square-Fits. Eine neue Kalibrierung wurde auf die NV-PL-Methode angewandt, wobei eine Reihe von CVD-Diamanten mit unterschiedlichen NV-Konzentrationen verwendet wurde. Die neue Kalibrierung zeigte eine gute lineare Anpassung für CVD-Diamanten mit NV-Zentren im ppb-Bereich und lieferte zuverlässigere Ergebnisse als Kalibrierungen mit HPHT-Diamanten, die eine geringe Homogenität und eine zu hohe Stickstoffkonzentration aufweisen, welche die NV-Fluoreszenz unterdrücken kann.

Für P1-Zentren entwickelte die Autorin eine neuartige Fitting-Methode zur Bestimmung der Konzentration über die 270 nm-Absorptionsbande im UV-Vis-Absorptionsspektrum, die besser zugänglich und einfacher zu implementieren ist als die etablierte EPR-Methode. Die Anpassung der identifizierten Banden ist ein zuverlässiger Weg, um die 270 nm-Bande aus dem Hintergrund zu extrahieren, wie die gute Übereinstimmung zwischen Messung und Anpassung zeigt und durch die lin-

eare Beziehung zwischen dem EPR-Ergebnis und der Methode der Autorin bestätigt wird. Die gute Übereinstimmung mit der EPR bestätigt außerdem die Annahme, dass die 270 nm-Bande tatsächlich hauptsächlich durch P1-Zentren verursacht wird. Diese neue Anpassungsmethode funktioniert gut für Diamantspektren ohne komplexe Komponenten, die sich mit den Anpassungskomponenten überschneiden. Mit anderen Worten, sie kann in großem Umfang auf verschiedene Diamanttypen angewandt werden, abgesehen von frisch gewachsenen CVD-Diamanten. Außerdem hat die Autorin den Absorptionsquerschnitt $\sigma = 1.96 \pm 0.15$ cm^{-1}·ppm^{-1} (für den gemeinsamen Logarithmus) und $\sigma_e = 4.51 \pm 0.35$ cm^{-1}·ppm^{-1} (für den natürlichen Logarithmus) bestimmt, die zur schnellen Bestimmung von P1-Dichten aus UV-Vis-Messungen dienen können, ohne dass eine EPR-Kalibrierung erforderlich ist. Dies ermöglicht auch die Bestimmung der P1-Konzentration in einem unteren Bereich, der mit EPR- oder FTIR-Methoden kaum nachweisbar ist.

Unter Verwendung der neuen Charakterisierungsmethoden (und anderer etablierter Methoden) untersuchte die Autorin stickstoffdotierten CVD-gewachsenen Diamant, indem das Verhältnis von Stickstoff zu Kohlenstoff (N/C) im Plasma über einen Bereich von 150 bis 10^6 ppm variiert wurde. Es wurde festgestellt, dass neutraler einzelner Substitutionsstickstoff (P1-Zentren) mit einer Abhängigkeit von $\sim 0,09\sqrt{\mathrm{N/C}}$ entsteht und P1-Dichten im CVD-Wachstum von 0,2 bis 20 ppm erzeugt werden. NV-Zentren von 0,03-33,9 ppb wurden direkt während des Wachstums mit einem festen NV$^-$/P1-Verhältnis von 0,25% erzeugt. Die Kohärenzzeit T_2 des NV-Zentrums nach dem Wachstum zeigte die erwartete umgekehrte Beziehung zu den P1-Zentren, und sie betrug 48-497 μs für P1-Konzentrationen im Bereich von 2,6-0,2 ppm. Für diesen Bereich stimmt die Kohärenzzeit als Funktion der P1-Konzentration mit einer früheren Studie überein, wenn man annimmt, dass 75% des Stickstoffs in Form von P1-Zentren vorliegt. Bei höheren P1-Konzentrationen (3,2-19,3 ppm) zeigte die T_2 der Proben eine große Schwankung der Werte und passte nicht mehr in das Modell (obwohl immer noch eine inverse Beziehung zwischen der T_2 und der P1-Konzentration bestand). Andere stickstoffbedingte Defekte und möglicherweise andere Dekohärenzquellen müssen bei Diamanten mit hohem Stickstoffgehalt in zukünftigen Studien berücksichtigt werden. Darüber hinaus wurden in dieser Arbeit die Möglichkeiten zur Verbesserung der in-situ erzeugten NV-Konzentration durch Veränderung der Wachstumsparameter diskutiert. Die erzeugten NV$^-$-Dichten (bis zu ∼30 ppb) und Kohärenzzeiten (bis zu ∼500 μs) zeigten, dass der gewachsene stickstoffdotierte CVD-Diamant als ausreichendes und reproduzierbares Sensormaterial verwendet werden kann.

Darüber hinaus untersuchte und optimierte die Autorin die Fluenz der hochenergetischen Elektronenbestrahlung (1 MeV und 2 MeV) für eine erhöhte NV-Konzentration. Die Ergebnisse zeigen, dass eine Erhöhung der Bestrahlungsfluenz die NV-Konzentration erhöht, jedoch gibt es einen bestimmten optimalen Punkt, oberhalb dessen mehr Fluenz hauptsächlich zusätzliche NV^0 und kaum mehr NV^- erzeugt. Dieses Optimum für 2,2 ppm Ausgangs-P1 lag bei 1×10^{17}-2×10^{17} e/cm^2 für 2 MeV und bei 1×10^{18}-3×10^{18} e/cm^2 für 1MeV-Bestrahlung. Mit diesem Optimum wurde in dieser Arbeit ein P1-zu-NV^--Umwandlungsverhältnis von ∼7-8% erreicht, mit einem NV^-/NV-Verhältnis ∼66-86%. Höhere Verhältnisse sind möglich, aber nicht wünschenswert wenn der Ladungszustand negativ dominiert sein soll. Da die P1-Zentren die Hauptelektronenspender für die Ladung der NV-Zentren sind, interpretierte die Autorin die Entstehung von NV^0 oberhalb des Optimums so, dass nicht genügend P1-Zentren übrig sind, um Elektronen für die Ladung der NV-Zentren bereitzustellen. Auf der Grundlage dieses Modells nehmen wir an, dass die optimale Fluenz mit der P1-Dichte für ähnlich gewachsene CVD-Diamanten skaliert. Die Autorin weist auch auf ein wichtiges Kriterium für das herkömmliche Wachstums-Bestrahlungs-Glühverfahren hin, nämlich dass bei CVD-Diamanten die Umwandlungsrate von gewachsenen P1- zu NV-Zentren kleiner als 10% sein sollte, um ein NV^-/NV-Verhältnis von über 80% zu erreichen. In Zukunft könnte dies durch die Einführung eines weiteren Elektronendonors zur Aufladung der NV^- überwunden werden.

Darüber hinaus wurde in dieser Arbeit das Absorptionsspektrumsverhalten im UV-Vis-Bereich untersucht, um Defektumwandlungen während der Bestrahlung und des Annealings visuell zu beschreiben. Die Bildung der negativ geladenen Leerstellen V^- (ND1-Bande) wurde nach der Bestrahlung vor dem Annealing beobachtet und skaliert mit der Fluenz. Neutrale Leerstellen V^0 (GR1-Bande) wurden auch bei hohen Fluenzen gebildet. Nach dem Annealing wurden die V^--Zentren weitgehend umgewandelt und bildeten NV-Zentren, die proportional zur Bestrahlungsstärke waren. Es wurde festgestellt, dass das Auftreten der GR1-Bande nach der Bestrahlung ein Indikator für die NV^0-Bildung nach dem Annealing sein kann. Dies unterstützt das neue Modell in dieser Arbeit, dass bei überbestrahlten Proben die verbleibenden P1-Zentren nicht ausreichen, um Leerstellen (oder NV-Zentren) zu laden, so dass sich neutrale Leerstellen und später neutrale NV-Zentren bilden können. Daraus leitet die Autorin ab, dass das UV-Vis-Absorptionsspektrum ein nützliches Instrument zur Bestimmung der optimalen Bestrahlungsfluenz vor dem Tempern der Probe ist.

Wenn die Proben mit dem oben beschriebenen Bestrahlungs- und Annealingprotokoll behandelt werden, bleiben die Kohärenzzeiten T_2 konsistent mit den Zeiten im Ausgangszustand. Das bedeutet, dass die Bestrahlung/das Annealing erhebliche Vorteile für die Erkennung und Empfindlichkeit bietet, da die NV-Dichte und damit die Signalstärke erhöht wird, ohne die T_2 zu beeinträchtigen. Nach der Behandlung wurde eine Kombination von 549 μs T_2 mit 1 ppb NV^- und 45,5 μs mit 168 ppb erreicht. Die längste T_2=549 μs, die in dieser Arbeit erreicht wurde, ist vergleichbar mit T_2, die zuvor für einzelne NV [3, 149] sowie für NV-Ensembles [4] berichtet wurden, welche beide um 600 μs liegen. Im Vergleich zu früheren Arbeiten zeigt diese Arbeit ihre Vorteile: Erstens wurden bei ähnlich langen Kohärenzzeiten höhere NV Konzentrationen erreicht (1 ppb NV^--Zentren in dieser Arbeit vs. ∼0. 18 ppb gesamte NV-Zentren in [4] oder ein einzelnes NV-Zentrum in [3] und [149]); diese Arbeit schuf gute Kombinationen von hohen NV-Konzentrationen und langen Kohärenzzeiten in massiven Diamantplatten (wenn bessere Kombinationen nur für einen kleinen Spot auf dem Diamanten berichtet wurden, z.B. in [49]). Die Kombination der erhöhten NV^--Konzentration mit langer T_2 ist ein interessanter Weg, um die Empfindlichkeit bei der Sensorik zu verbessern.

Die Optimierung des NV-Erzeugungsverfahrens ist eine der wichtigsten Voraussetzungen für NV-Laseranwendungen. Eine weitere wichtige Voraussetzung ist die Verringerung der optischen Verluste im Material, die hauptsächlich durch die Absorption und Doppelbrechung von Diamant verursacht werden. Der Absorptionskoeffizient bei etwa 700 nm ist der Bereich, der von Interesse ist, da er den größten Teil der NV-Fluoreszenz aufweist: In dieser Arbeit wurden die Quellen der Absorption in diesem Bereich untersucht und der Ansatz zu ihrer Verbesserung erörtert. Die Ergebnisse zeigen, dass der Absorptionskoeffizient bei 700 nm mit zunehmendem Stickstoffgehalt während des Wachstums deutlich ansteigt und eine superlineare Korrelation aufweist. Das Spektrum zeigt, dass dieser starke Anstieg hauptsächlich durch den 'Offset' des Spektrums verursacht wird, von dem man annimmt, dass er von nichtdiamantischen Kohlenstoffeinschlüssen stammt. Es muss auch darauf hingewiesen werden, dass eine zu starke Bestrahlung GR1-Bänder erzeugt, die sich mit dem 700 nm-Bereich überlagern und den Absorptionskoeffizienten erhöhen. Durch das anschließende Annealing bei 1000°C für 2 h wurde ein Teil der GR1-Bande ausgeheilt, was zu einem Rückgang der Absorption führte. Da jedoch neutrale Leerstellen (GR1-Bande) kaum vollständig umgewandelt werden können war die Absorption nach der Behandlung immer noch höher als in der unbestrahlten Phase. Folglich ist eine Vermeidung von Überbestrahlung nicht nur für eine verbesserte Ladungsstabilität,

sondern auch für eine stabile und niedrige Absorption erforderlich. Da die Quellen der Absorption bekannt sind, werden in dieser Arbeit auch Verbesserungen der Absorption durch die Optimierung der Wachstumsparameter und Nachbehandlungen aufgezeigt (auf die weiter unten eingegangen wird).

Im Gegensatz dazu wurde festgestellt, dass die Diamant-Doppelbrechung mit zunehmender Stickstoffkonzentration während des CVD-Wachstums abnimmt. Außerdem zeigten Proben mit hohem Stickstoffgehalt eine bessere Homogenität der Doppelbrechung. Die einzelnen Schritte der Bestrahlung oder des Temperns (bei 1000°C) hatten nur einen sehr geringen Einfluss auf die Doppelbrechung. Nach der Kombination der beiden Schritte (d. h. Bestrahlung und anschließendes Annealing) kam es sowohl zu einer Erhöhung als auch zu einer Verringerung der Doppelbrechung, was offenbar von der Art der vorhandenen Defekte und deren Veränderung durch Leerstellen abhängt. Eine extrem niedrige Doppelbrechung $\Delta n < 10^{-5}$ wird in dieser Arbeit für Diamanten mit einer hohen Stickstoffkonzentration (P1$\sim$20 ppm) erreicht.

Aus der Arbeit hat die Autorin ein Verständnis dafür gewonnen, wie die Absorption und Doppelbrechung von Diamanten durch den Stickstoffgehalt und Nachbehandlungen beeinflusst werden. Um die Absorption und die Doppelbrechung zu verringern und damit den optischen Verlust zu reduzieren, wurden Hochtemperaturbehandlungen (HT) durchgeführt, die eine beeindruckende Leistung bei der Entwicklung der Diamantfärbung gezeigt haben. Das Niederdruck-Hochtemperatur-Annealing (LPHT) wurde bei 1800°C im Vakuum und in H_2-Atmosphäre durchgeführt, und das Hochdruck-Hochtemperatur-Annealing (HPHT) wurde bei 1850°C mit 5-6 GPa durchgeführt. Unter Verwendung der neuartigen Anpassungsmethode (die von derAutorin entwickelt und in dieser Arbeit vorgestellt wurde) zur Analyse des UV-Vis-Spektrums vor und nach dem Tempern wurde festgestellt, dass beide Behandlungen die P1-Konzentration in CVD-Diamanten nicht veränderten. Sie verringerten beide die RRampeünd die 360 nm-Bande, was auf die Dissoziation von Leerstellenclustern hinweist. Vor allem aber verringerten beide den 'Offset' des Spektrums, was zu einem Rückgang des Absorptionskoeffizienten bei 700 nm führte: Insbesondere die HPHT-Temperung hatte eine stärkere Wirkung (reduzierte $\sim$5 cm^{-1}) als die LPHT-Temperung (reduzierte $<$1 cm^{-1}). Dies ist auch ein Beweis dafür, dass der Öffsetmmit den Kohlenstoffeinschlüssen zusammenhängt, da ein HPHT-Annealing in der Nähe der Graphit-Diamant-Gleichgewichtslinie die Chance hat, Graphit wieder in Diamant zu verwandeln (Ausglühen der Kohlenstoffeinschlüsse). Aus dem gleichen Grund hat das LPHT-Annealing, das im Graphitbereich durchge-

führt wird, ein höheres Potenzial Risse im Diamanten zu erzeugen, die zu einer starken Doppelbrechung führen. Diamanten, die während des HPHT-Annealings nicht verbrannt wurden, zeigen eine relativ stabile (oder sogar verbesserte) Doppelbrechung. Zusammenfassend lässt sich sagen, dass HT-Behandlungen nützliche Instrumente zur Verbesserung der Diamanteigenschaften nach dem Wachstum und vor der Bestrahlung sind. Sie können die Absorption des Diamanten bei ∼700 nm erheblich reduzieren und haben das Potenzial, die Doppelbrechung des Diamanten zu verringern, was zu einem geringeren optischen Verlust und einer verbesserten Materialleistung führt.

Diese Arbeit legt den Grundstein für die weitere Erforschung und Verbesserung der Eigenschaften von NV-Diamant für sensorische Anwendungen: Erstens werden neue Charakterisierungsmethoden etabliert, um die NV- und P1-Konzentration zuverlässig abzuschätzen; zweitens werden die Zusammenhänge zwischen den Diamanteigenschaften (N/C-Verhältnis, P1, NV-Konzentrationen, T_2, Absorption und Doppelbrechung usw.) systematisch anhand der Ergebnisse von Diamantproben untersucht; drittens werden optimierte Verfahren zur Erzeugung von NV-Ensembles in Bulk-Diamant vorgeschlagen; schließlich werden auch potenzielle Ansätze für weitere Verbesserungen auf der Grundlage experimenteller Ergebnisse diskutiert. Diese ermöglichen die Herstellung optimierter NV-dotierter Diamanten für sensorische Anwendungen und bieten einen Leitfaden für breitere Anwendungsbereiche, die NV-dotierte Diamanten erfordern.

Appendix

A Growth conditions and sample preparation

Multiple (100)-oriented CVD diamond series have been grown and investigated in this study. The in-house growth has been conducted by Julia Langer and Volker Cimalla. Before CVD growth, basic characterization (WLI/DIC images, crossed polarizer, HR-XRD, etc.) has been conducted to ensure the quality of the substrates, and all substrates have undergone an extended cleaning process, which included boiling them in nitro-sulfuric acid and successively several steps of organic solvent cleaning. An in-situ plasma etching pretreatment step has been conducted prior to the growth based on the findings published in [166].

The nitrogen-doped CVD growth was run in an ellipsoidal-shaped CVD reactor with a 2.45 GHz microwave frequency and equipped with a 6 kW microwave generator [167]. The growth was conducted at 210 mbar, between 800-900 °C on the substrate, with 2.67% of methane, 0.1 sccm oxygen and an adjustable flow of nitrogen doping gas. The growth parameters for the important growth series are listed in Table. A.1. We kept the growth conditions constant within the series to ensure the comparability of the samples (except for the N/C ratio in the two nitrogen series, for which we varied them on purpose to investigate the in-situ P1 and NV creation). The microwave power, pressure and methane flow have been well controlled.

The growth temperature has been measured on the substrate by a narrow band radiation thermometer, with an error of ±10 °C. These values of temperature need to be treated carefully as the temperature during the CVD run varies in terms of the thermal contact of the sample to the substrate holder. As they are measured manually, the measurements are not strictly at the same time intervals. The substrate temperature has an influence on the resulting outcome, however, the introduced nitrogen into the reactor chamber has a much more significant influence in this work. The nitrogen within the gas even indirectly influences the substrate temperature since

Table A.1: Growth parameters for important nitrogen-doped CVD series.

Series	Sample	N/C (ppm)	Temperature (°C)[1]	Thickness (μm)	Duration (h)	Microwave Power (kW)
Nitrogen series #1	NDT-26	150	800	246.5	67.5	2
	NDT-14	500	770	22.6	15	
	NDT-07	1500	800	195.8	20	
	NDT-34	2500	800	142.5	15	
	NDT-01	4500	810	64.5	6	
	NDT-02	7429	820	58.6	6	
	NDT-12	8500	770	80	6	
Nitrogen series #2	Cas-40	9722	800	581.8	44	3
	Cas-48	42777	845	653.8		
	Cas-68	77142	870	634.9		
	Cas-44	87499	810	559.7		
	Cas-51	173571	865	793.4		
	Cas-49	34143	840	561.4		
	Cas-50	694286	890	608		
2 MeV series	I2-01	8500	830	308.2	19	2.5
	I2-02		820	319.1		
	I2-04		820	308.6		
	I2-05		840	318.3		
	I2-08		840	303.2		
1 MeV series	I1-39	8500	800	696	44	2.5
	I1-50		800	716		
	I1-28		820	665.6		
	I1-29		800	688		

All samples have been grown with a pressure of 210 mbar and 2.67% methane.
[1] Average estimated growth temperature

the substrates are heated through the plasma and the gas temperature changes with nitrogen introduction.

After growth, Nitrogen series #2 and the two irradiation series have been laser cut from the substrate then polished on both sides with a surface roughness Ra <0.5 nm. In this sense, no substrate contributes to the characterization for these series. For Nitrogen series #1, only the polishing step has been conducted, as some samples with a thin overgrown layer might not survive from the laser cutting. Losses in sample thickness arises during the laser cutting and polishing steps, which can be precisely measured afterwards. The thicknesses listed in Table. A.1 are growth layer thicknesses before removal from the substrate. The actual thickness after polishing of Nitrogen series #1 (for overgrown layer) ranged from ∼20 to 245 μm. For Nitrogen series #2 after laser cutting and polishing ∼500 μm, and for the two irradiation series respectively ∼300 μm and ∼650 μm.

B Influences of annealing temperatures

Table B.2: Some interesting annealing temperatures and their influences on NV creation and related diamond properties. Here the annealing is designated as subsequent annealing.

Temperature	Influence	Reference
>400 °C	Vacancies and interstitial nitrogen atoms introduced by implantation migrate and annihilate with each other	[88, 89]
>800 °C	The diffusion of vacancies becomes significant	[49, 89]
850-1000 °C	NV concentration reaches a plateau and remains stable with increasing temperature	[27, 139]
1000-1200 °C	NV concentration and NV^-/NV ratio decreases with increasing temperature	[86]
800-1500 °C	Elongated in coherence times can be achieved under specific ambient conditions	[94, 141, 143]
>1500 °C	Vacancy clusters start to dissociate	[107]
1800-2100 °C	Most brown-color-related defects are annealed out Moderate annealing temperature to achieve pink color in type IIa diamonds	

Publications of the author

Journal articles

Tingpeng Luo, Lukas Lindner, Julia Langer, Volker Cimalla, Xavier Vidal, Felix Hahl, Christoph Schreyvogel, Shinobu Onoda, Shuya Ishii, Takeshi Ohshima, Di Wang, David A Simpson, Brett C Johnson, Marco Capelli and Jan Jeske. Creation of nitrogen-vacancy centers in chemical vapor deposition diamond for sensing applications. *New Journal of Physics*, 24(3): 033030, 2022.

Tingpeng Luo, Lukas Lindner, Rémi Blinder, Marco Capelli, Julia Langer, Volker Cimalla, Felix A Hahl, Xavier Vidal, and Jan Jeske. Rapid determination of single substitutional nitrogen N_s^0 concentration in diamond from UV-Vis spectroscopy. *Applied Physics Letters*, 121(6):064002, 2022

Marco Capelli, Lukas Lindner, **Tingpeng Luo**, Jan Jeske, Hiroshi Abe, Shinobu Onoda, Takeshi Ohshima, Brett Johnson, David A Simpson, Alastair Stacey, Philipp Reineck, Brant C Gibson and Andrew D Greentree. Proximal nitrogen reduces the fluorescence quantum yield of nitrogen-vacancy centres in diamond. *New Journal of Physics*, 24(3):033053, 2022.

Felix Hahl, Lukas Lindner, Xavier Vidal, **Tingpeng Luo**, Takeshi Ohshima, Shinobu Onoda, Shuya Ishii, Alexandre M. Zaitsev, Marco Capelli, Brant C. Gibson, Andrew D. Greentree and Jan Jeske. Magnetic-field-dependent stimulated emission from nitrogen-vacancy centres in diamond. *Science Advances*, 8(22):eabn7192, 2021

Julia Langer, Volker Cimalla, Vadim Lebedev, Lutz Kirste, Mario Prescher, **Tingpeng Luo**, Jan Jeske, and Oliver Ambacher. Manipulation of the in situ nitrogen-vacancy doping efficiency in CVD-grown diamond. *physica status solidi (a)*, page 2100756, 2022

Patents

Felix Hahl, Jan Jeske, **Tingpeng Luo**. Diamant mit hoher Dichte von Farbzentren und verbesserten optischen Eigenschaften und Verfahren zur Herstellung. *patent submitted for registration*, 2021

Serhiy Danylyuk, Sascha Brose, Klaus Bergmann, **Tingpeng Luo**, Jan Jeske, Ralf Ostendorf. Verfahren und Anordnung zur lokalisierten Defekterzeugung für die Quantentechnologie. *patent submitted for registration*, 2021

Bibliography

[1] G Davies and MF Hamer. Optical studies of the 1.945 ev vibronic band in diamond. *Proceedings of the Royal Society of London. A. Mathematical and Physical Sciences*, 348(1653):285–298, 1976.

[2] Gopalakrishnan Balasubramanian, IY Chan, Roman Kolesov, Mohannad Al-Hmoud, Julia Tisler, Chang Shin, et al. Nanoscale imaging magnetometry with diamond spins under ambient conditions. *Nature*, 455(7213):648–651, 2008.

[3] Jeronimo R Maze, Paul L Stanwix, James S Hodges, Seungpyo Hong, Jacob M Taylor, Paola Cappellaro, et al. Nanoscale magnetic sensing with an individual electronic spin in diamond. *Nature*, 455(7213):644–647, 2008.

[4] Paul L Stanwix, Linh My Pham, Jeronimo R Maze, D Le Sage, Tsun Kwan Yeung, Paola Cappellaro, et al. Coherence of nitrogen-vacancy electronic spin ensembles in diamond. *Physical Review B*, 82(20):201201, 2010.

[5] Marcus W Doherty, Neil B Manson, Paul Delaney, Fedor Jelezko, Jörg Wrachtrup, and Lloyd CL Hollenberg. The nitrogen-vacancy colour centre in diamond. *Physics Reports*, 528(1):1–45, 2013.

[6] Igor Aharonovich, Andrew D Greentree, and Steven Prawer. Diamond photonics. *Nature Photonics*, 5(7):397–405, 2011.

[7] MW Doherty, F Dolde, H Fedder, F Jelezko, J Wrachtrup, NB Manson, et al. Theory of the ground-state spin of the NV^- center in diamond. *Physical Review B*, 85(20):205203, 2012.

[8] Christian L Degen, Friedemann Reinhard, and Paola Cappellaro. Quantum sensing. *Reviews of Modern Physics*, 89(3):035002, 2017.

[9] F Jelezko, T Gaebel, I Popa, A Gruber, and J Wrachtrup. Observation of coherent oscillations in a single electron spin. *Physical Review Letters*, 92:076401, Feb 2004.

[10] MV Gurudev Dutt, L Childress, L Jiang, E Togan, J Maze, F Jelezko, AS Zibrov, PR Hemmer, and MD Lukin. Quantum register based on individual electronic and nuclear spin qubits in diamond. *Science*, 316(5829):1312–1316, 2007.

[11] P Neumann, N Mizuochi, F Rempp, P Hemmer, H Watanabe, S Yamasaki, V Jacques, T Gaebel, F Jelezko, and J Wrachtrup. Multipartite entanglement among single spins in diamond. *Science*, 320(5881):1326–1329, 2008.

[12] Dmitry Budker and Michael Romalis. Optical magnetometry. *Nature Physics*, 3(4):227–234, 2007.

[13] John F Barry, Jennifer M Schloss, Erik Bauch, Matthew J Turner, Connor A Hart, Linh M Pham, et al. Sensitivity optimization for NV-diamond magnetometry. *Reviews of Modern Physics*, 92(1):015004, 2020.

[14] A Gruber, A Drabenstedt, C Tietz, L Fleury, J Wrachtrup, and C von Borczyskowski. Scanning confocal optical microscopy and magnetic resonance on single defect centers. *Science*, 276(5321):2012–2014, 1997.

[15] A Dräbenstedt, L Fleury, C Tietz, F Jelezko, S Kilin, A Nizovtzev, and J Wrachtrup. Low-temperature microscopy and spectroscopy on single defect centers in diamond. *Physical Review B*, 60(16):11503, 1999.

[16] Rosa Brouri, Alexios Beveratos, Jean-Philippe Poizat, and Philippe Grangier. Photon antibunching in the fluorescence of individual color centers in diamond. *Optics Letters*, 25(17):1294–1296, 2000.

[17] Christian Kurtsiefer, Sonja Mayer, Patrick Zarda, and Harald Weinfurter. Stable solid-state source of single photons. *Physical Review Letters*, 85(2):290, 2000.

[18] Fedor Jelezko and Jörg Wrachtrup. Single defect centres in diamond: A review. *physica status solidi (a)*, 203(13):3207–3225, 2006.

[19] Ilya P Radko, Mads Boll, Niels M Israelsen, Nicole Raatz, Jan Meijer, Fedor Jelezko, Ulrik L Andersen, and Alexander Huck. Determining the internal quantum efficiency of shallow-implanted nitrogen-vacancy defects in bulk diamond. *Optics Express*, 24(24):27715–27725, 2016.

[20] Ettore Bernardi, Richard Nelz, Selda Sonusen, and Elke Neu. Nanoscale sensing using point defects in single-crystal diamond: recent progress on nitrogen vacancy center-based sensors. *Crystals*, 7(5):124, 2017.

[21] Gopalakrishnan Balasubramanian, Philipp Neumann, Daniel Twitchen, Matthew Markham, Roman Kolesov, Norikazu Mizuochi, Junichi Isoya, Jocelyn Achard, Johannes Beck, Julia Tissler, et al. Ultralong spin coherence time in isotopically engineered diamond. *Nature Materials*, 8(5):383–387, 2009.

[22] A Jarmola, VM Acosta, K Jensen, S Chemerisov, and D Budker. Temperature- and magnetic-field-dependent longitudinal spin relaxation in nitrogen-vacancy ensembles in diamond. *Physical Review Letters*, 108(19):197601, 2012.

[23] T Rosskopf, A Dussaux, K Ohashi, M Loretz, Romana Schirhagl, H Watanabe, S Shikata, Kohei M Itoh, and CL Degen. Investigation of surface magnetic noise by shallow spins in diamond. *Physical Review Letters*, 112(14):147602, 2014.

[24] ED Herbschleb, H Kato, Y Maruyama, T Danjo, T Makino, S Yamasaki, I Ohki, K Hayashi, H Morishita, M Fujiwara, et al. Ultra-long coherence times amongst room-temperature solid-state spins. *Nature Communications*, 10(1):1–6, 2019.

[25] CL Degen. Scanning magnetic field microscope with a diamond single-spin sensor. *Applied Physics Letters*, 92(24):243111, 2008.

[26] JM Taylor, P Cappellaro, L Childress, L Jiang, D Budker, PR Hemmer, et al. High-sensitivity diamond magnetometer with nanoscale resolution. *Nature Physics*, 4(10):810–816, 2008.

[27] Victor M Acosta, Erik Bauch, Micah P Ledbetter, Charles Santori, K-MC Fu, Paul E Barclay, et al. Diamonds with a high density of nitrogen-vacancy centers for magnetometry applications. *Physical Review B*, 80(11):115202, 2009.

[28] HJ Mamin, M Kim, MH Sherwood, CT Rettner, K Ohno, DD Awschalom, et al. Nanoscale nuclear magnetic resonance with a nitrogen-vacancy spin sensor. *Science*, 339(6119):557–560, 2013.

[29] Michael Sean Grinolds, Sungkun Hong, Patrick Maletinsky, Lan Luan, Mikhail D Lukin, Ronald Lee Walsworth, et al. Nanoscale magnetic imaging of a single electron spin under ambient conditions. *Nature Physics*, 9(4):215–219, 2013.

[30] David Le Sage, Koji Arai, David R Glenn, Stephen J DeVience, Linh M Pham, Lilah Rahn-Lee, et al. Optical magnetic imaging of living cells. *Nature*, 496(7446):486–489, 2013.

[31] Florian Dolde, Helmut Fedder, Marcus W Doherty, Tobias Nöbauer, Florian Rempp, Gopalakrishnan Balasubramanian, et al. Electric-field sensing using single diamond spins. *Nature Physics*, 7(6):459–463, 2011.

[32] Florian Dolde, Marcus W Doherty, Julia Michl, Ingmar Jakobi, Boris Naydenov, Sebastien Pezzagna, et al. Nanoscale detection of a single fundamental charge in ambient conditions using the NV^- center in diamond. *Physical Review Letters*, 112(9):097603, 2014.

[33] Preeti Ovartchaiyapong, Kenneth W Lee, Bryan A Myers, and Ania C Bleszynski Jayich. Dynamic strain-mediated coupling of a single diamond spin to a mechanical resonator. *Nature Communications*, 5(1):1–6, 2014.

[34] J Teissier, A Barfuss, P Appel, E Neu, and P Maletinsky. Strain coupling of a nitrogen-vacancy center spin to a diamond mechanical oscillator. *Physical Review Letters*, 113(2):020503, 2014.

[35] VM Acosta, E Bauch, MP Ledbetter, A Waxman, L-S Bouchard, and D Budker. Temperature dependence of the nitrogen-vacancy magnetic resonance in diamond. *Physical Review Letters*, 104(7):070801, 2010.

[36] G Kucsko, PC Maurer, NY Yao, HJ Kubo, Mand Noh, PK Lo, et al. Nanometre-scale thermometry in a living cell. *Nature*, 500(7460):54–58, 2013.

[37] Philipp Neumann, Ingmar Jakobi, Florian Dolde, Christian Burk, Rolf Reuter, Gerald Waldherr, et al. High-precision nanoscale temperature sensing using single defects in diamond. *Nano Letters*, 13(6):2738–2742, 2013.

[38] David M Toyli, Charles F de las Casas, David J Christle, Viatcheslav V Dobrovitski, and David D Awschalom. Fluorescence thermometry enhanced by the quantum coherence of single spins in diamond. *Proceedings of the National Academy of Sciences*, 110(21):8417–8421, 2013.

[39] Marcus W Doherty, Viktor V Struzhkin, David A Simpson, Liam P McGuinness, Yufei Meng, Alastair Stacey, et al. Electronic properties and metrology applications of the diamond NV^- center under pressure. *Physical Review Letters*, 112(4):047601, 2014.

[40] Loïc Rondin, Jean-Philippe Tetienne, Thomas Hingant, Jean-François Roch, Patrick Maletinsky, and Vincent Jacques. Magnetometry with nitrogen-vacancy defects in diamond. *Reports on Progress in Physics*, 77(5):056503, 2014.

[41] Francesco Casola, Toeno Van Der Sar, and Amir Yacoby. Probing condensed matter physics with magnetometry based on nitrogen-vacancy centres in diamond. *Nature Reviews Materials*, 3(1):1–13, 2018.

[42] Romana Schirhagl, Kevin Chang, Michael Loretz, and Christian L Degen. Nitrogen-vacancy centers in diamond: nanoscale sensors for physics and biology. *Annual Review of Physical Chemistry*, 65:83–105, 2014.

[43] Yuzhou Wu, Fedor Jelezko, Martin B Plenio, and Tanja Weil. Diamond quantum devices in biology. *Angewandte Chemie International Edition*, 55(23):6586–6598, 2016.

[44] David R Glenn, Dominik B Bucher, Junghyun Lee, Mikhail D Lukin, Hongkun Park, and Ronald L Walsworth. High-resolution magnetic resonance spectroscopy using a solid-state spin sensor. *Nature*, 555(7696):351–354, 2018.

[45] Dominik B Bucher, Diana PL Aude Craik, Mikael P Backlund, Matthew J Turner, Oren Ben Dor, David R Glenn, and Ronald L Walsworth. Quantum diamond spectrometer for nanoscale NMR and ESR spectroscopy. *Nature Protocols*, 14(9):2707–2747, 2019.

[46] Andreas W Schell, Günter Kewes, Tim Schröder, Janik Wolters, Thomas Aichele, and Oliver Benson. A scanning probe-based pick-and-place procedure for assembly of integrated quantum optical hybrid devices. *Review of Scientific Instruments*, 82(7):073709, 2011.

[47] Tony X Zhou, Rainer J Stöhr, and Amir Yacoby. Scanning diamond NV center probes compatible with conventional afm technology. *Applied Physics Letters*, 111(16):163106, 2017.

[48] Chathuranga Abeywardana, Viktor Stepanov, Franklin H Cho, and Susumu Takahashi. Magnetic resonance spectroscopy using a single nitrogen-vacancy center in diamond. In *Quantum and Nonlinear Optics III*, volume 9269, page 92690K. International Society for Optics and Photonics, 2014.

[49] Tobias Lühmann, Nicole Raatz, Roger John, Margarita Lesik, Jasper Rödiger, Marc Portail, Dominik Wildanger, Felix Kleißler, Kai Nordlund, Alexander Zaitsev, et al. Screening and engineering of colour centres in diamond. *Journal of Physics D: Applied Physics*, 51(48):483002, 2018.

[50] Alberto Boretti, Lorenzo Rosa, Jonathan Blackledge, and Stefania Castelletto. Nitrogen-vacancy centers in diamond for nanoscale magnetic resonance imaging applications. *Beilstein journal of nanotechnology*, 10(1):2128–2151, 2019.

[51] John F Barry, Matthew J Turner, Jennifer M Schloss, David R Glenn, Yuyu Song, Mikhail D Lukin, et al. Optical magnetic detection of single-neuron action potentials using quantum defects in diamond. *Proceedings of the National Academy of Sciences*, 113(49):14133–14138, 2016.

[52] Jan Jeske, Jared H Cole, and Andrew D Greentree. Laser threshold magnetometry. *New Journal of Physics*, 18(1):013015, 2016.

[53] Akihiro Kuwahata, Takahiro Kitaizumi, Kota Saichi, Takumi Sato, Ryuji Igarashi, Takeshi Ohshima, Yuta Masuyama, Takayuki Iwasaki, Mutsuko Hatano, Fedor Jelezko, et al. Magnetometer with nitrogen-vacancy center in a bulk diamond for detecting magnetic nanoparticles in biomedical applications. *Scientific reports*, 10(1):1–9, 2020.

[54] Xue Zhang, Georgios Chatzidrosos, Yinan Hu, Huijie Zheng, Arne Wickenbrock, Alexej Jerschow, and Dmitry Budker. Battery characterization via eddy-current imaging with nitrogen-vacancy centers in diamond. *Applied Sciences*, 11(7):3069, 2021.

[55] Ken Yahata, Yuichiro Matsuzaki, Shiro Saito, Hideyuki Watanabe, and Junko Ishi-Hayase. Demonstration of vector magnetic field sensing by simultaneous control of nitrogen-vacancy centers in diamond using multi-frequency microwave pulses. *Applied Physics Letters*, 114(2):022404, 2019.

[56] Binbin Zhao, Hao Guo, Rui Zhao, Fangfang Du, Zhonghao Li, Lei Wang, Dajin Wu, Yulei Chen, Jun Tang, and Jun Liu. High-sensitivity three-axis vector magnetometry using electron spin ensembles in single-crystal diamond. *IEEE Magnetics Letters*, 10:1–4, 2019.

[57] Felix A Hahl, Lukas Lindner, Xavier Vidal, Tingpeng Luo, Takeshi Ohshima, Shinobu Onoda, Shuya Ishii, Alexander M Zaitsev, Marco Capelli, Brant C Gibson, et al. Magnetic-field-dependent stimulated emission from nitrogen-vacancy centers in diamond. *Science Advances*, 8(22):eabn7192, 2021.

[58] Alexander Savvin, Alexander Dormidonov, Evgeniya Smetanina, Vladimir Mitrokhin, Evgeniy Lipatov, Dmitriy Genin, Sergey Potanin, Alexander Yelisseyev, and Viktor Vins. NV^-diamond laser. *Nature Communications*, 12(1):1–8, 2021.

[59] Andrew M Edmonds, Connor A Hart, Matthew J Turner, Pierre-Olivier Colard, Jennifer M Schloss, Kevin S Olsson, et al. Characterisation of CVD

diamond with high concentrations of nitrogen for magnetic-field sensing applications. *Materials for Quantum Technology*, 1(2):025001, 2021.

[60] Jennifer M Schloss, John F Barry, Matthew J Turner, and Ronald L Walsworth. Simultaneous broadband vector magnetometry using solid-state spins. *Physical Review Applied*, 10(3):034044, 2018.

[61] Tobias Lühmann, Roger John, Ralf Wunderlich, Jan Meijer, and Sébastien Pezzagna. Coulomb-driven single defect engineering for scalable qubits and spin sensors in diamond. *Nature Communications*, 10(1):1–9, 2019.

[62] Cort Johnson, Natalie L Adolphi, Kimberly L Butler, Debbie M Lovato, Richard Larson, Peter DD Schwindt, and Edward R Flynn. Magnetic relaxometry with an atomic magnetometer and squid sensors on targeted cancer cells. *Journal of Magnetism and Magnetic Materials*, 324(17):2613–2619, 2012.

[63] John Kitching. Chip-scale atomic devices. *Applied Physics Reviews*, 5(3):031302, 2018.

[64] Young Jin Kim and Igor Savukov. Ultra-sensitive magnetic microscopy with an optically pumped magnetometer. *Scientific reports*, 6(1):1–7, 2016.

[65] I Lovchinsky, JD Sanchez-Yamagishi, EK Urbach, S Choi, S Fang, TI Andersen, K Watanabe, T Taniguchi, A Bylinskii, E Kaxiras, et al. Magnetic resonance spectroscopy of an atomically thin material using a single-spin qubit. *Science*, 355(6324):503–507, 2017.

[66] Surjeet Rajendran, Nicholas Zobrist, Alexander O Sushkov, Ronald Walsworth, and Mikhail Lukin. A method for directional detection of dark matter using spectroscopy of crystal defects. *Physical Review D*, 96(3):035009, 2017.

[67] Hunter C Davis, Pradeep Ramesh, Aadyot Bhatnagar, Audrey Lee-Gosselin, John F Barry, David R Glenn, Ronald L Walsworth, and Mikhail G Shapiro. Mapping the microscale origins of magnetic resonance image contrast with subcellular diamond magnetometry. *Nature Communications*, 9(1):1–9, 2018.

[68] Franziska KK Kirschner, Felix Flicker, Amir Yacoby, Norman Y Yao, and Stephen J Blundell. Proposal for the detection of magnetic monopoles in spin ice via nanoscale magnetometry. *Physical Review B*, 97(14):140402, 2018.

[69] Dominik B Bucher, David R Glenn, Hongkun Park, Mikhail D Lukin, and Ronald L Walsworth. Hyperpolarization-enhanced NMR spectroscopy with

femtomole sensitivity using quantum defects in diamond. *Physical Review X*, 10(2):021053, 2020.

[70] NB Manson, JP Harrison, and MJ Sellars. Nitrogen-vacancy center in diamond: Model of the electronic structure and associated dynamics. *Physical Review B*, 74(10):104303, 2006.

[71] Lucio Robledo, Hannes Bernien, Toeno Van Der Sar, and Ronald Hanson. Spin dynamics in the optical cycle of single nitrogen-vacancy centres in diamond. *New Journal of Physics*, 13(2):025013, 2011.

[72] AT Collins, MF Thomaz, and MIB Jorge. Luminescence decay time of the 1.945 ev centre in type Ib diamond. *Journal of Physics C: Solid State Physics*, 16(11):2177, 1983.

[73] G Liaugaudas, G Davies, K Suhling, RUA Khan, and DJF Evans. Luminescence lifetimes of neutral nitrogen-vacancy centres in synthetic diamond containing nitrogen. *Journal of Physics: Condensed Matter*, 24(43):435503, 2012.

[74] Jürgen Köhler. Magnetic resonance of a single molecular spin. *Physics reports*, 310(5-6):261–339, 1999.

[75] Marco Capelli. *Investigation of artificial diamonds for optical sensing with ensemble of nitrogen-vacancy centres*. PhD thesis, RMIT University, 2019.

[76] Simon C Lawson, David Fisher, Damian C Hunt, and Mark E Newton. On the existence of positively charged single-substitutional nitrogen in diamond. *Journal of Physics: Condensed Matter*, 10(27):6171, 1998.

[77] R Jones, JP Goss, and PR Briddon. Acceptor level of nitrogen in diamond and the 270-nm absorption band. *Physical Review B*, 80(3):033205, 2009.

[78] Sally Eaton-Magaña, James E Shigley, and Christopher M Breeding. Observations on HPHT-grown synthetic diamonds: A review. *Gems & Gemology*, 53(3), 2017.

[79] M Capelli, AH Heffernan, T Ohshima, H Abe, J Jeske, A Hope, et al. Increased nitrogen-vacancy centre creation yield in diamond through electron beam irradiation at high temperature. *Carbon*, 143:714–719, 2019.

[80] Michael Schwander and Knut Partes. A review of diamond synthesis by CVD processes. *Diamond and Related Materials*, 20(9):1287–1301, 2011.

[81] CE Ashbaugh. Gemstone irradiation and radioactivity. *Gems & Gemology*, 24(4):196–213, 1988.

[82] Yoshimi Mita. Change of absorption spectra in type-Ib diamond with heavy neutron irradiation. *Physical Review B*, 53(17):11360, 1996.

[83] B Campbell and A Mainwood. Radiation damage of diamond by electron and gamma irradiation. *physica status solidi (a)*, 181(1):99–107, 2000.

[84] Alan T Collins and Isaac Kiflawi. The annealing of radiation damage in type Ia diamond. *Journal of Physics: Condensed Matter*, 21(36):364209, 2009.

[85] Gordon Davies. Charge states of the vacancy in diamond. *Nature*, 269(5628):498–500, 1977.

[86] JO Orwa, C Santori, KMC Fu, B Gibson, D Simpson, I Aharonovich, et al. Engineering of nitrogen-vacancy color centers in high purity diamond by ion implantation and annealing. *Journal of applied physics*, 109(8):083530, 2011.

[87] Claire A McLellan, Bryan A Myers, Stephan Kraemer, Kenichi Ohno, David D Awschalom, and Ania C Bleszynski Jayich. Patterned formation of highly coherent nitrogen-vacancy centers using a focused electron irradiation technique. *Nano Letters*, 16(4):2450–2454, 2016.

[88] DJ Twitchen, DC Hunt, C Wade, ME Newton, JM Baker, TR Anthony, and WF Banholzer. The production and annealing stages of the self-interstitial (R2) defect in diamond. *Physica B: Condensed Matter*, 273:644–646, 1999.

[89] Yiwen Chu, Nathalie Pulmones de Leon, Brendan J Shields, Birgit Hausmann, R Evans, Emre Togan, Michael John Burek, M Markham, Alastair Stacey, Alexander S Zibrov, et al. Coherent optical transitions in implanted nitrogen vacancy centers. *Nano Letters*, 14(4):1982–1986, 2014.

[90] Ariful Haque and Sharaf Sumaiya. An overview on the formation and processing of nitrogen-vacancy photonic centers in diamond by ion implantation. *Journal of Manufacturing and Materials Processing*, 1(1):6, 2017.

[91] Eric Van Oort and Max Glasbeek. Optically detected low field electron spin echo envelope modulations of fluorescent NV centers in diamond. *Chemical physics*, 143(1):131–140, 1990.

[92] Eric van Oort and Max Glasbeek. Fluorescence detected level-anticrossing and spin coherence of a localized triplet state in diamond. *Chemical physics*, 152(3):365–373, 1991.

[93] R Hanson, VV Dobrovitski, AE Feiguin, O Gywat, and DD Awschalom. Coherent dynamics of a single spin interacting with an adjustable spin bath. *Science*, 320(5874):352–355, 2008.

[94] Christian Osterkamp, Martin Mangold, Johannes Lang, Priyadharshini Balasubramanian, Tokuyuki Teraji, Boris Naydenov, et al. Engineering preferentially-aligned nitrogen-vacancy centre ensembles in CVD grown diamond. *Scientific reports*, 9(1):1–7, 2019.

[95] Jan Jeske, Desmond WM Lau, Xavier Vidal, Liam P McGuinness, Philipp Reineck, Brett C Johnson, et al. Stimulated emission from nitrogen-vacancy centres in diamond. *Nature Communications*, 8(1):1–8, 2017.

[96] SC Scholten, AJ Healey, IO Robertson, GJ Abrahams, DA Broadway, and J-P Tetienne. Widefield quantum microscopy with nitrogen-vacancy centers in diamond: Strengths, limitations, and prospects. *Journal of Applied Physics*, 130(15):150902, 2021.

[97] MS Grinolds, P Maletinsky, Sungkun Hong, MD Lukin, RL Walsworth, and A Yacoby. Quantum control of proximal spins using nanoscale magnetic resonance imaging. *Nature Physics*, 7(9):687–692, 2011.

[98] Patrick Appel, Elke Neu, Marc Ganzhorn, Arne Barfuss, Marietta Batzer, Micha Gratz, Andreas Tschöpe, and Patrick Maletinsky. Fabrication of all diamond scanning probes for nanoscale magnetometry. *Review of Scientific Instruments*, 87(6):063703, 2016.

[99] Alan T Collins. The Fermi level in diamond. *Journal of Physics: Condensed Matter*, 14(14):3743, 2002.

[100] K-MC Fu, C Santori, PE Barclay, and RG Beausoleil. Conversion of neutral nitrogen-vacancy centers to negatively charged nitrogen-vacancy centers through selective oxidation. *Applied Physics Letters*, 96(12):121907, 2010.

[101] MV Hauf, B Grotz, B Naydenov, M Dankerl, S Pezzagna, J Meijer, et al. Chemical control of the charge state of nitrogen-vacancy centers in diamond. *Physical Review B*, 83(8):081304, 2011.

[102] Erik Bauch, Swati Singh, Junghyun Lee, Connor A Hart, Jennifer M Schloss, Matthew J Turner, et al. Decoherence of ensembles of nitrogen-vacancy centers in diamond. *Physical Review B*, 102(13):134210, 2020.

[103] WV Smith, PP Sorokin, IL Gelles, and GJ Lasher. Electron-spin resonance of nitrogen donors in diamond. *Physical Review*, 115(6):1546, 1959.

[104] JA Van Wyk, EC Reynhardt, GL High, and I Kiflawi. The dependences of ESR line widths and spin-spin relaxation times of single nitrogen defects on the concentration of nitrogen defects in diamond. *Journal of Physics D: Applied Physics*, 30(12):1790, 1997.

[105] Gareth R Eaton, Sandra S Eaton, David P Barr, and Ralph T Weber. *Quantitative EPR*. Springer Science & Business Media, 2010.

[106] A Tallaire, AT Collins, D Charles, J Achard, R Sussmann, A Gicquel, ME Newton, AM Edmonds, and RJ Cruddace. Characterisation of high-quality thick single-crystal diamond grown by CVD with a low nitrogen addition. *Diamond and Related Materials*, 15(10):1700–1707, 2006.

[107] Inga A Dobrinets, Victor G Vins, and Alexander M Zaitsev. *HPHT-treated diamonds*. Springer, 2016.

[108] Stephanie Liggins. *Identification of point defects in treated single crystal diamond*. PhD thesis, University of Warwick, 2010.

[109] F De Weerdt and AT Collins. Determination of the C defect concentration in HPHT annealed type IaA diamonds from UV-VIS absorption spectra. *Diamond and Related Materials*, 17(2):171–173, 2008.

[110] HB Dyer, FA Raal, L Du Preez, and JHN Loubser. Optical absorption features associated with paramagnetic nitrogen in diamond. *Philosophical Magazine*, 11(112):763–774, 1965.

[111] RM Chrenko, HM Strong, and RE Tuft. Dispersed paramagnetic nitrogen content of large laboratory diamonds. *Philosophical Magazine*, 23(182):313–318, 1971.

[112] John Walker. Optical absorption and luminescence in diamond. *Reports on Progress in Physics*, 42(10):1605, 1979.

[113] Rizwan U A Khan, Philip Maurice Martineau, BL Cann, ME Newton, and DJ Twitchen. Charge transfer effects, thermo and photochromism in single crystal CVD synthetic diamond. *Journal of Physics: Condensed Matter*, 21(36):364214, 2009.

[114] RUA Khan, BL Cann, PM Martineau, J Samartseva, JJP Freeth, SJ Sibley, et al. Colour-causing defects and their related optoelectronic transitions in single crystal CVD diamond. *Journal of Physics: Condensed Matter*, 25(27):275801, 2013.

[115] H Sumiya and S Satoh. High-pressure synthesis of high-purity diamond crystal. *Diamond and Related Materials*, 5(11):1359–1365, 1996.

[116] T Luo, L Lindner, J Langer, V Cimalla, X Vidal, F Hahl, C Schreyvogel, S Onoda, S Ishii, T Ohshima, et al. Creation of nitrogen-vacancy centers in chemical vapor deposition diamond for sensing applications. *New Journal of Physics*, 24(3):033030, 2022.

[117] J-M Mäki, F Tuomisto, C Kelly, D Fisher, and P Martineau. Effects of thermal treatment on optically active vacancy defects in CVD diamonds. *Physica B: Condensed Matter*, 401:613–616, 2007.

[118] R Jones. Dislocations, vacancies and the brown colour of CVD and natural diamond. *Diamond and Related Materials*, 18(5-8):820–826, 2009.

[119] T. Luo, L. Lindner, R. Blinder, M. Capelli, J. Langer, V. Cimalla, F. A. Hahl, X. Vidal, and J. Jeske. Rapid determination of single substitutional nitrogen ns0 concentration in diamond from uv-vis spectroscopy. *Applied Physics Letters*, 121(6):064002, 2022.

[120] OR Rubinas, VV Soshenko, SV Bolshedvorskii, AI Zeleneev, AS Galkin, SA Tarelkin, et al. Optimization of the coherence properties of diamond samples with an intermediate concentration of NV centers. *Results in Physics*, 21:103845, 2021.

[121] Alexander I Shames, Alex I Smirnov, Sergey Milikisiyants, Evgeny O Danilov, Nicholas Nunn, Gary McGuire, et al. Fluence-dependent evolution of paramagnetic triplet centers in e-beam irradiated microcrystalline Ib type HPHT diamond. *The Journal of Physical Chemistry C*, 121(40):22335–22346, 2017.

[122] Marco Capelli, Lukas Lindner, Tingpeng Luo, Jan Jeske, Hiroshi Abe, Shinobu Onoda, Takeshi Ohshima, Brett Johnson, David A Simpson, Alastair Stacey, et al. Proximal nitrogen reduces the fluorescence quantum yield of nitrogen-vacancy centres in diamond. *New Journal of Physics*, 24(3):033053, 2022.

[123] FC Waldermann, Paolo Olivero, J Nunn, K Surmacz, ZY Wang, D Jaksch, et al. Creating diamond color centers for quantum optical applications. *Diamond and Related Materials*, 16(11):1887–1895, 2007.

[124] Jan M Binder, Alexander Stark, Nikolas Tomek, Jochen Scheuer, Florian Frank, Kay D Jahnke, Christoph Müller, Simon Schmitt, Mathias H Metsch, Thomas Unden, et al. Qudi: A modular python suite for experiment control and data processing. *SoftwareX*, 6:85–90, 2017.

[125] Robert Chapman and Taras Plakhotnik. Quantitative luminescence microscopy on nitrogen-vacancy centres in diamond: Saturation effects under pulsed excitation. *Chemical Physics Letters*, 507(1-3):190–194, 2011.

[126] C Zhang, H Yuan, N Zhang, LX Xu, B Li, GD Cheng, et al. Dependence of high density nitrogen-vacancy center ensemble coherence on electron irradiation doses and annealing time. *Journal of Physics D: Applied Physics*, 50(50):505104, 2017.

[127] Viktor Stepanov and Susumu Takahashi. Determination of nitrogen spin concentration in diamond using double electron-electron resonance. *Physical Review B*, 94(2):024421, 2016.

[128] Gordon Davies, Simon C Lawson, Alan T Collins, Alison Mainwood, and Sarah J Sharp. Vacancy-related centers in diamond. *Physical Review B*, 46(20):13157, 1992.

[129] Gordon Davies. Current problems in diamond: towards a quantitative understanding. *Physica B: Condensed Matter*, 273:15–23, 1999.

[130] Kasper Jensen, Nathan Leefer, Andrey Jarmola, Yannick Dumeige, Victor M Acosta, Pauli Kehayias, Brian Patton, and Dmitry Budker. Cavity-enhanced room-temperature magnetometry using absorption by nitrogen-vacancy centers in diamond. *Physical Review Letters*, 112(16):160802, 2014.

[131] Georgios Chatzidrosos, Arne Wickenbrock, Lykourgos Bougas, Nathan Leefer, Teng Wu, Kasper Jensen, Yannick Dumeige, and Dmitry Budker. Miniature cavity-enhanced diamond magnetometer. *Physical Review Applied*, 8(4):044019, 2017.

[132] R Hanson, O Gywat, and DD Awschalom. Room-temperature manipulation and decoherence of a single spin in diamond. *Physical Review B*, 74(16):161203, 2006.

[133] I Jakobi, S A Momenzadeh, F Fávaro de Oliveira, J Michl, F Ziem, M Schreck, P Neumann, A Denisenko, and J Wrachtrup. Efficient creation of dipolar coupled nitrogen-vacancy spin qubits in diamond. *Journal of Physics: Conference Series*, 752(1):012001, sep 2016.

[134] Peter Deák, Bálint Aradi, Moloud Kaviani, Thomas Frauenheim, and Adam Gali. Formation of NV centers in diamond: A theoretical study based on calculated transitions and migration of nitrogen and vacancy related defects. *Physical Review B*, 89(7):075203, 2014.

[135] Erwin L Hahn. Spin echoes. *Physical review*, 80(4):580, 1950.

[136] Vikas K Sewani, Hyma H Vallabhapurapu, Yang Yang, Hannes R Firgau, Chris Adambukulam, Brett C Johnson, Jarryd J Pla, and Arne Laucht. Coherent control of NV^- centers in diamond in a quantum teaching lab. *American Journal of Physics*, 88(12):1156–1169, 2020.

[137] Julia Langer. *Quantum-Grade Diamond for Cavity-based Solutions*. PhD thesis, Albert-Ludwigs-Universität Freiburg, 2022.

[138] Julia Langer, Volker Cimalla, Vadim Lebedev, Lutz Kirste, Mario Prescher, Tingpeng Luo, Jan Jeske, and Oliver Ambacher. Manipulation of the in situ nitrogen-vacancy doping efficiency in CVD-grown diamond. *physica status solidi (a)*, page 2100756, 2022.

[139] Sally Eaton-Magaña, Troy Ardon, and Alexander M Zaitsev. Inclusion and point defect characteristics of marange graphite-bearing diamonds after high temperature annealing. *Diamond and Related Materials*, 71:20–29, 2017.

[140] J Botsoa, T Sauvage, M-P Adam, P Desgardin, E Leoni, B Courtois, F Treussart, and M-F Barthe. Optimal conditions for NV^- center formation in type-1b diamond studied using photoluminescence and positron annihilation spectroscopies. *Physical Review B*, 84(12):125209, 2011.

[141] T Yamamoto, T Umeda, K Watanabe, S Onoda, ML Markham, DJ Twitchen, B Naydenov, LP McGuinness, T Teraji, S Koizumi, et al. Extending spin coherence times of diamond qubits by high-temperature annealing. *Physical Review B*, 88(7):075206, 2013.

[142] Srivatsa Chakravarthi, Chris Moore, April Opsvig, Christian Pederson, Emma Hunt, Andrew Ivanov, Ian Christen, Scott Dunham, and Kai-Mei C Fu. Window into NV center kinetics via repeated annealing and spatial tracking of thousands of individual NV centers. *Physical Review Materials*, 4(2):023402, 2020.

[143] Boris Naydenov, Friedemann Reinhard, Anke Lämmle, V Richter, Rafi Kalish, Ulrika FS D'Haenens-Johansson, Mark Newton, Fedor Jelezko, and Jörg

Wrachtrup. Increasing the coherence time of single electron spins in diamond by high temperature annealing. *Applied Physics Letters*, 97(24):242511, 2010.

[144] Jun-Feng Wang, Fei-Fei Yan, Qiang Li, Zheng-Hao Liu, He Liu, Guo-Ping Guo, Li-Ping Guo, Xiong Zhou, Jin-Ming Cui, Jian Wang, et al. Coherent control of nitrogen-vacancy center spins in silicon carbide at room temperature. *Physical Review Letters*, 124(22):223601, 2020.

[145] John Edwin Field and John Edwin Field. *Properties of natural and synthetic diamond*. Academic Press, 1992.

[146] AT Collins and M Stanley. Absorption and luminescence studies of synthetic diamond in which the nitrogen has been aggregated. *Journal of Physics D: Applied Physics*, 18(12):2537, 1985.

[147] HB Dyer and L du Preez. Irradiation damage in type I diamond. *The Journal of Chemical Physics*, 42(6):1898–1906, 1965.

[148] AM Zaitsev, KS Moe, and W Wang. Defect transformations in nitrogen-doped CVD diamond during irradiation and annealing. *Diamond and Related Materials*, 88:237–255, 2018.

[149] N Mizuochi, P Neumann, F Rempp, J Beck, V Jacques, P Siyushev, et al. Coherence of single spins coupled to a nuclear spin bath of varying density. *Physical Review B*, 80(4):041201, 2009.

[150] Felix Hahl. *Cavity-enhanced magnetic-field sensing via stimulated emission from nitrogen-vacancy centres in diamond*. PhD thesis, Albert-Ludwigs-Universität Freiburg, 2022.

[151] Alan T Collins, Alex Connor, Cheng-Han Ly, Abdulla Shareef, and Paul M Spear. High-temperature annealing of optical centers in type-I diamond. *Journal of applied physics*, 97(8):083517, 2005.

[152] James E Shigley, Emmanuel Fritsch, John I Koivula, Nikolai V Sobolev, Igor Y Malinovsky, and Yuri N Pal'yanov. The gemological properties of russian gem-quality synthetic yellow diamonds. *Gems & Gemology*, 29(4):228–248, 1993.

[153] AM Zaitsev, NM Kazuchits, VN Kazuchits, KS Moe, MS Rusetsky, OV Korolik, K Kitajima, JE Butler, and W Wang. Nitrogen-doped CVD diamond: Nitrogen concentration, color and internal stress. *Diamond and Related Materials*, 105:107794, 2020.

[154] Wuyi Wang, Patrick Doering, Joshua Tower, Ren Lu, Sally Eaton-Magaña, Paul Johnson, Erica Emerson, and Thomas M Moses. Strongly colored pink CVD lab-grown diamonds. *Gems & Gemology*, 46(1), 2010.

[155] VR Howes. The graphitization of diamond. *Proceedings of the Physical Society (1958-1967)*, 80(3):648, 1962.

[156] SJ Charles, JE Butler, BN Feygelson, ME Newton, DL Carroll, JW Steeds, H Darwish, C-S Yan, HK Mao, and RJ Hemley. Characterization of nitrogen doped chemical vapor deposited single crystal diamond before and after high pressure, high temperature annealing. *physica status solidi (a)*, 201(11):2473–2485, 2004.

[157] Yu-fei Meng, Chih-shiue Yan, Joseph Lai, Szczesny Krasnicki, Haiyun Shu, Thomas Yu, Qi Liang, Ho-kwang Mao, and Russell J Hemley. Enhanced optical properties of chemical vapor deposited single crystal diamond by low-pressure/high-temperature annealing. *Proceedings of the National Academy of Sciences*, 105(46):17620–17625, 2008.

[158] R Berman and Sir Francis Simon. On the graphite-diamond equilibrium. *Zeitschrift für Elektrochemie, Berichte der Bunsengesellschaft für physikalische Chemie*, 59(5):333–338, 1955.

[159] R Berman. The diamond-graphite equilibrium calculation: the influence of a recent determination of the gibbs energy difference. *Solid state communications*, 99(1):35–37, 1996.

[160] NM Kazuchits, MS Rusetsky, VN Kazuchits, OV Korolik, V Kumar, KS Moe, W Wang, and AM Zaitsev. Comparison of HPHT and LPHT annealing of Ib synthetic diamond. *Diamond and Related Materials*, 91:156–164, 2019.

[161] F De Weerdt and AT Collins. The influence of pressure on high-pressure, high-temperature annealing of type Ia diamond. *Diamond and Related Materials*, 12(3-7):507–510, 2003.

[162] D Fisher, DJF Evans, C Glover, CJ Kelly, MJ Sheehy, and GC Summerton. The vacancy as a probe of the strain in type IIa diamonds. *Diamond and Related Materials*, 15(10):1636–1642, 2006.

[163] H Pinto and R Jones. Theory of the birefringence due to dislocations in single crystal CVD diamond. *Journal of Physics: Condensed Matter*, 21(36):364220, 2009.

[164] Ian Friel, Sarah L Geoghegan, Daniel J Twitchen, and Geoffrey A Scarsbrook. Development of high quality single crystal diamond for novel laser applications. In *Optics and Photonics for Counterterrorism and Crime Fighting VI and Optical Materials in Defence Systems Technology VII*, volume 7838, pages 340–347. SPIE, 2010.

[165] I Friel, SL Clewes, HK Dhillon, N Perkins, DJ Twitchen, and GA Scarsbrook. Control of surface and bulk crystalline quality in single crystal diamond grown by chemical vapour deposition. *Diamond and Related Materials*, 18(5-8):808–815, 2009.

[166] Julia Langer, Volker Cimalla, Mario Prescher, Jana Ligl, Björn Tegetmeyer, Christoph Schreyvogel, and Oliver Ambacher. Quality assessment of in situ plasma-etched diamond surfaces for chemical vapor deposition overgrowth. *physica status solidi (a)*, 218(11):2100035, 2021.

[167] M Füner, C Wild, and P Koidl. Novel microwave plasma reactor for diamond synthesis. *Applied Physics Letters*, 72(10):1149–1151, 1998.